ADVANCED FUNCTIONAL MATERIALS
www.afm-journal.de

Mechanochemically Engineered Functional Materials: Advancing Photocatalysis for Sustainable Fuels

Oscar Trentin, Mario J. Muñoz-Batista, Alvise Perosa, Maurizio Selva, and Daily Rodriguez-Padron**

The pressing demand for sustainable energy solutions has spurred the development of innovative fuel production methods. Mechanochemistry has emerged as a powerful strategy for engineering functional materials with enhanced photocatalytic properties, offering a greener and more efficient route to solar-driven fuel generation. This review thoroughly explores the role of mechanochemistry in designing and optimizing visible-light-active photocatalysts, with a particular focus on hydrogen production and CO_2 photoreduction, highlighting its potential to enable energy-efficient, solvent-free, and scalable synthesis. The mechanochemical synthesis of advanced semiconductor-based photocatalysts, including titania-based materials, metal-free photocatalysts, supported metal species ranging from nanoparticles to clusters and single atoms, perovskites, Metal-Organic Frameworks (MOFs), and bioconjugates, offers a sustainable alternative to conventional fabrication methods, minimizing energy consumption and solvent waste. Additionally, the final section of this manuscript provides insights into the direct application of mechanical energy for fuel production. Finally, this review discusses the challenges and future directions of mechanochemically engineered photocatalysts, positioning this approach as a key enabler of next-generation solar fuel technologies.

1. Introduction

The global energy crisis and environmental degradation have accelerated the search for sustainable and renewable energy solutions. The increasing energy demand, coupled with the urgent need to mitigate climate change, necessitates transitioning from fossil fuels to alternative energy sources.[1,2]

In this context, hydrogen, the most abundant element in the universe, holds significant potential as a future energy carrier due to its nontoxic nature, high specific energy (120–142 MJ kg^{-1}), and zero greenhouse gas emissions when used in fuel cells or directly combusted, producing only water as a byproduct.[3–8]

Additionally, hydrogen's low density makes it safer in open environments, as it rapidly disperses upon accidental release, minimizing ignition risks.[9] However, hydrogen's light weight also contributes to its scarcity in molecular form (H_2) on Earth, thereby requiring efficient production and storage methods.[10,11]

Currently, ≈95% of hydrogen is produced from fossil fuels, primarily via steam methane reforming ($CH_4 + 2H_2O \rightarrow CO_2 + 4H_2$) at high temperatures (650–1000 °C). This is a cost-effective process, but it generates substantial CO_2 emissions estimated at ≈920 Mt $year^{-1}$ (2023) by the International Energy Agency (IEA).[12–18] Albeit CO_2 is a cheap, nontoxic, and abundant carbon feedstock to produce fuels and chemicals, its major contribution to global warming makes the control of its emissions crucial.[19–21]

To advance toward a more sustainable energy landscape, it is therefore imperative to simultaneously improve hydrogen production and develop efficient technologies for CO_2 capture and sequestration. Various approaches, including thermocatalysis,[22] electrocatalysis,[23] and photocatalysis, are being explored, with photocatalysis emerging as a particularly promising strategy due to its ability to harness a renewable and widely available source as solar energy, without any additional inputs.[24] Photocatalytic processes involve the absorption of light by a catalyst to generate electron–hole pairs, initiating subsequent chemical reactions.[25] However, the practical application of such processes is limited by rapid electron-hole recombination and inefficient charge transfer. To address these challenges, researchers have developed diverse catalytic materials such as metal oxides, graphitic carbon nitride, heterojunctions, and perovskites. Doping these materials with heteroatoms or metals can further enhance charge separation, prevent recombination, and optimize the band gap for hydrogen production and CO_2 reduction. These procedures are effective for the catalyst's synthesis, but they suffer from being time-consuming and requiring large amounts of solvents, often environmentally harmful ones.

O. Trentin, A. Perosa, M. Selva, D. Rodriguez-Padron
Dipartimento di Scienze Molecolari e Nanosistemi
Università Ca' Foscari Venezia
Via Torino 155, Venezia Mestre, Venice 30175, Italy
E-mail: selva@unive.it; daily.rodriguez@unive.it

M. J. Muñoz-Batista
Department of Chemical Engineering
University of Granada
Granada 18074, Spain

The ORCID identification number(s) for the author(s) of this article can be found under https://doi.org/10.1002/adfm.202506860

DOI: 10.1002/adfm.202506860

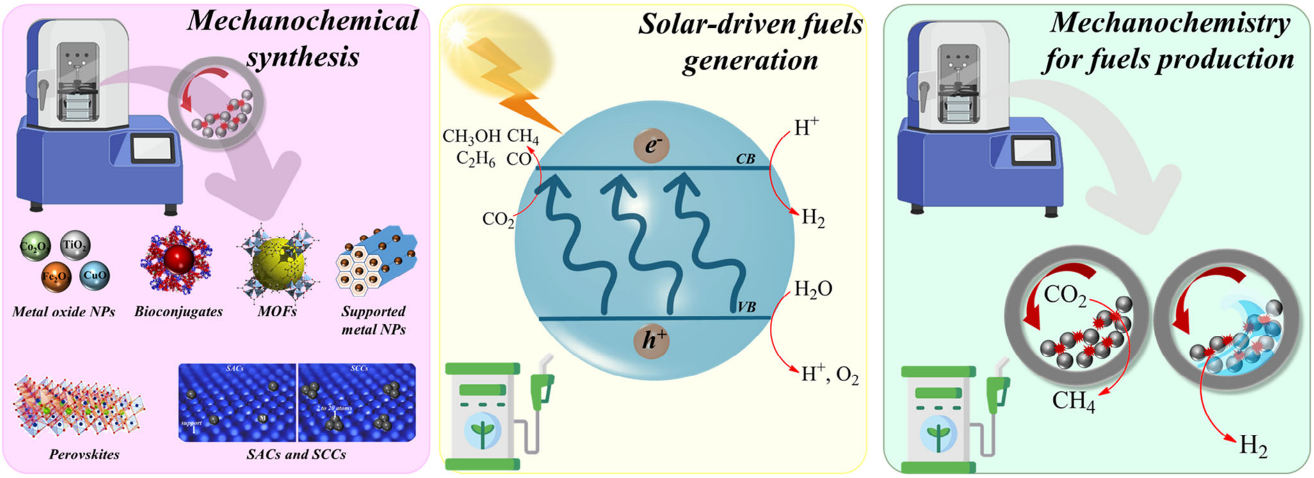

Figure 1. Outline of the topics covered in this review on the application of mechanochemistry in photocatalyst synthesis and sustainable fuel production.

In this context, mechanochemistry has emerged as a green alternative that aligns with the principles of sustainable chemistry. The International Union of Pure and Applied Chemistry (IUPAC) defines mechanochemistry as the field of chemical reactions induced by direct mechanical energy absorption.[26] Over the past few decades, mechanochemical reactions have gained attention for their ability to produce a wide range of materials with minimal or no solvent use, classified based on an empirical parameter, η (amount of liquid phase (in μL) per mg of solid reactants).[27–29] This approach includes neat grinding ($\eta = 0$ μL mg^{-1}) or liquid-assisted grinding (LAG) for η values between 0 and 1 μL mg^{-1}.[30,31] Indeed, mechanochemical synthesis not only enables solvent-free reactions but also allows the use of small liquid amounts, which could lead to different product selectivity. This technique could be particularly advantageous for synthesizing photocatalytic materials, particularly its scalability and eco-friendliness make it promising for producing materials that facilitate visible-light-driven hydrogen evolution and CO_2 reduction.

This review will focus on this specific subject by presenting a comprehensive analysis of the state of the art in mechanochemical synthesis of photocatalytic materials for hydrogen production and CO_2 reduction under visible light, with a particular emphasis on developments over the last 5 years (**Figure 1**). The discussion will address mechanochemical synthesis and photocatalytic performance of materials such as perovskites, MOFs, supported metal nanoparticles, bioconjugates, and metal-free materials like graphitic carbon nitride. Other mechanochemically synthesized materials with diverse visible-light-driven applications will be further explored as potential candidates for photocatalytic fuel production. Additionally, a section will be devoted to the direct generation of fuels through mechanochemical reactions.

2. Mechanochemical Synthesis: Principles and Approaches

Unlike traditional solution-based synthesis, mechanochemical processes do not rely on thermal activation or solvents, but instead use mechanical energy to promote bond formation and cleavage. The fundamental basis of mechanochemistry lies on the application of physical forces such as impact, compression, or shear, where the repeated application of localized mechanical stress generates reactive intermediates at the solid–solid interface. These conditions lead to the formation of structural defects (such as dislocations and vacancies), localized heating, and enhanced diffusion, all of which lower the activation energy required for reactions to proceed.[32,33] As a result, mechanochemical reactions often proceed under nonequilibrium conditions and can access unique reaction pathways that are inaccessible in solution.

Among mechanochemical methods, ball milling is the most established. It involves the use of mechanical mills (e.g., planetary, vibrational, or attritor mills) in which balls repeatedly collide with the solid reactants, enabling intimate mixing and high-energy impacts. Ball milling is versatile, scalable, and can be performed under solvent-free or solvent-minimized conditions. It is widely used for the synthesis of organic compounds, inorganic solids, and hybrid materials.

In addition to its versatility, ball milling also plays a crucial role in defect engineering at the atomic scale. The formation of structural defects, such as oxygen vacancies, during ball milling is strongly influenced by key parameters including milling time, frequency, ball-to-powder ratio, and energy input.[32] Several models have been proposed to quantitatively describe this relationship, often based on collision dynamics and energy transfer between the milling media and the powder.[34,35] These models typically correlate mechanical impact frequency or accumulated energy with defect concentration, showing that defect formation increases with milling energy, up to an optimal point, beyond which excessive energy may lead to particle agglomeration or structural collapse.[36] Such correlations provide a valuable framework for tuning defect densities and optimizing photocatalytic properties through controlled mechanochemical processing.[37,38]

A more recent and gentler alternative is resonant acoustic mixing (RAM), which uses low-frequency acoustic energy to agitate and homogenize solid mixtures without grinding media. This technique is advantageous for materials that are sensitive to mechanical stress or require precise control of morphology, such as pharmaceutical co-crystals and soft hybrid materials. RAM provides uniform energy distribution and is free from contamination by milling media.

Twin-screw extrusion (TSE) offers another mechanochemical approach, enabling continuous processing under controlled shear and compressive forces. In this method, solid reactants are conveyed and mixed by intermeshing rotating screws, often at elevated temperatures. TSE is highly attractive for its industrial scalability, short residence times, and precise control over reaction parameters. It has been successfully applied to the synthesis of polymers, inorganic nanomaterials, and is increasingly used for solvent-free synthesis of catalytic materials.

Mechanochemistry offers a powerful and sustainable alternative to traditional solution-based synthesis. Its solvent-free or solvent-minimized nature significantly reduces waste generation and environmental impact, while enabling reactions under ambient or mild conditions with high energy efficiency. Mechanochemical methods often lead to shorter reaction times, enhanced selectivity, and access to unique materials or reactivity profiles that are difficult to achieve via conventional routes. These advantages make mechanochemistry particularly attractive for the development of greener processes and innovative materials across diverse chemical domains.

3. Mechanochemically Engineered Materials for Sustainable Fuel Production via Photocatalysis

3.1. Visible-Light-Driven H_2 Photoproduction

3.1.1. Mechanochemically-Modified Titania-Based Materials

Titanium dioxide (TiO_2) has long been recognized as a benchmark photocatalyst for hydrogen (H_2) production due to its stability, non-toxicity, and strong redox capabilities. However, its wide bandgap (≈3.2 eV for anatase) limits its absorption primarily to the UV region, restricting its efficiency under visible light. To overcome this limitation, the incorporation of metal nanoparticles (MNPs) onto TiO_2 or the modification of its crystal structure have emerged as strategies to extend light absorption and enhance charge carrier dynamics. Noble metals such as Pt, Au, and Pd act as electron sinks, suppressing charge recombination and promoting hydrogen evolution, while nonprecious metals and alloy-based systems offer cost-effective alternatives with promising activity. Recent advancements in material engineering, including plasmonic enhancement, alloying effects, and tailored metal-support interactions, have further improved photocatalytic efficiency. This section explores the latest advances in mechanochemically-modified TiO_2 systems for visible-light-driven H_2 production, with emphasis on sustainability.

Particularly, gold-modified titania has been designed as a photocatalyst for visible-light-driven hydrogen evolution, leveraging the localized surface plasmon resonance (LSPR) effect of gold nanoparticles to extend light absorption beyond the UV region. Several examples in the literature highlight the use of mechanochemical methods for synthesizing these materials, ranging from Au nanoparticles to clusters. For instance, Caps et al. described a solvent-free mechanochemical approach to synthesize Au/TiO_2 nanocomposites through solid-state grinding, followed by mild heat treatment to convert gold precursors into metallic gold nanoparticles. The authors emphasized that the thermal treatment atmosphere plays a crucial role in determining the photocatalytic performance. Air is proving more effective than hydrogen in promoting the decomposition of the gold complex and enhancing the Au/TiO_2 interface. Among the tested compositions, the catalyst containing 0.5 wt.% Au exhibited the highest hydrogen evolution rate of ≈500 μmol H_2 h^{-1} g^{-1} under simulated solar irradiation with methanol as a sacrificial agent.[39] In another investigation by the same group, Au/TiO_2 nanocomposites synthesized via solid grinding demonstrated higher photocatalytic activity than those obtained through chemical reduction. The superior performance of the mechanochemically prepared catalysts was attributed to the intimate contact between gold and titania nanoparticles, particularly when subjected to calcination at 400 °C. This treatment improved the metal-support interaction and promoted efficient charge separation and electron transfer, both of which are essential for enhancing photocatalytic hydrogen production.[40]

Moreover, in a study by Llorca et al., high-surface-area TiO_2 lyogels were prepared and thermally transformed into defined anatase–rutile mixtures, subsequently being decorated with Au nanoparticles (≈2 nm) preformed via ball milling. Lyogels, a class of gel materials formed by the removal of solvent from a colloidal network, serve as versatile precursors for high-surface-area metal oxides. Authors found that the optimal photocatalyst among those prepared was obtained by calcining the lyogel at 550 °C and exhibited a hydrogen photoproduction rate of 19.8 mmol H_2 g^{-1} h^{-1} under an irradiance of 80 mW cm^{-2} and a gas hourly space velocity (GHSV) of 26 000 h^{-1}. Structural characterization confirmed that this sample contained 84% anatase and 16% rutile, a composition closely resembling commercial P25 TiO_2, widely recognized for its photocatalytic efficiency. As an alternative synthetic strategy, Au nanoparticles were incorporated into the TiO_2 gel before lyophilization, followed by calcination. This method led to the formation of larger Au nanoparticles (up to 18 nm), which exhibited a strong interaction with the TiO_2 matrix and significantly delayed the anatase-to-rutile transformation. The study underscored the critical role of TiO_2 polymorph control in optimizing photocatalytic hydrogen evolution.[41]

Reducing metal particle size from nanometers to atomically dispersed clusters is a well-established approach to enhancing photocatalytic efficiency. However, achieving this with a simple, rapid, and scalable synthesis method remains a challenge. In this context, Jordi Llorca and colleagues reported a mechanochemical strategy using ball milling, which successfully facilitated the direct synthesis and dispersion of gold clusters onto a TiO_2 surface in a single step, eliminating the need for solvents or complex processing (**Figure** 2A). The strong interaction between gold and TiO_2 in the ball-milled material significantly enhanced charge separation and photocatalytic activity, leading to a hydrogen evolution rate twice as high as that of conventional Au/TiO_2 catalysts containing larger nanoparticles. By optimizing milling conditions, including ball-to-powder ratio, milling time, and frequency, highly dispersed gold clusters were achieved, resulting in lower charge transfer resistance and improved photocurrent response. This mechanochemical method provides a fast, cost-effective, and environmentally friendly platform for fabricating ultrasmall metal clusters for sustainable energy applications.[42]

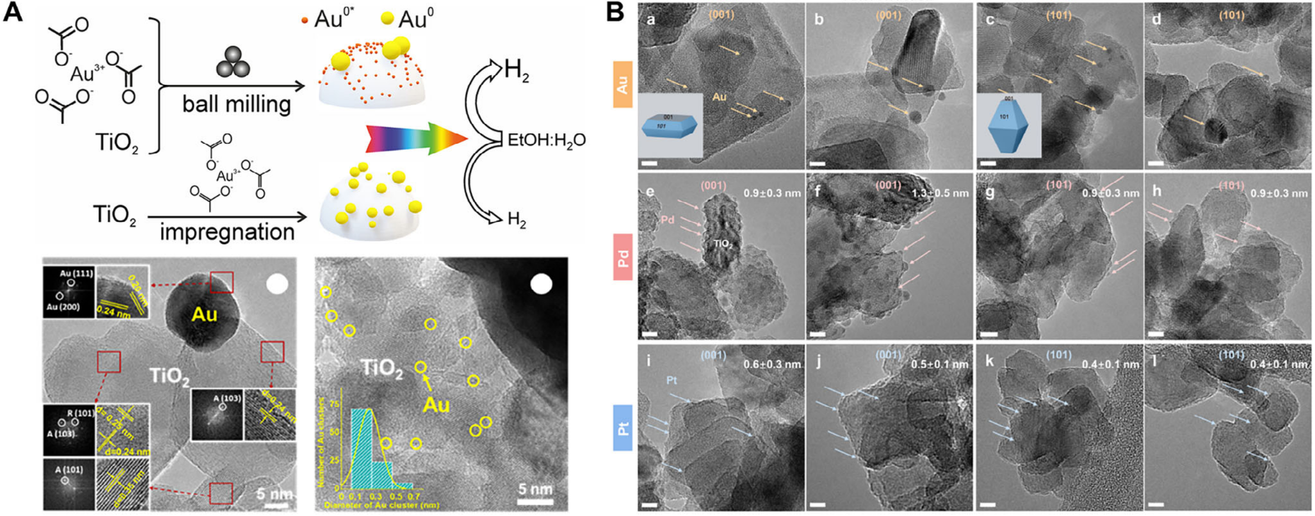

Figure 2. A) Schematic illustration of the mechanochemical synthesis of Au clusters supported on TiO_2, along with corresponding HRTEM images. Reproduced with permission from ref. [42] B) HRTEM images of samples before and after the photoreaction: (a,b) Au/TiO_2-001, (c,d) Au/TiO_2-101, (e, f) Pd/TiO_2-001, (g,h) Pd/TiO_2-101, (i,j) Pt/TiO_2-001, and (k,l) Pt/TiO_2-101. Scale bar: 5 nm. Reproduced with permission from ref. [44].

In addition to gold-functionalized materials, palladium nanoparticles and clusters have also been synthesized via mechanochemical methods for visible-light-driven hydrogen production. A one-step ball milling approach was reported for the formation of highly dispersed Pd clusters on TiO_2, establishing a unique metal-support interface. This interface allowed the dynamic evolution of Pd clusters into nanoparticles during photocatalytic hydrogen production while maintaining stable performance over 100 h. Photoluminescence (PL) analysis revealed that Pd loading on TiO_2 significantly suppressed fluorescence intensity, particularly in the Pd/TiO_2-BM sample, indicating reduced electron–hole recombination and prolonged charge carrier lifetime. Transient photocurrent response measurements further corroborated these results, demonstrating enhanced carrier mobility in Pd-modified TiO_2, with Pd/TiO_2-BM outperforming other samples. Notably, this interaction was exclusive to ball-milled materials and disappeared upon calcination, mirroring observations in Au/TiO_2 systems, where ball milling enhanced charge separation and catalytic efficiency. For Pd/TiO_2, variations in milling parameters such as vibration frequency (15–50 Hz), ball-to-powder ratio (13–90), and milling time (1–120 min) were systematically explored, revealing that fine-tuning these parameters significantly influenced cluster dispersion and catalytic performance.[43] The authors further expanded the application of mechanochemistry to design metal clusters (Pt, Pd, and Au) supported on anatase TiO_2 nanoparticles, strategically engineered to preferentially expose specific crystal facets ({001} plates and {101} bipyramids (Figure 2B). The stability of metal clusters depended on both the metal species nanosheet and the TiO_2 facet, with Pt/TiO_2 showing superior stability over Pd/TiO_2 and Au/TiO_2, particularly on {001} facets. In this case, mechanochemical synthesis ensured uniform cluster distribution, preventing sintering during photocatalysis and maintaining high hydrogen evolution performance.[44]

The incorporation of non-noble metals onto titania surfaces via mechanochemistry has been a key focus in recent research efforts to reduce reliance on costly and scarce noble metals.[45–52] In this context, the exploration of copper-, nickel-, or molybdenum-based systems deserves particular attention. In a recent study, ball-milling-synthesized Pt–Cu–TiO_2 composites, featuring different TiO_2 nanoshapes (nanotubes, nanobelts, and nanowires) and further modified with orange peel-derived reduced graphene oxide (rGO), were investigated for hydrogen evolution from water–alcohol mixtures (Figure 2A). Notably, the partial substitution of platinum with copper significantly reduced the cost associated with noble-metal-based photocatalysts while maintaining high hydrogen production efficiency (**Figure** 3A). Furthermore, the integration of rGO played a crucial role in enhancing photocatalytic performance. The conductive nature of rGO facilitated charge separation and electron transport, ultimately boosting hydrogen evolution to ≈27 mmol H_2 g^{-} h^{-1}.[53]

Furthermore, in a recent study using mechanochemical methods, Cu nanodots with sizes under 5 nm (Cu loading below 10 wt.%) were uniformly dispersed on TiO_2.[54] The size of the Cu nanoparticles was carefully controlled by varying the milling environment, with nanoparticles obtained under different conditions—Cu-ethanol, Cu-water, and Cu-drying milling—showing distinct size distributions. Dry milling produced the smallest Cu clusters, all under 2 nm (1 ± 0.7 nm). Milling with ethanol resulted in larger clusters (2.5 ± 0.8 nm), while milling in water formed Cu_2O clusters ≈2 ± 0.8 nm. The optimal photocatalytic performance for hydrogen generation was achieved with Cu/TiO_2 composites containing 2.0 wt.% Cu, where the Cu nanoparticles ranged from 2 to 4 nm in size. The enhanced and stable hydrogen evolution observed in these composites was further supported by transient photocurrent responses for three 60 s light-on-off cycles in 1 M Na_2SO_4 aqueous solution under solar light irradiation with a bias potential of 1.0 V, indicating efficient photogenerated charge separation. Interestingly, the study found that excessively small Cu clusters hindered the hydrogen evolution activity, despite having the same Cu loading. On the other hand, larger Cu nanoparticles (2–4 nm) improved photocatalytic

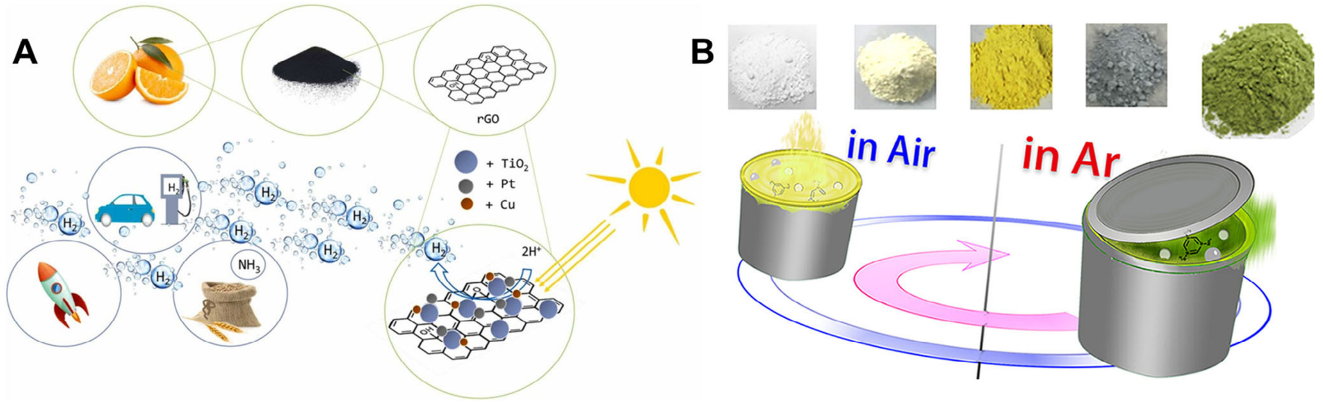

Figure 3. A) Schematic illustration of the mechanochemical synthesis of a TiO_2-rGO composite doped with Pt and Cu for hydrogen photoproduction. Reproduced with permission from ref. [53]. B) Schematic representation of TiO_2 photocatalysts—green, gray, orange, and yellow—synthesized via a mechanochemical approach.[57].

performance by reducing electron–hole recombination, thus enhancing activity. These findings highlighted the importance of both Cu nanoparticle size and loading in optimizing the photocatalytic activity of Cu/TiO_2 composites.[54]

Photocatalytic water splitting is a promising renewable method for H_2 production, but its efficiency is limited by slow water oxidation kinetics, electron–hole recombination, and the undesired back reaction forming H_2O. To overcome these challenges, sacrificial agents such as biomass-derived compounds and alcohols are used to enhance electron transfer, suppress recombination, and promote selective H_2 generation.[55] Examples include glucose, ethanol, and glycerol, which not only improve H_2 production but also offer sustainable waste valorization opportunities. Building on this approach, a study by Palmisano et al. reported the use of mechanochemically synthesized copper–titania composites as efficient photocatalysts for solar-to-hydrogen (STH) conversion under real conditions. Systematic optimization of milling parameters, such as time and rotation speed, further improved photocatalytic performance. Among various biomass-derived sacrificial agents, glycerol yielded the highest STH efficiency (1.71%) when paired with the 3%Cu_2O-P25 photocatalyst (milling conditions 150 rpm, 2 h). Notably, and as expected, ball-milled composites significantly outperformed those prepared by simple hand mixing.[56]

Mechanochemical synthesis via ball milling continues to prove its effectiveness in engineering other metal oxide clusters on TiO_2, as evidenced by the successful fabrication of NiO/TiO_2 p–n heterojunction photocatalysts. Similar to Au/TiO_2 and Pd/TiO_2 systems,[42,43] the ball milling process enables the formation of highly dispersed NiO clusters, which significantly enhance charge separation and boost photocatalytic H_2 evolution under sunlight. Notably, the NiO/P90-BM sample achieved an H_2 evolution rate (8.85 mmol h^{-1} g^{-1}) over 12 times higher than that of pristine TiO_2 (0.73 mmol h^{-1} g^{-1}), underscoring the crucial role of mechanochemically induced interactions between NiO and the semiconductor support. The predominance of high-spin Ni^{2+} configurations further contributes to the improved charge transfer properties, as corroborated by photoelectrochemical measurements.[58]

In addition, molybdenum sulfides, particularly MoS_2, have been explored as effective co-catalysts for modifying titanium-based photocatalysts, enhancing their performance for solar-driven hydrogen production. Mechanochemical synthesis offers a simple and efficient route for fabricating MoS_2-TiO_2 composites by eliminating the need for complex precursor-based reduction protocols. This was demonstrated by the work of Yanyan Zhu and coworkers, who reported an approach that significantly streamlined the synthesis of the composites while enhancing their photocatalytic performance. The optimized 4.0% MoS_2-TiO_2 material, processed at 300 rpm for 2 h, achieved an H_2 evolution rate of 150.7 µmol h^{-1}, 48.6 times higher than pristine TiO_2.[59] The photocatalytic stability of MoS_2-TiO_2 composites was confirmed through repeated hydrogen evolution experiments conducted over three cycles of 6 h each, totaling 18 h. The consistent hydrogen production across all cycles indicated excellent stability of the photocatalyst during long-term operation. Furthermore, transient photocurrent response measurements showed that all MoS_2-TiO_2 composites exhibited higher photocurrent densities compared to pristine TiO_2, suggesting enhanced separation and migration efficiency of photogenerated charge carriers, attributed to the electron-accepting role of MoS_2. Notably, the sample with 4.0% MoS_2 loading achieved the highest photocurrent (≈0.09 mA), nearly 20 times greater than that of pure TiO_2. This improvement was attributed to the strong interfacial interaction between MoS_2 and TiO_2 induced by the ball milling process, which facilitated efficient charge transfer across the heterojunction.

Moreover, the modification of the crystal structure of TiO_2 through defects, doping, and phase mixing can extend its light absorption to the visible and even near-infrared (NIR) regions. However, while enhancing absorption can improve photocatalytic performance, excessive structural disorder may lead to deactivation. In a recent study by Saitow and Wang, four differently colored TiO_2 photocatalysts—green, gray, orange, and yellow—were synthesized using a mechanochemical approach (Figure 3B). The milling process, performed with or without melamine under ambient conditions for 2 h, significantly altered the electronic structure of TiO_2 by introducing controlled defect densities and dopant levels. Dry milling in air or argon was found to influence the formation of oxygen vacancies and Ti^{3+} centers, as well as the distribution of polymorphic phases, including anatase, rutile, high-pressure TiO_2-II (α-PbO_2 or columbite), and amorphous phases. Characterization by spectroscopy, microscopy, and diffraction methods revealed that green and orange TiO_2, which contained all four phases along with a high concentration of defects and heterojunctions, exhibited a fivefold increase in photocatalytic activity compared to commercial titania P25. Spectroscopy analysis indicated that red light from the NIR region played a key role in driving the photocatalytic reaction, while the reduced band gap ($E_g = 2.3$ eV) was critical for visible-light activity. Additionally, specific thresholds for absorbance and defect density were identified as necessary for enhanced photocatalytic performance. These TiO_2 photocatalysts achieved high activity without requiring metal co-catalysts or additional promoters, highlighting the effectiveness of mechanochemical synthesis in developing efficient and sustainable photocatalysts.[57]

3.1.2. Mechanochemically-Prepared Titanate-Based Materials

While TiO_2 is a commonly employed semiconductor photocatalyst, titanates such as sodium titanate ($NaTiO_3$), potassium titanate ($K_2Ti_6O_{13}$), and barium titanate ($BaTiO_3$) possess distinct properties that set them apart from TiO_2 in terms of structure, electronic behavior, and photocatalytic performance. Titanates often demonstrate superior photocatalytic activity, exhibit varied band gap energies, and can form different nanostructures, which offer enhanced efficiency and versatility compared to TiO_2 in certain applications.

Electronic waste, particularly discarded ceramic capacitors rich in $BaTiO_3$, Ag, Sn, and Ni, represents a valuable but underutilized resource for sustainable recycling. Conventional recovery methods, such as pyrometallurgy and hydrometallurgy, require significant energy input, involve multiple processing steps, and generate liquid waste. In contrast, a recent study by Gao et al. introduced an innovative mechanochemical approach that bypassed the need for chemical reagents, enabling the direct transformation of waste ceramic capacitors into self-doped $BaTiO_3$ photocatalysts via ball milling. The effects of milling time and ball-to-waste ratio on the structural, optical, and electronic properties of the resulting materials were systematically analyzed to optimize their photocatalytic hydrogen production. Photoluminescence (PL) analysis revealed that changes in ball milling parameters significantly influence the charge separation behavior of $BaTiO_3$-based photocatalysts. A pronounced emission peak at ≈410 nm, associated with radiative recombination of self-trapped excitons, was observed to decrease with higher ball-to-waste ratios, indicating improved charge separation. In contrast, extended milling time increased PL intensity, suggesting reduced separation efficiency. Complementary transient photocurrent response measurements showed that the sample milled for 1 h with a 20:1 ball-to-waste ratio exhibited the highest photocurrent density, confirming optimal electron–hole separation under these conditions, and achieved an impressive H_2 evolution rate of 191.3 $\mu mol\ g^{-1}\ h^{-1}$. The findings highlight the mechanochemical impact on both the synthesis and performance enhancement of $BaTiO_3$-based photocatalysts while providing a scalable and environmentally friendly strategy for upcycling e-waste into functional materials.[60]

In another example, Ilmenite ($FeTiO_3$) concentrates, derived from ilmenite-rich black sand through gravimetric and magnetic separation, were modified via high-energy ball milling to develop a cost-effective photocatalyst with enhanced hydrogen production capabilities. Milling was performed for varying durations (1–3 h) in the presence or absence of MgO or metallic Mg (0.5–3.0 wt.%) to incorporate magnesium into the $FeTiO_3$ structure while simultaneously reducing particle size. The goal of Mg insertion was to shift the conduction band potential to more negative values, despite a slight increase in band gap energy. Structural characterization revealed that milling induced partial amorphization of ilmenite, with no significant changes in lattice parameters, while substitutional doping was indicated by increased hematite peaks in XRD patterns. The photocatalytic activity for H_2 evolution (under UV light) improved significantly from 240.5 $\mu mol\ g^{-1}\ h^{-1}$ (unmilled) to 296.0 $\mu mol\ g^{-1}\ h^{-1}$ (2-h milling with 1.0 wt.% MgO), primarily due to electronic structure modifications rather than increased surface area.[61]

3.1.3. Mechanochemically-Prepared Supported Metal Nanoparticles on Carbonaceous Materials

Carbonaceous materials, such as graphdiyne (GDY), graphitic carbon nitride (g-C_3N_4), and black phosphorus (BP), have emerged as promising supports for metal nanoparticles due to their unique electronic properties, high surface area, and ability to facilitate charge transfer. Mechanochemical synthesis has been widely adopted to fabricate these materials and their composites, offering significant advantages over traditional solution-based methods.

Graphdiyne (GDY), a 2D carbon allotrope with *sp* and sp^2 hybridized structures, has been widely explored for photocatalytic applications. Its adjustable electronic structure, excellent conductivity, and electron delocalization properties make it an ideal candidate for constructing heterojunction photocatalysts. The synthesis of GDY and its composites often involves mechanochemical methods. For example, GDY can be prepared by ball milling calcium carbide (CaC_2) and hexabromobenzene (C_6Br_6) in the presence of catalysts such as tetraphenyl(triphenylphosphine)palladium and copper acetate. The resulting GDY precursor is then subjected to refluxing and calcination to obtain the final product.[62] This approach has been extended to fabricate GDY-based heterojunctions, such as Cu_3P@GDY, where the *p*–*n* junction between *p*-type Cu_3P and *n*-type GDY creates a built-in electric field that promotes charge separation and enhances photocatalytic H_2 evolution.[62] Electrochemical and photophysical characterizations confirmed the improved charge separation and transfer in the Cu_3P@GDY composite. Transient photocurrent measurements revealed that this material exhibits a significantly higher photocurrent response compared to GDY and Cu_3P, indicating more efficient suppression of electron–hole recombination. Photoluminescence (PL) analysis demonstrated quenched emission intensity upon Cu_3P@GDY addition, suggesting enhanced electron extraction and reduced recombination. Time-resolved photoluminescence (TRPL) decay analysis revealed that this composite exhibits a

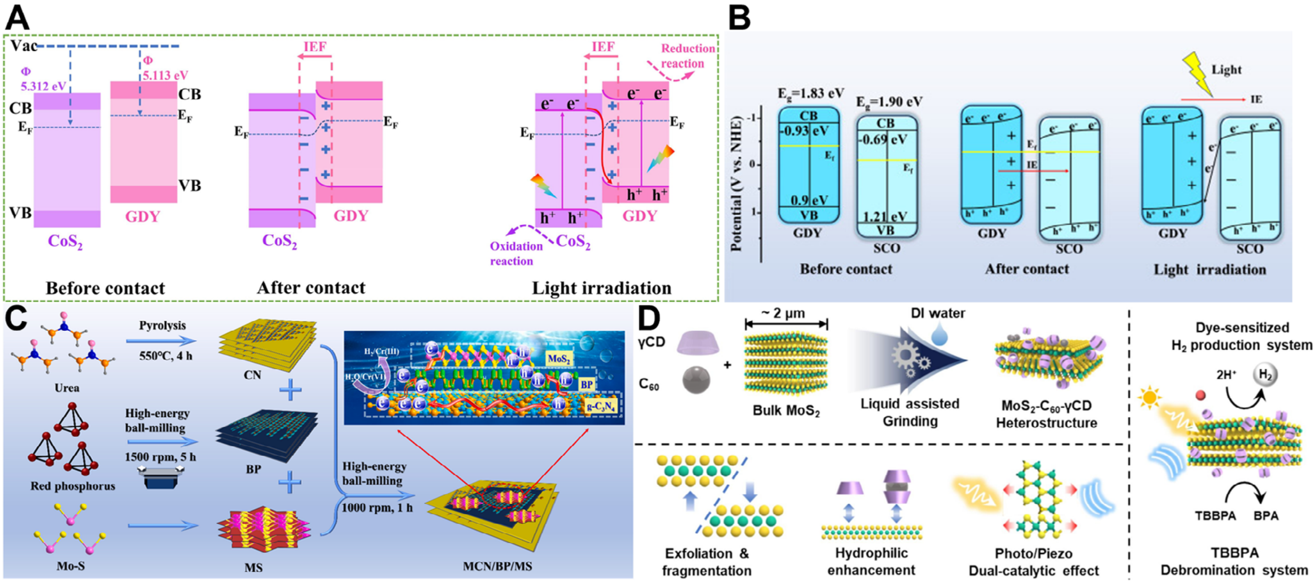

Figure 4. A) Representation of the relative energy band alignment and S-scheme charge transfer mechanism between CoS_2 and GDY. Reproduced with permission from ref. [63]. B) Electron transfer dynamics between SCO and GDY prior to and following contact. Reproduced with permission from ref. [64]. C) Schematic illustration of the synthesis pathway for MoS_2-modified g-C_3N_4/black phosphorus photocatalyst. Reproduced with permission from ref. [67]. D) Illustrative representation of the mechanochemical synthesis of supramolecular MoS_2 nanosheets with C_{60}-γCD complexes for H_2 photoproduction. Reproduced with permission from ref. [70].

much faster decay than Cu_3P and a similar average lifetime to GDY (≈0.25 ns), confirming the formation of an efficient p–n heterojunction that facilitates rapid charge transfer and limits recombination.

Moreover, the integration of GDY with cobalt disulfide through mechanochemical ball milling has been reported by Jin et al., demonstrating the formation of a S-scheme heterojunction, which significantly enhances photocatalytic H_2 evolution (**Figure** 4A).[63] The curly, thin-layer structure of GDY prevents the agglomeration of CoS_2 nanoparticles, ensuring a well-dispersed and tightly bonded interface. Electrochemical and optical characterizations confirmed the enhanced charge separation and photocatalytic activity of the CoS_2/GDY heterojunction (CSGY-20). The composite exhibited a stronger photocurrent response than the individual components, indicating more efficient charge carrier separation, while PL spectra showed pronounced fluorescence quenching, suggesting reduced recombination of photogenerated electron–hole pairs. Moreover, TRPL measurements demonstrated a significantly shortened fluorescence lifetime in the composite, consistent with a faster non-radiative electron transfer pathway between CoS_2 and GDY, which promotes charge carrier mobility and accelerates the photocatalytic process. In situ X-ray photoelectron spectroscopy and density functional theory calculations have confirmed the S-scheme charge transfer mechanism. In this case, while the synthesis of GDY goes via mechanochemistry, the subsequent steps still rely on solution-based methods. This aspect may require further optimization to minimize energy and solvent consumption, as well as processing time.[63]

Similarly, the combination of GDY with strontium cobalt oxide ($Sr_2Co_2O_5$) has been reported to form an S-scheme heterojunction with exceptional stability and proton adsorption properties. The hierarchical flower-like structure of $Sr_2Co_2O_5$, coupled with the layered GDY, enhances the specific surface area and facilitates water adsorption. The charge separation capabilities of the synthesized materials were evaluated using both steady-state PL and TRFS. Among the samples, this composite exhibited the lowest photoluminescence intensity, indicating the most efficient suppression of electron–hole recombination. This enhanced separation efficiency was attributed to the presence of GDY, whose rich chemical bonding environment facilitates photogenerated electron capture. Time-resolved photoluminescence analysis revealed that GSCO20 possessed an intermediate carrier lifetime (217.68 ps) relative to those of GDY (14.28 ps) and $Sr_2Co_2O_5$ (385.92 ps), confirming both effective charge separation and improved transfer kinetics within the composite. In this study, Zhengyu Zhou and colleagues carried out density functional theory (DFT) calculations, revealing that both GDY and $Sr_2Co_2O_5$ possess direct bandgaps, enabling efficient electronic transitions without phonon assistance, thereby improving solar energy conversion efficiency (Figure 4B). Although GDY synthesis was performed by mechanochemical methods via ball milling, the synthesis of both $Sr_2Co_2O_5$ and graphdiyne/$Sr_2Co_2O_5$ still involves hydrothermal methods. Therefore, a potential improvement could involve replacing or integrating the reported protocols with mechanochemical approaches to further streamline the process.[64]

Furthermore, transition metal phosphides (TMPs), such as nickel phosphide (Ni_2P) and molybdenum phosphide (MoP), have also been explored as cocatalysts for photocatalytic H_2 production. These materials exhibit high work functions and low hydrogen evolution overpotentials, making them effective electron traps and reactive centers. For instance, Ni_2P-modified g-C_3N_4 prepared via ball milling has shown a nine-fold increase in H_2 evolution activity compared to pristine g-C_3N_4. The combination of phosphorus-doped (graphitic carbonitride) g-C_3N_4 (PCN) with

MoP further enhances photocatalytic performance by introducing mid-gap states that broaden light absorption and improve electrical conductivity. In particular, the formation of Mo-N bonds at the interface facilitates electron transfer, while the Schottky barrier promotes charge separation, resulting in a H_2 evolution rate up to 4917.83 µmol g^{-1} h^{-1}.[65,66]

In addition, g-C_3N_4, as a well-known semiconductor, has been utilized in the design other composite materials prepared via mechanochemistry, such as those incorporating MoS_2 or nickel nanoparticles.[67,68] Additionally, its combination with black phosphorus (BP) has also been explored, as BP exhibits exceptional electronic properties, including a tunable band gap and high charge carrier mobility.[69] A high-efficiency MoS_2-modified g-C_3N_4/black phosphorus photocatalyst was developed using high-energy ball milling (Figure 4C).[67] The optimized composite exhibited a H_2 evolution rate of 2146.8 µmol g^{-1} h^{-1} and excellent Cr(VI) reduction activity. The type-I/Z hybrid charge transfer mechanism promoted multistep charge migration, enhancing charge separation and preserving the reducing capacity of photogenerated electrons. In another example, Min Wen et al. synthesized a CN/BP@Ni heterostructure by anchoring nickel nanoparticle-decorated BP nanosheets to g-C_3N_4. The tight interfacial interaction and cascaded electron-transfer channel from CN to BP and then to Ni nanoparticles enhanced charge separation, resulting in a H_2 evolution rate of 8.59 mmol $h^{-1}g^{-1}$.[68]

Moving beyond traditional strategies, innovative approaches, such as supramolecular and van der Waals heterostructures, have also been developed to enhance photocatalytic activity for H_2 production. For example, a mechanochemically synthesized MoS_2-C_{60}-cyclodextrin (γCD) heterostructure exhibits improved water dispersibility and catalytic activity due to the synergistic effects of supramolecular interactions (Figure 4D). Similarly, the integration of C_{60} with MoS_2 via ball milling creates a van der Waals heterostructure that reduces the number of MoS_2 layers and shifts the conduction and valence bands, leading to a remarkable H_2 evolution rate of 6.89 mmol $h^{-1}g^{-1}$ under visible light irradiation. In this study, an agate mortar was used for mechanochemical synthesis. While this was a simple and solvent-free approach, its reproducibility and scalability raised significant concerns, as manual grinding may lead to inconsistencies in efficiency when compared to automated high-energy milling techniques.[70]

3.1.4. Mechanochemically-Prepared Metal-Free Catalytic Systems

Metal-free photocatalysts have garnered substantial interest for their role in visible-light-driven hydrogen (H_2) production due to their cost-effectiveness and environmental compatibility. Such systems, including modified carbon nitride, conjugated polymers, and black phosphorus, have been recently fabricated by mechanochemical synthesis. This section highlights recent advancements in the field, emphasizing defect engineering, heterojunction formation, and mechanochemical synthesis approaches.

Defect engineering and heteroatom doping are crucial strategies for enhancing the photocatalytic efficiency of g-C_3N_4 by optimizing light absorption and charge carrier behavior.

Mechanochemistry has provided a unique basis to prepare bromine-doped, carbon- and nitrogen-deficient g-C_3N_4 (CNV-mCN-Br).

In a recent study, the ball-milling process induced the formation of vacancies, facilitating Br incorporation. The resultant material exhibited a curled nanosheet morphology, enhanced electron–hole separation, and impressive hydrogen evolution rates of 22.21 and 34.41 mmol g^{-1} h^{-1} in distilled water and simulated seawater, respectively. This was corroborated by steady-state PL and Time-resolved PL decay spectra (TRPL). The reduced PL intensity and shortened average carrier lifetime (from TRPL) compared to pristine CN and mCN suggest more efficient separation and migration of photogenerated charges in the modified sample. These improvements are attributed to the synergistic effect of CNV and bromine doping, which enhances visible light absorption, narrows the bandgap, and modulates charge distribution. Additionally, the curled nanosheet morphology contributes to a higher surface area and reduced diffusion distance for charge carriers, further suppressing recombination losses and promoting photocatalytic activity. Apparent quantum yields reached 25.87% and 40.08% at 420 nm. These findings highlight the synergistic effects of defect engineering and heteroatom doping in improving photocatalytic performance.[71]

Another study demonstrated the synthesis of mesoporous g-C_3N_4 with nitrogen vacancies (mCNv) via mechanochemical processing of a melamine intermediate, followed by calcination (**Figure** 5A,B). The simultaneous formation of mesopores and nitrogen vacancies resulted in enhanced surface area, improved visible light absorption, and superior charge separation, leading to a 6.3-fold increase in photocatalytic hydrogen production compared to bulk g-C_3N_4. In this case, the mechanochemical process induced structural modifications, providing a scalable and environmentally friendly route for the development of high-performance, cost-efficient photocatalysts.[72]

Pushing this concept forward, the integration of g-C_3N_4 with carbon-based materials such as fullerene (C_{60}) has also shown promise for improving photocatalytic hydrogen evolution. Yang and coworkers reported a mechanochemical approach to covalently bond g-C_3N_4 with C_{60} using lithium hydroxide (LiOH) as a catalyst. The resultant hybrid material exhibited a hydrogen evolution rate of 266 µmol $h^{-1}g^{-1}$ under visible light, outperforming pristine g-C_3N_4 by a factor of four. The enhanced activity was attributed to improved interfacial charge transfer and increased surface area, demonstrating the potential of mechanochemical methods in fabricating covalently bonded photocatalytic hybrids.[73]

A sugar-assisted mechanochemical treatment has been recently developed as a cost-effective method for the delamination of g-C_3N_4. According to the study conducted by Liu and colleagues, the co-grinding of g-C_3N_4 with fructose facilitated the exfoliation process, yielding few-layered nanoplates with improved photocatalytic activity. The resulting material exhibited a surface area six times the value of bulk g-C_3N_4 (57.4 m^2g^{-1}), increasing exposure of active sites, and enhanced charge carrier mobility (confirmed by transient photocurrent response), leading to superior performance in hydrogen evolution and pollutant degradation.[74]

Another investigation has shown that simply mechanochemical exfoliation can effectively enhance the photocatalytic

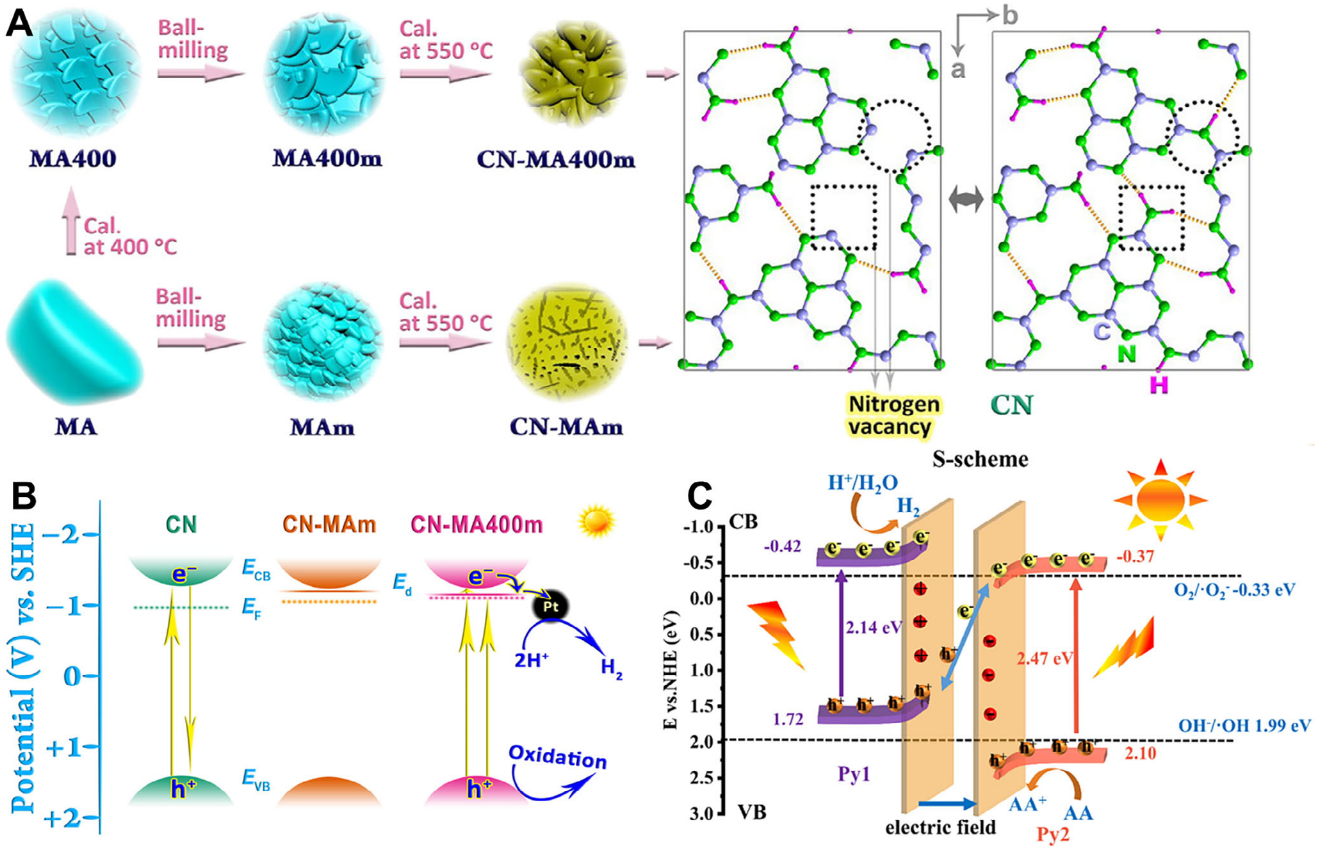

Figure 5. A) Schematic illustration of the synthesis and structural diagrams of mCNv and related intermediates. B) Energy band structures of the samples, along with photoinduced charge separation, transfer pathways, and hydrogen evolution mechanism. Reproduced with permission from ref. [72]. C) S-scheme electron transfer mechanism upon light irradiation involving two linear conjugated polymers. Reproduced with permission from ref. [76].

performance of g-C_3N_4 by reducing the layer thickness and increasing the specific surface area. A solvent-free approach developed by Pokhodenko et al. enabled the synthesis of 2D g-C_3N_4 nanoparticles with monolayer-like structures and improved electronic properties. Compared to conventional liquid-phase exfoliation, the mechanochemically processed material exhibited 1.5 times greater photocurrent response, a larger bandgap (3.07 vs 2.83 eV for bulk g-C_3N_4), and a higher hydrogen evolution rate (1326 vs 605 μmol g^{-1} h^{-1}), demonstrating the effectiveness of this approach in enhancing photocatalytic efficiency.[75]

Conjugated polymers with donor–acceptor (D–A) architectures have emerged as efficient metal-free photocatalysts. In particular, the synthesis of D–A conjugated polymers via mechanochemical techniques, followed by solvent-assisted exfoliation, has been recently explored by Tsiakaras and coworkers (Figure 5C). This study demonstrated the construction of a physical heterojunction (PHJ) by the ball-milling of two linear conjugated polymers, followed by ultrasonic treatment. Steady-state PL analysis revealed that the composite N-Py1/Py2 exhibits the lowest fluorescence intensity among all samples tested, indicating a more efficient separation of photogenerated electron–hole pairs and reduced recombination. Time-resolved fluorescence spectroscopy (TRFS) further confirmed this behavior: N-Py1/Py2 displayed significantly shorter average lifetimes compared to the other materials, suggesting enhanced charge transfer efficiency. Moreover, the instantaneous photocurrent response (IPS) showed that N-Py1/Py2 achieves the highest photocurrent density (3.40 μA cm^{-2}), indicating superior charge carrier mobility and separation efficiency. Electrochemical impedance spectroscopy (EIS) supported these findings, as the N-Py1/Py2 composite exhibited the smallest Nyquist radius among the tested samples, reflecting minimal charge transfer resistance.

Collectively, these results demonstrate that the NMP-treated N-Py1/Py2 composite forms a favorable interfacial architecture, enabling rapid and efficient photogenerated charge carrier transport, an essential feature to enhance the photocatalytic performance, achieving up to 26.5 mmol $g^{-1}h^{-1}$ without requiring a co-catalyst.[76]

Moreover, new perspectives on the use of black phosphorus as a promising metal-free photocatalyst have been explored by Yang and colleagues. Specifically, the authors reported a LiOH-assisted solid-state mechanochemical synthesis of BP nanosheets, which resulted in enhanced visible-light-driven hydrogen evolution activity. The BP nanosheets displayed a hydrogen production rate of 512 μmol $h^{-1}g^{-1}$, significantly outperforming bulk BP and even surpassing some g-C_3N_4-based materials. The enhanced photocatalytic efficiency was attributed to hydroxyl-terminated edges that facilitated charge carrier separation.[77]

In summary, the synthesis of metal-free photocatalytic materials, which are crucial for advancing renewable energy technologies, largely benefits from mechanochemical engineering, particularly for their structural and electronic properties.

3.1.5. Mechanochemically-Prepared Perovskites

Metal halide perovskites (MHPs) have gained attention as semiconductors due to their outstanding optical properties, including strong visible-light absorption, tunable bandgaps, and extended charge carrier lifetimes.[78,79] These characteristics make them attractive for applications in photovoltaics and optoelectronics.[80] More recently, their potential has expanded into the realm of solar-driven photocatalysis, particularly for hydrogen (H_2) photoproduction. Unlike conventional metal oxide photocatalysts, MHPs feature narrower bandgaps, enabling efficient utilization of low-energy photons. Their electronic band structures are also well-suited for photocatalytic reactions, such as hydrogen evolution and CO_2 reduction. However, a key challenge limiting their practical implementation is the intrinsic instability of many MHPs in aqueous or polar environments, which is particularly problematic since water is essential for crucial photocatalytic reactions like H_2O splitting and CO_2 reduction.[81,82] To address this limitation, various stabilization strategies have been explored, including the use of saturated halo acids, low-polarity solvents, and encapsulation techniques.[83] For instance, hydrogen photogeneration using methylammonium lead iodide ($MAPbI_3$) has proved successful, but only in the presence of aqueous hydrogen iodide (HI) to maintain structural stability.[84–87] While effective, these approaches highlight the need for more robust and environmentally friendly alternatives.

A major breakthrough in this direction has been the development of water-stable MHPs, recently achieved by introducing materials such as dimethylammonium tin halides ($DMASnX_3$, where X = Br or I).[88,89] These materials retain their structural integrity and optical properties even after prolonged water exposure, a stability attributed to the hydrophobic nature of the dimethylammonium cation. Unlike conventional MHPs, these tin-based perovskites can function as photocatalysts for H_2 evolution in deionized water without requiring strongly acidic conditions. Other water-stable perovskite systems, such as $C_{22}H_{18}N_2(PbI_3)_2$ and hydroxyl ammonium lead halides ($OHNH_3PbI_2Cl$, $OHNH_3PbCl_3$), have also demonstrated remarkable resistance to degradation, with some maintaining stability for extended periods, up to 45 days.[88,89] Lead-free 2D perovskites, such as phenylethylammonium tin bromide (PEA_2SnBr_4), have also shown exceptional stability in water. Instead of dissolving, these materials remain dispersed while preserving their structural and optical properties. Computational studies suggest that the layered structure of 2D perovskites contributes to their resistance against oxidation and degradation.[88,89]

A significant advancement in perovskite synthesis was pioneered by Gustavo de Miguel and colleagues, who were among the first that demonstrate the viability of mechanochemistry for hybrid perovskite fabrication. Their study introduced a solvent-free, scalable approach using ball milling to produce polycrystalline perovskite powders under ambient conditions. By milling lead iodide (PbI_2) with organic halides such as methylammonium iodide (MAI), formamidinium iodide (FAI), or guanidinium iodide (GuaI) in equimolar ratios, a rapid, reproducible method was developed by which the need for solvents typically used in conventional solution-based techniques was eliminated (**Figure 6**). Further characterization of these mechanochemically synthesized perovskites by X-ray photoelectron spectroscopy (XPS) confirmed their stoichiometric integrity. Notably, XPS revealed the absence of metallic Pb, a common defect in perovskites synthesized via solvent-based routes. Since metallic Pb is linked to iodide deficiencies, its absence suggests an improvement of the optoelectronic properties of these materials. Scanning electron microscopy (SEM) analysis demonstrated that the resulting particle size ranged from 10 to 200 µm, indicating a reduction in surface and bulk defects compared to their solution-processed counterparts. This defect minimization could significantly enhance both the stability and performance of perovskite-based devices.[90]

Recent breakthroughs in lead-free MHPs have expanded their potential for photocatalytic applications. For instance, coupling $DMASnBr_3$ with g-C_3N_4 has led to the development of composite materials with exceptional photocatalytic activity for H_2 evolution in aqueous environments. The mechanochemical synthesis of $DMASnBr_3$ has been designed starting with the ball milling of stoichiometric mixtures of dimethylammonium bromide (DMABr) and tin(II) bromide ($SnBr_2$) at 300 rpm for 12 h. This process induced the formation of a crystalline perovskite structure characterized by distorted edge-sharing $SnBr_6$ octahedra, as confirmed by X-ray diffraction analysis. The ball milling method not only simplified the synthesis but also ensured high phase purity and crystallinity, which are critical factors for optimizing the material's optical and electronic properties. Extending this mechanochemical approach, a composite material with enhanced photocatalytic performance was successfully fabricated by incorporating-C_3N_4 with $DMASnBr_3$. The mechanical energy supplied during milling favored an intimate contact between the two components, which proved crucial to promote efficient charge transfer and separation. The resulting composite achieved an impressive hydrogen evolution rate exceeding 1700 µmol $g^{-1}h^{-1}$ under visible-light irradiation, driven by the synergistic interaction between the perovskite and g-C_3N_4. DFT calculations suggested that the enhanced performance arises from favorable interfacial energy level alignment, which facilitated efficient charge separation and transport.[91]

These studies are paving the way for the development of more efficient lead-free and water-stable photocatalytic systems for visible-light-driven H_2 production.

3.1.6. Mechanochemically-Prepared MOFs

Metal–organic frameworks have emerged as promising materials for visible-light-driven H_2 photoproduction, owing to their exceptional photoactive and electroactive properties.[92,93] While numerous studies have investigated MOFs for the hydrogen evolution reaction (HER), these materials are typically synthesized through solution-based methods rather than mechanochemistry.[94–98] Nevertheless, recent advances in mechanochemical synthesis have demonstrated the potential to

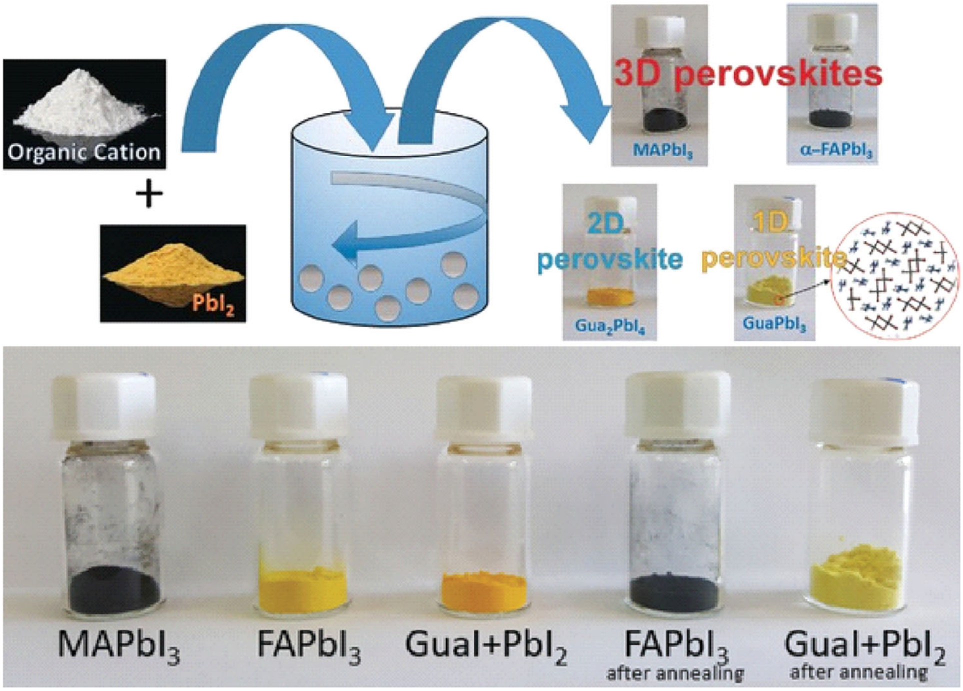

Figure 6. Illustrative representation of the mechanochemical synthesis of 3D, 2D, and 1D hybrid perovskites. Reproduced with permission from ref. [90].

enhance the photocatalytic performance of MOFs by optimizing their interfacial properties, charge carrier dynamics, and stability under visible light irradiation. This section highlights key developments in the field, focusing on MOF-based hybrids incorporating graphdiyne (GDY), perovskite nanocrystals, and single-atom catalysts for sustainable H_2 production.

Interface engineering has proven to be a powerful strategy to enhance the photocatalytic activity of MOFs. Zhiliang Jin et al. investigated an interface-engineered MOF-on-MOF strategy to construct ZIF-9(Co)/Cu_3BTC_2 (namely a heterojunction between ZIF-9(Co) and Cu_3BTC MOFs).[99] The hydrogen evolution kinetics and charge carrier behavior of the catalysts were investigated using steady-state PL and TRPL spectroscopy. The incorporation of GDY into this heterostructure enabled interfacial carrier migration, thereby improving photogenerated charge transfer (average lifetime of 1.1070 ns instead of 0.0288 ns) while preserving active sites and surface area (28.08 m^2g^{-1}). The formation of an S-scheme heterojunction within the composite contributed to strong reduction activity and accelerated charge migration via GDY's electron relay effect, enhancing hydrogen evolution. This study underscored the potential of GDY-functionalized MOFs in sustainable photocatalysis, but the approach used largely relied on solution-based synthesis methods.[100]

Similarly, Wang et al. developed a GDY/ZnCo-ZIF S-scheme heterojunction photocatalyst via a low-temperature blending method, composed of graphdiyne and ZnCo-ZIF MOF.[100] When sensitized with eosin Y (EY), the composite achieved a notable hydrogen production of 171.79 µmol, significantly outperforming its individual components. The heterojunction design facilitated efficient charge separation, while the EY sensitization provided an additional source of excited electrons for the reduction reaction. Steady-state photoluminescence (PL) and time-resolved PL (TRPL) analyses were performed to investigate charge carrier dynamics in the GDY/ZnCo-ZIF system. The addition of GDY to ZnCo-ZIF significantly reduced PL intensity compared to the individual components, indicating suppressed electron–hole recombination. TRPL measurements further confirmed this, as the GDY/ZnCo-ZIF composite showed the shortest average fluorescence lifetime, suggesting accelerated charge transfer at the interface and reduced carrier residence time in the excited state. Despite these advantages, the synthesis of ZnCo-ZIF and its composites was solution-based, with major issues related to solvent waste and process sustainability.[100] An alternative strategy for improving the stability and performance of MOF-based photocatalysts was explored by Sitong Feng et al., who developed a $CsPbX_3$@ZIF-8 composite via mechanical milling. This approach enabled large-scale synthesis while enhancing the stability of $CsPbX_3$ perovskite nanocrystals: these materials preserved 86.7% of their photoluminescence (PL) intensity over eight weeks. The synergy between ZIF-8 and $CsPbX_3$ improved charge separation, leading to a substantial increase in photocatalytic H_2 evolution up to 19.63 µmol g^{-1} after 2.5 h (**Figure** 7).[101]

Single-atom catalysis was explored for MOF-based H_2 production. Yulu Wu et al. developed a CdS/Fe-MOF-525 composite via ball milling, wherein Fe single atoms were anchored to MOF ligands. PL and TRPL analyses demonstrated improved charge separation in CdS/Fe-MOF-525 composites, particularly in the sample with a 2.3:1 CdS:MOF ratio, which exhibited the lowest PL intensity and the longest average carrier lifetime (22.38 ns). This enhancement is attributed to efficient ligand-to-metal and metal-to-semiconductor charge transfer at the interface. Complementary photocurrent measurement confirmed these findings, since

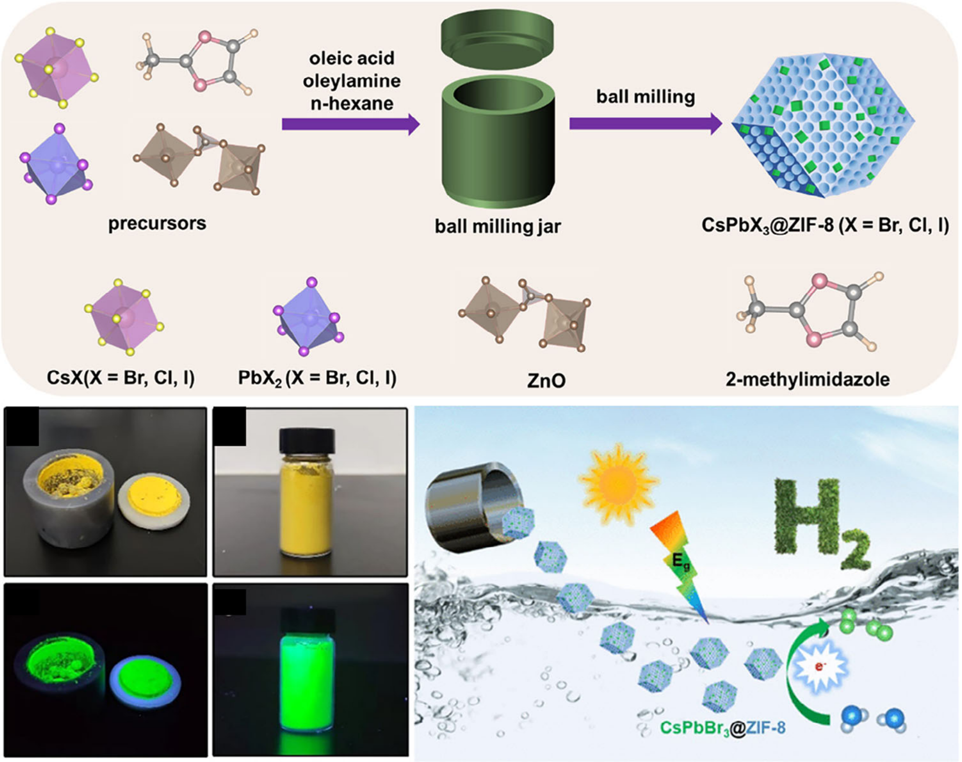

Figure 7. Illustration of the mechanochemical synthesis of the $CsPbBr_3$@ZIF-8 composite, along with real images of the ball-milling jar used for the synthesis of the $CsPbBr_3$@ZIF-8 composite under visible and UV light. also shown is the representation of hydrogen photoproduction over $CsPbBr_3$@ZIF-8. Reproduced with permission from ref. [101].

CdS/Fe-MOF-525-2.3 showed the highest photocurrent density, indicating more effective charge transport compared to both pristine CdS and other composite ratios. The composite exhibited a hydrogen evolution rate of 3638.6 µmol g^{-1} h^{-1}, surpassing the performance of its individual components. This investigation highlights the synergistic effects of MOF-quantum dot heterojunctions in photocatalysis.[102]

While significant progress has been made in visible-light-driven H_2 photoproduction using MOFs, several challenges remain. The synthesis of MOF-based composites often involves solvent-based methods, which are inconsistent with the principles of green/sustainable chemistry. Mechanochemical approaches, such as ball milling or extrusion, could offer an attractive alternative.[103,104] Additionally, the long-term stability and recyclability of these materials under operational conditions need to be addressed to ensure their practical applicability. By addressing the current challenges and leveraging the unique properties of MOFs, researchers can unlock the full potential of these materials for advancing renewable energy technologies.

DFT analyses have provided critical insights into charge transfer mechanisms and the fundamental properties of photocatalytic materials, offering a robust theoretical foundation for experimental observations. In particular, DFT calculations have confirmed the S-scheme charge transfer mechanism in heterojunctions such as CoS_2/GDY and GDY/$Sr_2Co_2O_5$, by determining work functions (GDY: 5.113 eV, CoS_2: 5.312 eV, and GDY: 5.06 eV, SCO: 6.04 eV, respectively) and Fermi level differences that drive electron migration and the formation of internal electric fields.[63,64] Moreover, phosphorus doping in g-C_3N_4 (PCN) has been shown to narrow the band gap (from 1.23 to 1.05 eV) and introduce an empty mid-gap state, thereby enhancing light absorption and electron transport.[66] DFT simulations also revealed electron transfer across the PCN/MoP heterojunction, confirming Schottky barrier formation and calculating a Gibbs free energy for hydrogen adsorption ($\Delta GH^* = +0.129$ eV) close to thermoneutral, indicating weak but favorable hydrogen binding kinetics, an essential feature for promoting efficient photocatalytic H_2 evolution.[66] Additionally, DFT studies on MoS_2 nanoparticles have shown that the projected density of states is predominantly governed by Mo 4*d* and S 3*p* orbitals, facilitating charge transport across the catalyst. The calculated conduction and valence band edge positions (−0.39 and +1.31 V, respectively) further align with the energetic requirements for visible-light-driven photocatalysis, highlighting the suitability of MoS_2-based heterostructures for efficient solar conversion.[70]

Further DFT investigations have expanded the understanding of heterojunction behavior, dopant effects, and surface stability across diverse photocatalytic systems. In BP-$MoO_{3\text{-}x}$ heterostructures, DFT simulations indicated metallic character in $MoO_{3\text{-}x}$ and predicted a substantial band gap narrowing (from 1.43 eV in BP to 0.5 eV in the composite) due to Mo-P interactions, enhancing photoexcited charge mobility. These findings, combined with plasmonic enhancement from $MoO_{3\text{-}x}$, support a Z-scheme mechanism and improved light harvesting.[69] In metal cluster-TiO_2 interfaces, DFT revealed that Pt exhibits the highest adsorption energy and lowest aggregation tendency, particularly on the

Table 1. Summary of mechanochemically prepared materials and their applications in H_2 photoproduction.

Entry	Material	Milling conditions (Speed/time)	Apparent quantum efficiency [%]	H_2 evolution rate [µmol g^{-1}h^{-1}]	Refs.
1	Au/TiO_2	Manual/10 min	nr	500	[39]
2	Au/TiO_2	Manual/10 min	nr	500	[40]
3	Au/TiO_2-550	29.5 Hz/10 min	nr	19 800	[41]
4	Au/P90-BM	15 Hz/10 min	0.3	49 300	[42]
5	Pd/TiO_2	15-50 Hz/up to 2 h	14	86 700	[43]
6	0.5%Pt-0.5%Cu-2%rGO-TiO_2	15 Hz/3 min[a]	3.17	27 000	[53]
7	Cu/TiO_2	300 rpm/15 min	nr	9500	[54]
8	NiO/P90-BM	15 Hz/10min	nr	8850	[58]
9	4.0%MoS_2/TiO_2	300 rpm/4 h	nr	150.7	[59]
10	self-doped $BaTiO_3$	300 rpm/1 h	nr	191.3	[60]
11	$MgFeTiO_3$	600 rpm/2 h	nr	296	[61]
12	Cu_3P@GDY	250 rad min^{-1}/6 h[a]	3.03	1270	[62]
13	CoS_2/GDY	500 rad min^{-1}/10 h[a]	1.16	1835	[63]
14	Graphdiyne/$Sr_2Co_2O_5$	nr/10 h[a]	1.76	157	[64]
15	Ni_2P/g-C_3N_4	400 rpm/2 h	nr	129	[65]
16	g-C_3N_4/BP/MoS_2	1000 rpm/1 h	9.71	2146.8	[67]
17	CN/BP@Ni	200 rpm/5 h	1.8	8590	[68]
18	MoS_2-C_{60}-cyclodextrin	Manual/10 min	nr	6890	[70]
19	1%Pt-CNv-mCN-Br	500 rpm/30 min[a]	40.08	34 410	[71]
20	mCNv	1500 rpm/6 h	5.4	529	[72]
21	g-C_3N_4/C_{60}	500 rpm/24 h	6.97	266	[73]
22	g-C_3N_4	160 rpm/2.5 h	nr	103.7	[74]
23	2D g-C_3N_4	500 rpm/1 h	nr	1326	[75]
24	N-Py1/Py2	nr/12 h	6.9	26 500	[76]
25	BP nanosheets	250 rpm/24 h	0.47	512	[77]
26	3%Pt-DMASnBr_3@g-C_3N_4	300 rpm/12 h	6.6	1730	[91]
27	Cu_3BTC_2/ZIF-9(Co)/GDY	500 rpm/10 h[a]	nr	1126	[99]
28	GDY/ZnCo-ZIF-0.9	250 rad min^{-1}/6 h[a]	2.8	34.4	[100]
29	$CsPbX_3$@ZIF-8	Manual/1 h	nr	7.9	[101]
30	CdS/Fe-MOF-525	30Hz/2-9 h	nr	3638.6	[102]

[a] A mechanochemical step was involved only in the synthesis of one component of the reported material. nr: non-reported.

{001} facet, maintaining superior stability and HER activity even under photoexcitation.[44] For conjugated donor–acceptor polymers (Py1/Py2), DFT optimized molecular segments and identified bisulfone oxygen atoms as hydrogen adsorption sites, although with high ΔG_H values indicating limited intrinsic catalytic activity.[76] Finally, in Br-doped and C/N-deficient g-C_3N_4 (CNV-mCN-Br), DFT confirmed preferential Br substitution at N_2 sites and demonstrated complete spatial separation of HOMO and LUMO orbitals, correlating with reduced charge recombination and enhanced carrier dynamics.[71]

Table 1 presents some of the key findings on mechanochemically prepared materials and their applications in H_2 photoproduction, along with the corresponding milling conditions.

3.2. Visible-Light-Driven CO_2 Photoreduction

The utilization of solar energy to drive the photocatalytic reduction of CO_2 is among the most investigated approaches toward the sustainable production of fuels.[105] This process involves the conversion of CO_2 into value-added hydrocarbons such as methane (CH_4), carbon monoxide (CO), methanol (CH_3OH), and other reduced carbon species, and at the same time, it represents a viable strategy to mitigate greenhouse gas emissions.

The activation of a thermodynamically stable and inert species as CO_2, requires a substantial energy input that in conventional processes is achieved through high-temperature and high-pressure catalytic reactions.[106,107]

However, photocatalysis provides a low-energy alternative, enabling CO_2 conversion under ambient conditions.[108] The interaction of CO_2 with the photocatalyst surface is crucial in determining its reduction pathway. Upon adsorption, CO_2 molecules may undergo charge transfer interactions, leading to the formation of activated intermediates ($CO_2^{\cdot-}$, $^{\cdot}$COOH, $^{\cdot}$CHO) that facilitate subsequent reduction steps.[109] The adsorption mode, whether through monodentate carbon coordination, bidentate oxygen coordination, or mixed coordination, directly impacts the preferred reaction pathway and the final product selectivity.[110,111]

In this field, mechanochemically synthesized photocatalysts have demonstrated their potential for the CO_2-to-CH_4 conversion. The mechanochemical synthesis, which often involves high-energy ball milling, offers several advantages, including enhanced crystallinity, defect engineering, and improved charge carrier dynamics.

A crucial requirement for photocatalytic CO_2 reduction is the optimization of the band structure of the photocatalyst. For an effective charge transfer, the conduction band minimum (CBM) must be more negative than −0.24 V versus RHE, while the valence band maximum (VBM) must be more positive than +0.82 V versus RHE, ensuring a driving force enough for CO_2 reduction and water oxidation.[109] Rational catalyst design, including bandgap tuning, defect passivation, and nanostructuring, plays a pivotal role to improve both the activation of CO_2 and the CH_4 selectivity.

3.2.1. Mechanochemically-Modified Titania-Based Materials

Metal oxides, including TiO_2, have been widely employed as supports for photocatalytic CO_2 reduction, due to their well-established photoactivity.[112,113] Ruofei Tang et al. utilized TiO_2 as a support for synthesizing various single-atom catalysts (SACs) through a mechanochemical approach.[114] The synthesis was performed using a planetary ball mill, where TiO_2 (P25) was combined with metal chloride precursors (MCl_n, where M = Pd, Bi, Y, Er, Cu, Na, etc.) in deionized water, while hydrochloric acid (HCl) was used to adjust the pH to 0.0–4.0. To achieve homogeneous atomic dispersion, balls of three different sizes were utilized, and the process was carried out at 400 rpm for 12 h. The use of an agate grinding medium dissipated excess heat, maintaining the reaction temperature below 35 °C and preventing unwanted metal oxidation. X-ray diffraction (XRD) analysis of each material confirmed that only TiO_2 diffraction peaks were present. This indicated that metallic nanoparticles were absent and suggested that atomically dispersed metal species formed within the TiO_2 matrix. UV–vis diffuse reflectance spectroscopy (DRS) revealed that all metal single atom supported samples (M_{SA}/TiO_2) maintained strong UV absorption (≈3.0–3.1 eV band gap). However, catalytic activity was influenced by the electronic properties of the incorporated metal sites, rather than significant changes in optical absorption. The generation and separation of photoinduced charge carriers were assessed via electron paramagnetic resonance (EPR) and TRFS measurements. EPR spectra revealed that $PdSA/TiO_2$ exhibits a markedly enhanced generation of photoexcited electrons under light irradiation compared to $CuSA/TiO_2$, indicating superior charge separation and transport efficiency. Complementarily, TRFS measurements confirmed these findings, with $PdSA/TiO_2$ exhibiting the most significant quenching of fluorescence lifetime, indicative of faster charge carrier separation and suppressed recombination dynamics.

Among the synthesized SACs, Pd single-atom catalyst ($PdSA/TiO_2$) exhibited the highest CO_2 photoreduction activity, achieving a CH_4 production rate of 271.6 $\mu mol\ g^{-1} h^{-1}$ with ≈98% selectivity. This performance far exceeded that of previously Pd nanoparticle-based TiO_2 catalysts synthesized via conventional impregnation methods.[115] This result was explained by mechanistic studies using in situ Fourier-transform infrared (FTIR) spectroscopy and DFT calculations. These demonstrated that single-atom Pd sites strongly adsorbed CO_2, inducing significant structural bending of the O═C═O bond from 180° to 151°. This strong distortion lowered the activation energy barrier for CO_2 reduction, thereby facilitating its conversion into methane (CH_4) with high efficiency.[114] Overall, the proposed mechanochemical method offered a straightforward, high-yield, and scalable strategy for fabricating single-atom metal catalysts without thermal treatments, additives, or post-synthetic modifications, which not only simplified the synthesis process but reduced costs.

3.2.2. Mechanochemically-Prepared Gallium-Based Materials

Among metal oxides, gallium-based materials are becoming more and more popular as photocatalysts for energy conversion applications. Li Qin Zhou et al. synthesized a Sr_2GaCoO_5 sample via a solid-state reaction method, involving ball milling of $SrCO_3$, Ga_2O_3, and Co_3O_4, followed by calcination and sintering of the resulting mixture.[116] XRD and HAADF-STEM confirmed the formation of a high-purity orthorhombic brownmillerite phase, characterized by alternating CoO_6 octahedra and GaO_4 tetrahedra. When integrated into a bipolar membrane-free (BPM-free) electrolysis cell with an anodized silver cathode, Sr_2GaCoO_5 enabled a remarkable solar-to-CO conversion efficiency of 13.9%. The catalyst exhibited exceptional durability, maintaining its activity for over 19 h of continuous operation without significant performance loss. This result was attributed to the stabilization of intermediate-spin Co^{3+} ($t_{2g}{}^5 e_g{}^1$) states within the Brownmillerite framework.[117] This optimized electron occupancy in the e_g orbitals enhances the oxygen evolution reaction (OER) kinetics and facilitates more efficient charge transfer. Additionally, the incorporation of gallium (Ga^{3+}) into the structure contributed to high chemical stability, effectively preventing metal leaching and preserving the structural integrity of the catalyst in neutral pH environments.

Similarly, Tomomi Aoki et al. investigated the photocatalytic performance of mixed-phase gallium oxide materials, specifically $GaOOH/\beta\text{-}Ga_2O_3$ and $\alpha\text{-}Ga_2O_3/\beta\text{-}Ga_2O_3$, for CO_2 reduction using water as a proton source.[118] The synthesis of $GaOOH/\beta\text{-}Ga_2O_3$ was conducted via high-energy ball milling, using $\beta\text{-}Ga_2O_3$ in water at 400 rpm for various durations. This led to the formation of GaOOH fine particles whose amount increased with the milling time, albeit their specific surface area did not exceed 40 $m^2\ g^{-1}$. Subsequent calcination at 773 K transformed GaOOH into $\alpha\text{-}Ga_2O_3$. An oxide mixture comprised of $\alpha\text{-}Ga_2O_3/\beta\text{-}Ga_2O_3$ was achieved. Under UV irradiation, this material displayed a CO_2 photoreduction activity up to six times higher than that of pure $\beta\text{-}Ga_2O_3$. The H_2 evolution rate was positively correlated with the specific surface area, indicating that both GaOOH and $\alpha\text{-}Ga_2O_3$ contributed to H_2 generation. Notably, CO formation was significantly enhanced only in the $\alpha\text{-}Ga_2O_3/\beta\text{-}Ga_2O_3$ system, suggesting that distinct active sites within this phase mixture played a crucial role in CO_2 reduction.

The authors proposed a redox-type reaction mechanism, where GaOOH was reduced to $\alpha\text{-}Ga_2O_3$ under UV irradiation, generating both H_2 and O_2. In contrast, during dark conditions, $\alpha\text{-}Ga_2O_3$ reverted to GaOOH upon interaction with water, completing the catalytic cycle. The phase boundaries between the different Ga_2O_3 phases were identified as key factors in enhancing charge separation and electron transfer, which are essential for improving catalytic efficiency. Despite the promising CO_2 reduction performance, the CO selectivity of the catalysts remained relatively low. The authors suggested that incorporating a Ag cocatalyst could further improve the selectivity and overall CO_2 conversion efficiency, as reported in previous studies.[119]

This study highlighted the effect of ball milling duration on changing/enhancing the catalytic performance of gallium-based materials. Although this work employed UV irradiation rather than solar light and thus did not meet the primary scope of this review, the strategic application of mechanochemistry justified its inclusion.[120]

3.2.3. Mechanochemically-Prepared Nano- and Atomic-Scale Metal Catalysts on Carbonaceous Materials

g-C_3N_4 has been recently recognized as an ideal support for SACs.[121–123] Its specific surface area and the presence of lone pairs of electrons in the N atoms facilitate strong metal-support interactions, which may prevent the agglomeration of single atoms. The current literature reports some remarkable contributions of mechanochemistry in the preparation of g-C_3N_4-based highly dispersed SACs.

Tang et al. developed single-atom Ni catalysts on g-C_3N_4 (Ni/CN) for photocatalytic CO_2 reduction (CO_2RR) via a solvent-free, high-energy ball milling method at 400 rpm for 12 h, where the reagents were mixed together with water and HCl (to maintain pH 0–3).[124] This procedure ensured a uniform dispersion of Ni atoms on the g-C_3N_4 surface without the formation of clusters or nanoparticles (**Figure** 8A), as confirmed by HAADF-STEM analysis.

The optimized photocatalyst, Ni/CN-0.5 (0.5 at% Ni, 0.32 wt.%), exhibited the highest CO_2 reduction performance (19.9 µmol g^{-1} h^{-1}) under simulated solar irradiation, operating without additional co-catalysts or sacrificial agents. The strong Ni–N (metal-support) interaction achieved by mechanochemical synthesis enabled the activation of CO_2 molecules, thereby increasing both the generation of photoexcited electrons and charge separation efficiency.[125–128] Under illumination, the well-dispersed Ni(II) active sites were responsible for: i) capturing photoelectrons from g-C_3N_4; ii) promoting the separation of photogenerated electron–hole pairs; iii) accelerating the diffusion of charge carriers to the catalyst surface, and ultimately iv) reducing kinetic barriers and enhancing CO_2 photoreduction efficiency. DFT calculations further confirmed that Ni single atoms as active centers lowered the reaction energy barrier and selectively drove the CO formation.[129,130]

Furthermore, Tang et al. also synthesized single-atom Cu and Zn photocatalysts supported on g-C_3N_4 using a high-energy ball milling method. To achieve atomic dispersion, $CuCl_2$ or $ZnCl_2$ was milled with g-C_3N_4 in the presence of agate balls, water, and 6.0 M HCl, adjusting the pH to 0.0–3.0.[131] The mixture underwent 10–12 h of milling at 400–500 rpm, ensuring uniform metal incorporation into the g-C_3N_4 framework. Photocatalytic CO_2 reduction tests revealed that Zn-CN-0.5 (containing 0.35 wt.% Zn) achieved a CO production rate of ≈21.1 µmol g^{-1} h^{-1} with ≈100% selectivity, whereas Cu-CN-0.5 exhibited a lower CO yield (≈15.2 µmol g^{-1} h^{-1}) but a greater activity for CH_4 formation. DFT calculations provided insights into the role of electronic configuration in determining photocatalytic selectivity. Authors concluded that Zn^{2+} ($3d^{10}$) with a fully occupied inner electron shell possessed a stable electronic structure, while its vacant outer orbitals served as electron traps to enhance charge separation efficiency and CO_2 adsorption and activation. This configuration favored the breaking of intermediate bonds, directing the reaction toward CO formation and improving overall catalytic performance and selectivity.

In contrast, Cu^{2+} ($3d^9$) exhibited an incomplete electron configuration, which made it prone to electron capture, promoting its reduction to Cu^+ under light irradiation. The strong electron affinity of Cu^{2+} facilitated proton migration, leading to H^+ accumulation at Cu^+ sites. This, in turn, promoted CH_4 formation and reduced CO selectivity. The difference in electronic stability between Zn^{2+} and Cu^{2+} ultimately dictated their reaction pathways, with Zn and Cu favoring the production of CO and CH_4, respectively (Figure 8B,C).

Although the literature reports various carbon-based materials synthesized via mechanochemistry—such as graphdiyne and reduced graphene oxide (RGO)—and some of these conventionally synthesized materials have also been employed in photocatalytic CO_2 reduction reactions,[132] there remains a notable gap concerning the use of mechanochemical protocols to prepare metal catalysts supported on carbonaceous materials other than graphitic carbon nitride.

g-C_3N_4 has not only been widely employed as a support for metal catalysts, but its 2D polymeric semiconductor structure, featuring sp^2-hybridized carbon and nitrogen atoms similar to graphene, makes it an ideal candidate for constructing Van der Waals heterojunctions valuable for CO_2 photoreduction.[133–135] Jintao Dong et al. (2024) developed a CPDs/KCNNS heterojunction photocatalyst by integrating carbonized polymer dots (CPDs) with potassium-doped carbon nitride nanosheets (KCNNS) using a mechanochemical ball milling approach.[136] This method enhanced charge separation and boosted CO_2 reduction performance without requiring additional co-catalysts or sacrificial agents. The ball milling process involved two main steps: i) a mixture of bulk g-C_3N_4, KCl, and LiCl was milled in an agate jar at 1200 rpm for 30 min, obtaining KCNNS; ii) then, a precise amount of CPDs was mixed with KCNNS and 1 mL of ethanol, and ball milling was continued at 1200 rpm for 120 min. the resulting CPDs/KCNNS composite was finally dried under vacuum. The photoelectrochemical properties of the as-prepared materials were evaluated using a combination of complementary techniques. The PL intensity was significantly quenched in CdS/Fe-MOF-5252.3, indicating improved charge separation efficiency. This was further supported by time-resolved PL, which showed extended average lifetimes with increasing CdS content. The photocurrent response under periodic illumination confirmed enhanced charge transport, particularly for the 2.3:1 composite.[136]

The photocatalytic mechanism was investigated through DFT calculations and in situ FTIR analysis, which identified COOH* as a key intermediate in the CO_2 reduction pathway (**Figure** 9A). The study confirmed the formation of a type-II heterojunction, where photoexcited electrons from CPDs migrated to the

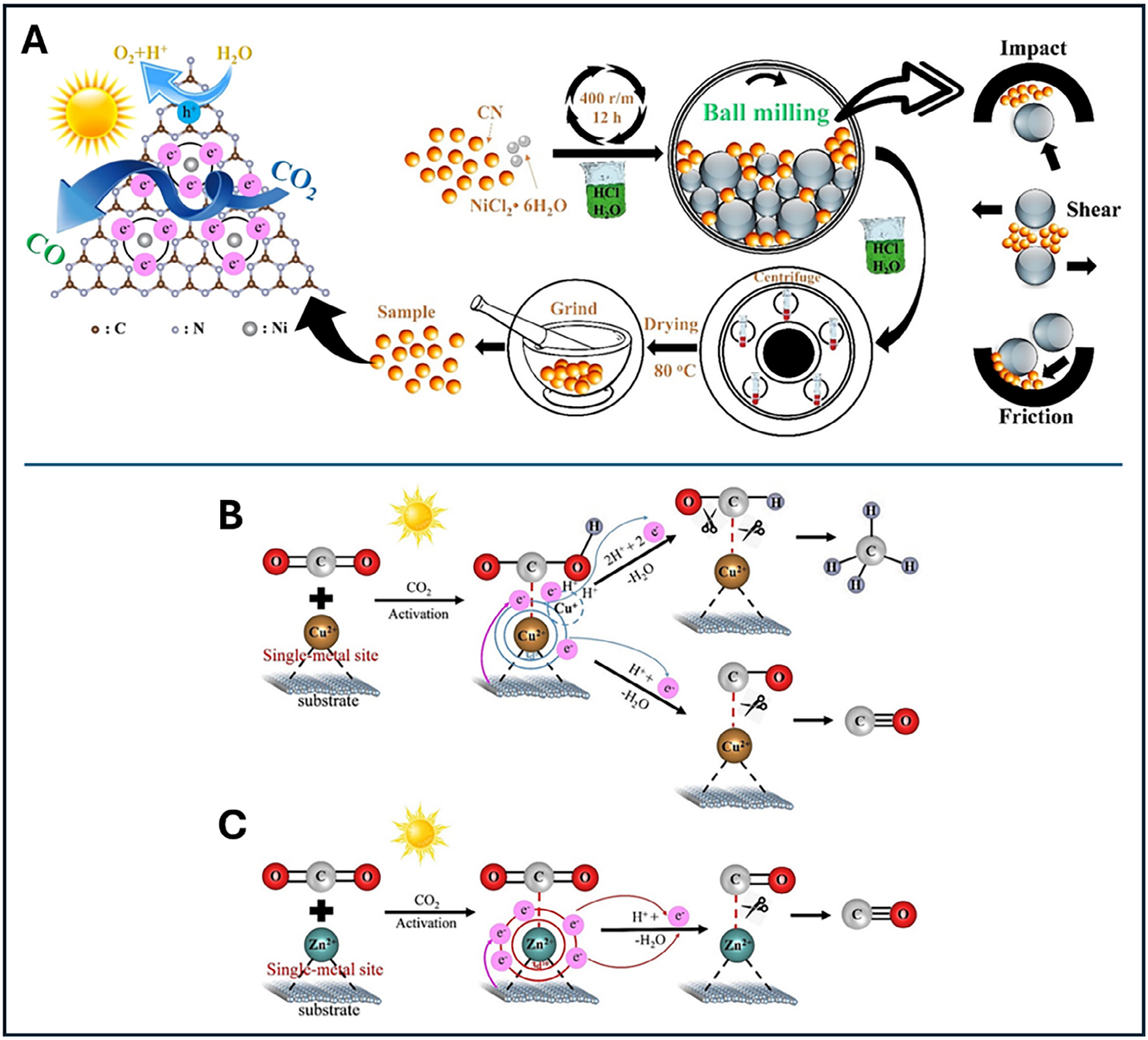

Figure 8. A) Schematic representation of material synthesis via high-energy ball milling and CO_2 photoreduction. Reproduced with permission from ref. [124]. B,C) Schematic representation of the role of different Cu^{2+} and Zn^{2+} electron configurations in the CO_2 photoreduction mechanism. Cu sites (B) facilitate CH_4 formation via dynamic Cu^{2+}/Cu^+ redox cycling and strong CO adsorption, while Zn^{2+} centers (C) act as electronic traps with weakened Zn–C bonding, promoting efficient CO desorption. Reproduced with permission from ref. [131].

conduction band (CB) of KCNNS, facilitating CO_2 reduction, while holes transferred in the opposite direction, minimizing charge recombination and enhancing photocatalytic efficiency.

The formation of the Van der Waals heterojunction improved charge separation efficiency, while the incorporation of CPDs enhanced CO_2 adsorption and extended light absorption. As a result, at 400 nm, the CPDs/KCNNS-2 composite achieved a CO evolution rate of 78.98 μmol g^{-1} h^{-1} with 100% selectivity for CO production in pure water, without requiring co-catalysts, hole scavengers, or organic solvents. This performance represents a 13.71-fold increase compared to pristine KCNNS (Figure 9B). Finally, the CPDs/KCNNS-2 composite exhibited excellent stability and photocatalytic activity over multiple cycles, underscoring its potential for long-term application in solar-driven CO_2 conversion.

3.2.4. Mechanochemically-Prepared Metal-Free Catalytic Systems

Recent advancements in CO_2 photoreduction have expanded beyond metal-based materials, with increasing attention on metal-free systems. In this context, Na Yang et al. developed an innovative mechanochemical synthesis for the direct conversion of elemental sulfur (S_8), typically considered an industrial byproduct,

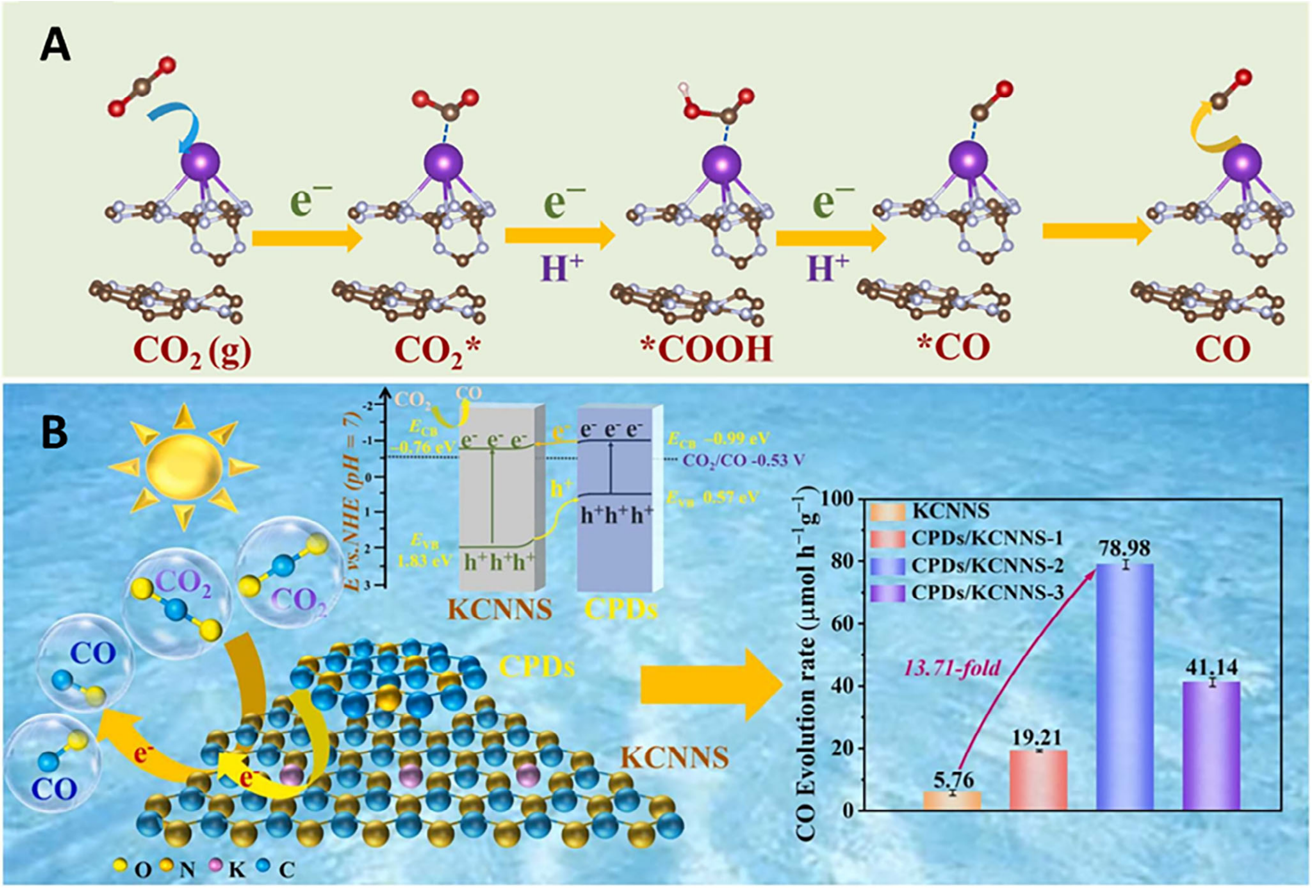

Figure 9. A) Schematic CO_2 photoreduction mechanism. B) Representation of the band structure of the CPDs/KCNNS-2 composite and a comparison of the different CO production rates. Reproduced with permission from ref. [136].

into porous donor–acceptor (D–A) ladder polymer networks.[137] This solvent-free approach eliminated the need for complex purification processes and offered a scalable method to produce photocatalysts for CO_2 photoreduction. The polymers were synthesized via nucleophilic aromatic substitution (SNAr) by ball-milling elemental sulfur (S_8) with 1,2-dihaloarenes in the presence of Cs_2CO_3 as a base. The reaction was carried out in a zirconia (ZrO_2) jar with zirconia balls at 30 Hz, either under nitrogen or ambient air. By adjusting the milling time to 2 h, the sulfur content, and the base concentration, the yield and the surface area of the polymer reached 68.7% and 823 $m^2\ g^{-1}$, respectively. The resulting polymer featured bent thianthrene units, essential for efficient charge separation (**Figure 10**).

The CO_2 photoreduction performance of the ball-milled polymer (HAT-S) was compared to an analogous polymer (HAT-N), which incorporated phenazine units instead of thianthrene and was synthesized using a solvothermal method. Under visible-light irradiation, HAT-S achieved a CO production rate of 306.1 $\mu mol\ g^{-1}h^{-1}$ with ≈100% selectivity, significantly surpassing HAT-N (82.7 $\mu mol\ g^{-1}\ h^{-1}$). This result was attributed to

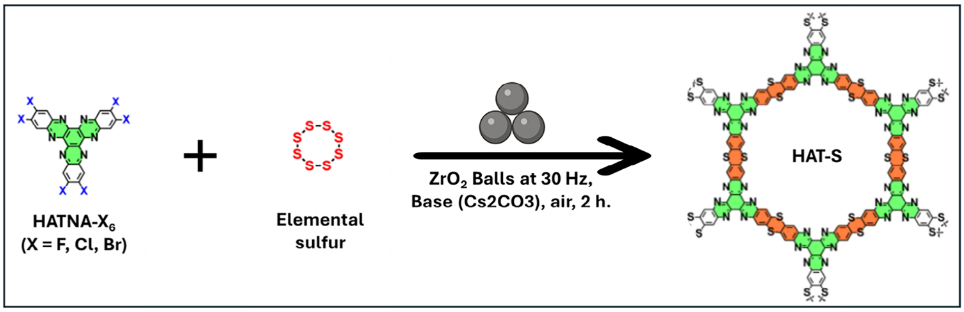

Figure 10. Schematic representation of thianthrene-bridged donor–acceptor (D–A) porous ladder polymer networks synthesis through high-energy ball milling. Reproduced with permission from ref. [137].

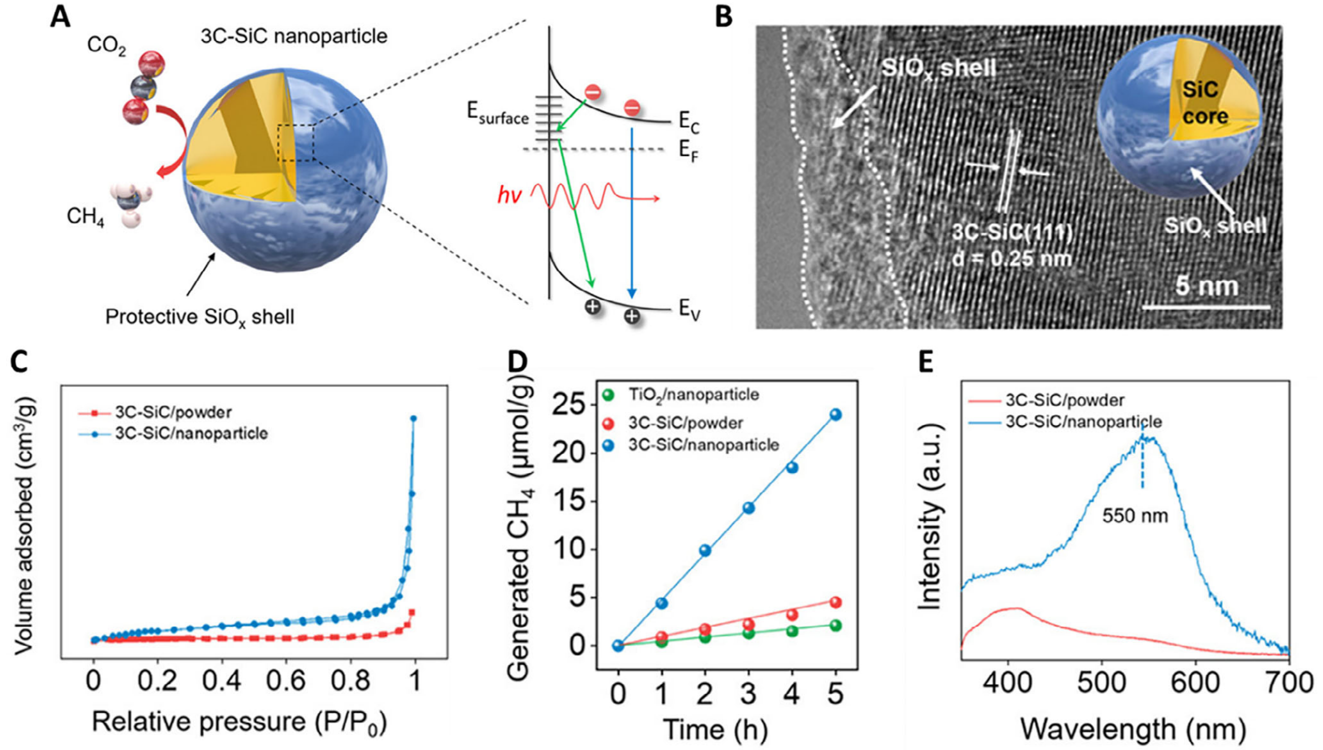

Figure 11. A) Representation of 3C-SiC nanoparticle and its band structure. B) High-resolution TEM image of nanosized 3C-SiC. C) N_2-physisorption analysis of the 3C-SiC crystalline powder and 3C-SiC nanoparticles. D) Photocatalytic CH_4 evolution over the different materials. E) Room-temperature steady-state PL spectra of the different materials. Reproduced with permission from ref. [142].

the ladder-type bent structure of HAT-S, which promoted directional charge transfer from the electron-donating thianthrene to the electron-accepting HATNA units. In contrast, planar structure in HAT-N resulted in less efficient charge separation, as the excited electrons and holes were more delocalized and intertwined, reducing their mobility. To further investigate the charge carrier dynamics, transient photocurrent response, steady-state PL, and TRPL spectroscopy were performed. HAT-S displayed a significantly higher photocurrent density than HAT-N, indicating improved separation of photogenerated electron–hole pairs. In addition, the steady-state PL intensity of HAT-S was notably lower than that of HAT-N, suggesting suppressed recombination of charge carriers. TRPL analysis showed a longer average photocarrier lifetime for HAT-S (32.10 ns) compared to HAT-N (18.53 ns), highlighting enhanced charge mobility.

DFT calculations showed that nitrogen atoms in HAT-S capture excited electrons, while sulphur atoms capture holes, facilitating effective charge separation. EIS measurements revealed that HAT-S exhibited lower charge transfer resistance, enhancing electron mobility, while PL spectroscopy showed a longer average lifetime of photogenerated carriers in HAT-S (32.10 ns) compared to HAT-N (18.53 ns), contributing to prolonged electron availability for CO_2 reduction.

Cubic silicon carbide (3C-SiC) is a metal-free semiconductor characterized by a narrow band gap of 2.36 eV. This feature enables an efficient absorption of visible light and band positions well-suited for CO_2 reduction and water oxidation.[138–141] Hao Li et al. developed a mechanochemical synthesis to produce 3C-SiC nanoparticles with enhanced surface properties that led to improved charge separation and selective photoreduction of CO_2 to CH_4 under visible-light irradiation (**Figure** 11A).[142] A top–down approach was followed by using high-energy ball milling to reduce the particle size and introduce surface defects. Bulk 3C-SiC powder was processed for 5 h at 500 rpm, generating an amorphous silica (SiO_x) layer on the nanoparticle surface. This layer played a pivotal role in preventing photoinduced corrosion, preserving the integrity of Si–C bonds, and ensuring long-term catalytic stability during photoreduction.

The resulting material was comprised of a thin amorphous SiO_x layer that surrounded a crystalline 3C-SiC core (Figure 11). N_2-phisisorption analysis showed that BET surface area increased from 0.39 $m^2\ g^{-1}$ (bulk SiC) to 15.14 $m^2\ g^{-1}$ after ball milling, improving the material's CO_2 adsorption capacity (Figure 11C). Under visible light irradiation, the ball-milled 3C-SiC nanoparticles exhibited a CH_4 production rate of 4.9 $\mu mol\ g^{-1} h^{-1}$, with a selectivity exceeding 90% (Figure 11D). Isotopic labelling experiments using $^{13}CO_2$ confirmed that the carbon source for CH_4 production originated from CO_2, and not from the catalyst decomposition. The enhanced photocatalytic performance of the ball-milled 3C-SiC nanoparticles was primarily attributed to the structural defects introduced during the milling process. These defects acted as electron traps, which captured photogenerated electrons and reduced their recombination with holes. This phenomenon was confirmed through PL spectroscopy, which showed a substantial emission peak at 550 nm (Figure 11E). Moreover, TRPL showed a prolonged lifetime of

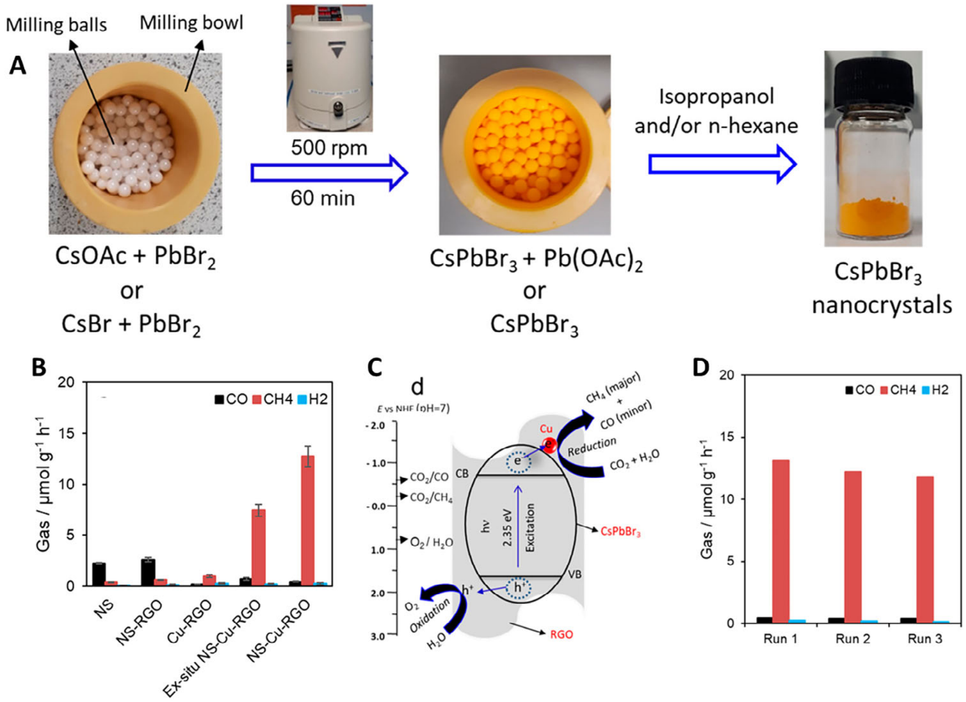

Figure 12. A) Illustration of the Mechanochemical synthesis of $CsPbBr_3$ perovskites. B) CO, CH_4, and H_2 production rates measured on different photocatalysts made of $CsPbBr_3$ and Cu and/or RGO. C) Schematic illustration of the charge separation and transfer mechanism for CO_2 reduction on $CsPbBr_3$-Cu-RGO nanocomposites under simulated solar irradiation. D) Reusability test of NS-Cu-RGO composite. Reproduced with permission from ref. [143].

photogenerated charge carriers, with an average electron lifetime (τ_2) of 38.9 ns, nearly six times longer than that of untreated SiC (6.7 ns).

The reaction mechanism was explored by in situ FTIR spectroscopy, which allowed to identify *COOH as the key intermediate during CO_2 reduction. Then, the subsequent formation of *CHO and *CH_3O species was noticed before the final production of CH_4. This study demonstrated the potential of ball milling to produce high-performance metal-free silicon carbide nanoparticles from cost-effective materials.

3.2.5. Mechanochemically-Prepared Perovskites

The synthesis of lead-based halide perovskites (LHP) nanocrystals via mechanochemical methods allows a precise control over particle size, morphology, and crystallinity. All these features play a crucial role in determining the photocatalytic efficiency of the resulting materials. For instance, Kumar et al. demonstrated that varying ball milling parameters during the synthesis of $CsPbBr_3$ perovskites led to distinct structural and morphological characteristics (**Figure** 12A).[143] In particular: i) by increasing the milling time from 60 to 180 min, the diameter of $CsPbBr_3$ nanorods decreased from 60–70 to 20–40 nm; ii) by prolonging milling beyond 300 min resulted in the formation of nanospheres (40–50 nm) due to the changing energy dynamics; iii) at 500 rpm, by increasing the zirconia ball size from 5 to 15 mm led to the formation of longer nanorods, iv) by switching the cesium precursor from acetate to bromide resulted in nanosheets instead of nanorods, highlighting the influence of precursor chemistry on morphology.[143,144]

The photocatalytic CO_2 reduction activity of the synthesized $CsPbBr_3$ perovskites was evaluated in the gas phase using water vapor as a proton source. Three distinct $CsPbBr_3$ perovskite samples, obtained under varying ball-milling conditions, were tested alongside their composites with Cu-decorated reduced graphene oxide (Cu-RGO), which was synthesized via a solvothermal method. The composite (labelled NS-Cu-RGO) was obtained by adding Cu-RGO in isopropanol suspensions to the previously described $CsPbBr_3$ nanocrystal. Compared to the pristine $CsPbBr_3$ (labelled NS), the incorporation of Cu-RGO significantly enhanced CO_2-to-CH_4 conversion efficiency and selectivity (Figure 12 B,C). Notably, the total electron consumption increased from 8.1 to 103 µmol $h^{-1}g^{-1}$, while the selectivity for CH_4 improved from 42.5% to 98.5%.

Furthermore, composite materials exhibited superior stability in humid conditions. While pristine $CsPbBr_3$ nanosheets lost ≈70% of their photocatalytic activity over three consecutive reaction cycles, their Cu-RGO composites retained nearly 90% of the initial activity (Figure 12D). These nanocomposites also demonstrated an apparent quantum efficiency of 1.10% at 523 nm, attributed to enhanced charge separation, increased visible-light absorption, improved CO_2 adsorption/activation, and a hydrophobic character that mitigates degradation in moisture-rich environments.

However, for a fully green and scalable approach, future research should focus on developing air-stable mechanochemical routes, ensuring greater feasibility for CO_2 photoreduction

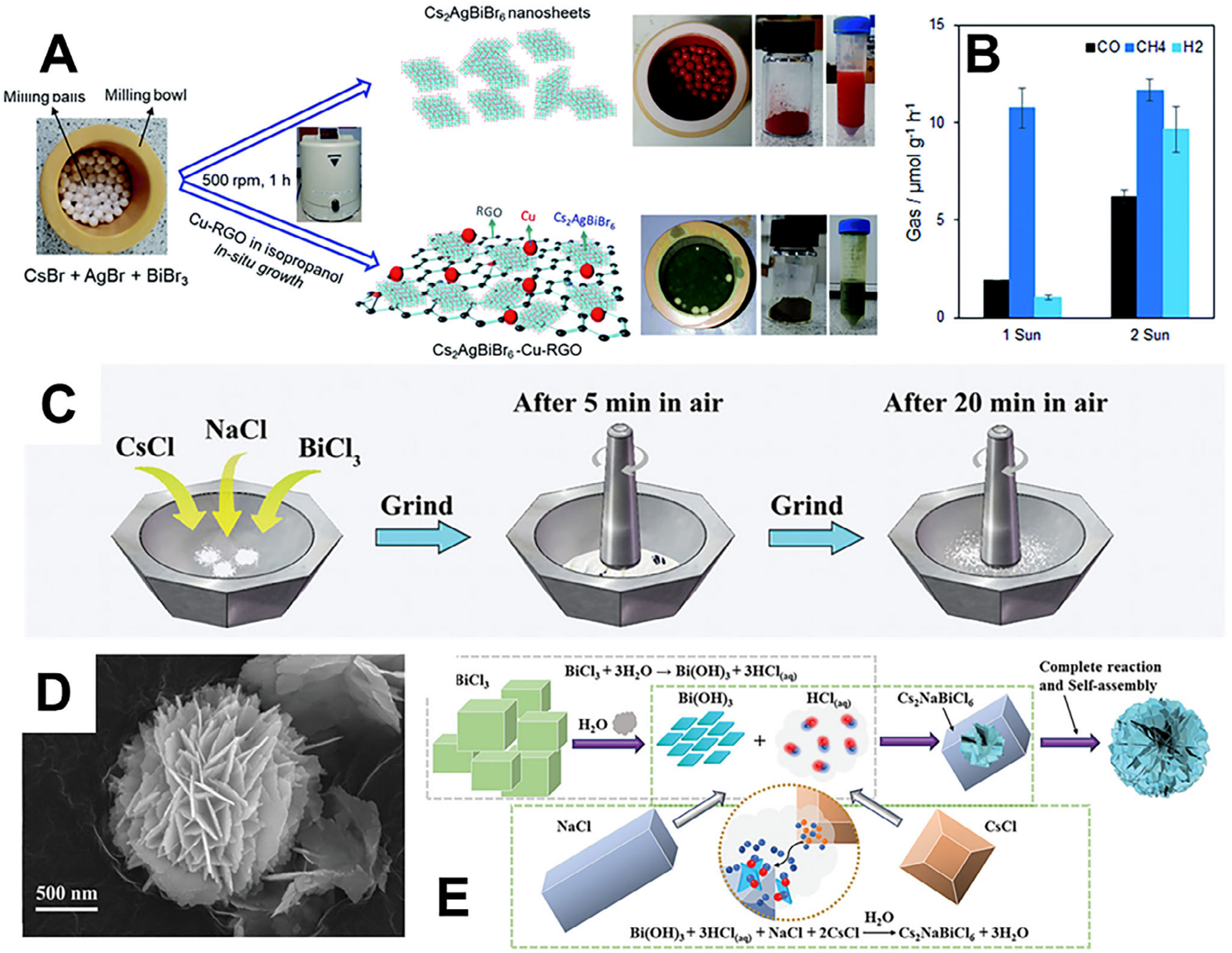

Figure 13. A) Schematic representation of mechanochemical synthesis of $Cs_2AgBiBr_6$ nanoplates and $Cs_2AgBiBr_6$-Cu-RGO composite. B) CO, CH_4, and H_2 production on DP-Cu-RGO with 1 and 2 suns of simulated sunlight. Reproduced with permission from ref. [145]. C) Illustration of the synthesis of $Cs_2NaBiCl_6$ by mechanochemical grinding. D) FE-SEM image of $Cs_2NaBiCl_6$-G. E) Schematic mechanism of $Cs_2NaBiCl_6$ nanoflakes. Reproduced with permission from ref. [146].

technologies. In this context, lead-free halide perovskites (LFHPs) have emerged as an alternative, offering reduced environmental impact and improved chemical stability. Among the various synthesis strategies, mechanochemical synthesis, via ball milling, has gained prominence to produce LFHP nanomaterials with tunable properties.[109]

Kumar et al. reported the mechanochemical synthesis of Pb-free $Cs_2AgBiBr_6$ double perovskite nanoplates and their heterostructures with Cu-loaded reduced graphene oxide (Cu–RGO) for gas-phase photocatalytic CO_2 reduction.[145] The synthesis involved planetary ball milling of $CsBr_3$, $AgBr_3$, and $BiBr_3$ precursors in a 2:1:1 molar ratio, achieving optimal formation of $Cs_2AgBiBr_6$ at 500 rpm for 60 min. To fabricate Cu–RGO or RGO composites, suspensions of Cu–RGO or RGO in isopropanol were added to the precursor mixture before milling (**Figure** 13A). The resulting $Cs_2AgBiBr_6$ nanoplates exhibited high thermal stability, comparable to Pb-based perovskites. At ambient conditions, pristine $Cs_2AgBiBr_6$ (DP) nanoplates remained stable for 2 days, while the Cu–RGO composite maintained its structural integrity beyond 8 days.[145] The steady-state PL intensity of this nanocomposite was significantly reduced compared to pristine DP, indicating suppressed radiative recombination due to improved charge separation at the $Cs_2AgBiBr_6$/Cu–RGO interface. TRPL further confirmed this behavior, with the nanocomposite exhibiting a much shorter average carrier lifetime (0.2 ns) than DP (1.5 ns), suggesting enhanced nonradiative pathways that facilitate charge extraction. These findings were corroborated by photocurrent measurements under light irradiation, where the $Cs_2AgBiBr_6$/Cu–RGO electrode displayed a markedly higher photocurrent response, consistent with more efficient photoinduced charge separation and transport across the heterostructure.

The photocatalytic performance of these mechanochemically synthesized perovskites was evaluated for gas-phase CO_2 reduction using water vapor as a proton source. While $Cs_2AgBiBr_6$ alone was less effective than Pb-based perovskites such as

$CsPbBr_3$, the $Cs_2AgBiBr_6$ -Cu-RGO nanocomposite achieved a CH_4 selectivity of 93.0 ± 0.5%, with an apparent quantum efficiency of 0.89 ± 0.21%. Remarkably, under simulated solar light (1 sun), the composite reached a photocatalytic activity of 93 mmol $h^{-1}g^{-1}$, with a 13-fold enhancement compared to $Cs_2AgBiBr_6$ alone. When the light intensity was doubled to 2 suns, photocatalytic activity increased by an additional 32%, albeit with a slight reduction in CH_4 selectivity due to an increased H_2 production (Figure 13B).

The photocatalytic performance of $Cs_2AgBiBr_6$-Cu-RGO was attributed to the formation of a well-integrated heterointerface, which facilitated charge separation and reduced electron–hole recombination. This occurred through electron transfer from $Cs_2AgBiBr_6$ to Cu via RGO, alongside hole migration toward the perovskite surface or the RGO framework. Additionally, the hydrophobic nature of RGO enhanced the long-term reusability of the photocatalyst, underscoring its potential as a viable Pb-free perovskite material for sustainable solar fuel production.

Nontoxic halide double perovskite materials have many advantages over lead halide perovskite, but they usually exhibit poor stability and very low intrinsic photocatalytic CO_2 reduction activity. Pi et al. developed chlorine-deficient 3D hierarchical $Cs_2NaBiCl_6$ porous microspheres using a controlled solid-state mechanochemical grinding approach.[146] This procedure introduced chlorine vacancies, improved charge carrier separation, and CO_2 activation properties. The synthesis involved manual grinding of solid precursors in an agate mortar for 25 min in air, as shown in Figure 13C. In the first 5 min, the chlorides adsorbed moisture from the atmosphere, forming a viscous mixture. As grinding was prolonged to 20 more minutes, a dry powder comprised of highly crystalline $Cs_2NaBiCl_6$ nanoflakes was obtained (Figure 13D). The mechanism underlying this transformation was attributed to the hydrolysis of $BiCl_3$, which generated $Bi(OH)_3$ nanoflakes while releasing HCl in an aqueous microenvironment. This process facilitated the rapid diffusion of Cs^+, Na^+, and Cl^- ions, enabling their interaction with $Bi(OH)_3$ to form oriented $Cs_2NaBiCl_6$ nanoflakes ($Cs_2NaBiCl_6$-G). The latter subsequently self-assembled into 3D hierarchical microspheres (Figure 13E).

The synthesized $Cs_2NaBiCl_6$ perovskite exhibited outstanding performance in gas–solid CO_2 photoreduction without the use of sacrificial agents, achieving a CO yield of 30.22 μmol g^{-1} h^{-1}. Experimental investigations combined with DFT calculations revealed that chlorine vacancies suppressed electron–hole recombination, improving CO_2 adsorption, and reduced the energy barrier for the formation of the COOH* intermediate, which is critical for CO_2 activation.

Steady-state PL and TRPL analyses were employed to evaluate the radiative recombination and charge carrier dynamics in $Cs_2NaBiCl_6$-based materials. The pristine sample ($Cs_2NaBiCl_6$-H) exhibited stronger PL emission, while chlorine-deficient variants ($Cs_2NaBiCl_6$-A and $Cs_2NaBiCl_6$-G) showed a marked reduction in luminescence intensity, suggesting that the presence of halide vacancies promotes charge separation by trapping excited electrons and reducing radiative recombination. Among them, $Cs_2NaBiCl_6$-G displayed the most significant PL quenching, indicating that its 3D hierarchical morphology further enhances charge carrier separation. TRPL measurements revealed a progressive increase in average carrier lifetime from $Cs_2NaBiCl_6$-H to -A and -G, confirming that both chlorine vacancies and nanostructuring play a synergistic role in extending charge carrier lifetimes and suppressing recombination processes.[146] Finally, compared to pristine $Cs_2NaBiCl_6$, the engineered hierarchical perovskite exhibited a 12.34-fold enhancement in CO_2 photoreduction activity. This behavior was attributed to its increased surface area, higher density of active sites, shorter charge diffusion pathways, and improved charge separation efficiency.

Tin-based halide perovskites have offered another alternative for lead-free optoelectronic applications, particularly in solar cells. However, their intrinsic instability in humid environments has largely hindered their applicability in photocatalytic CO_2 reduction. To address this limitation, Tsai et al. developed mixed-cation pseudohalide tin perovskites using a solvent-free mechanochemical approach.[25] The resulting material displayed enhanced water stability and photocatalytic efficiency. The perovskites were synthesized via ball milling of formamidinium iodide (FAI), tin(II) thiocyanate ($Sn(SCN)_2$), and different amounts of dimethylammonium iodide (DMAI). The synthesis was carried out inside a glove box (<5 ppm O_2), where the precursor mixture was placed into a milling jar along with zirconia balls (Φ = 3 mm). The system was then subjected to mechanochemical grinding at 400 rpm for 1 h at room temperature. Post-milling, the obtained perovskite was dispersed in deionized water, centrifuged for 5 min, and dried in a vacuum oven at 40 °C for 12 h.

Compared to conventional solution-based synthesis, this method enabled both lower processing temperatures and reduced reaction time.[147,148]

Photocatalytic evaluations identified the DMA50 system (where DMA:FA = 1:1, DMA and FA correspond to dimethylammonium and formamidinium cations, respectively) as the most efficient sample, achieving a CO production yield of 285 μmol g^{-1} after 12 h of light irradiation in a humid environment, surpassing other tin-based perovskites with different DMA-to-FA ratios. Stability assessments, including 24 h water immersion tests, demonstrated that $DMA_{0.5}FA_{0.5}$ preserved its structural integrity and electronic properties, exhibiting minimal oxidation of Sn^{2+} to Sn^{4+}. The steric hindrance of the methyl groups and the centrally located positive charge on the carbon atom in DMA acted as a protective barrier against hydrolysis by water. This study represents the first successful application of pseudohalide tin perovskites in photocatalytic systems, addressing the challenge of catalyst instability under humid conditions.

3.2.6. Mechanochemically-Prepared MOFs

MOFs have gained significant attention as potential photocatalysts for CO_2 reduction, owing to their high surface area, tunable porosity, and adaptable electronic properties.[149] The transport of photogenerated charge in MOFs photocatalyst systems can occur via three possible modes: i)Hopping conduction: electron transfer occurs between donor and acceptor sites via discrete energy levels, ii) Through-bond conduction: charge carriers travel through coordination or covalent bonds, influenced by metal d-orbital coupling with organic linkers, iii) Through-space charge transport: electrons migrate between donor and acceptor sites via non-covalent interactions (e.g., π–π stacking).[150]

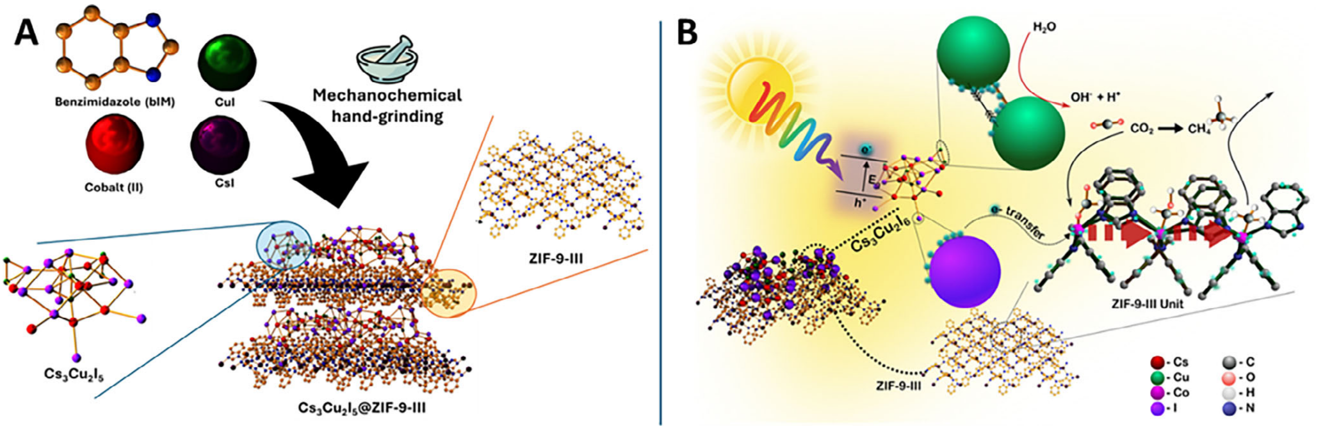

Figure 14. A) Schematic illustration of $Cs_3Cu_2I_5$@ZIF-9-III mechanochemical synthesis. B) Schematic representation of CO_2 photoreduction at the $Cs_3Cu_2I_5$@ZIF-9-III interface. Reproduced with permission from ref. [158].

However, conventional solution-based synthesis methods often suffer from low material yield, poor structural stability, and inefficient charge carrier separation, which significantly limit their overall photocatalytic performance.[151–154] To overcome these challenges, mechanochemical synthesis has emerged as a scalable, solvent-free strategy that enables the precise engineering of MOFs structures.[152,155]

Recent advancements have demonstrated that mechanochemically synthesized MOFs exhibit greater chemical stability, enhanced charge transport, and improved catalytic activity, particularly when combined with complementary materials such as perovskites, metal oxides, and conductive carbon-based supports.[156,157] These hybrid systems leverage synergistic charge transfer mechanisms, further boosting photocatalytic efficiency and selectivity in CO_2 reduction pathways.

For example, Sharma et al. developed a hybrid photocatalyst consisting of lead-free halide perovskite $Cs_3Cu_2I_5$ nanocrystals integrated with 2D cobalt-based metal–organic framework ZIF-9-III nanosheets, aiming to enhance CO_2 photoreduction efficiency and selectivity.[158,159] The hybrid material, $Cs_3Cu_2I_5$@ZIF-9-III, was synthesized using a mechanochemical one-pot grinding approach, ensuring a strong interfacial interaction between the perovskite and the MOF. The synthesis process involved hand-grinding the perovskite precursors (CsI and CuI) with the MOF precursors ($Co(NO_3)_2{\cdot}6H_2O$ and $NaHCO_3$) in the presence of 2 mL of ethanol for 5 min (**Figure** 14A). The resulting powder was then subjected to successive washing steps with water and methanol to remove unreacted residues. PL, photoluminescence excitation (PLE), and TRPL analyses were carried out to investigate the optical behavior and charge dynamics of $Cs_3Cu_2I_5$ and its composites with Co-ZIF-9(III). The pristine $Cs_3Cu_2I_5$ exhibited intense blue PL emission ≈445 nm and a high photoluminescence quantum yield (PLQY) of ≈90%, consistent with its strong excitonic confinement. However, upon hybridization with Co-ZIF-9(III), a quenching of PL intensity was observed, with PLQY values dropping to 1.5–3.0%, suggesting efficient photoinduced electron transfer from $Cs_3Cu_2I_5$ to the MOF component. TRPL measurements further supported this behavior: the exciton lifetime decreased from 1.43 ms in pure $Cs_3Cu_2I_5$ to 1.04 ms in the hybrid, with a more pronounced decay observed in the early stages of the TRPL curve. This indicates that the interfacial electron transfer primarily occurs on a sub-nanosecond timescale.

Electronic structure analysis by DFT revealed that ZIF-9-III exhibits conduction band (CB) and valence band (VB) positions more negative than those of $Cs_3Cu_2I_5$, leading to the formation of a Type-II heterojunction. Therefore, under simulated solar irradiation electrons from the valence bands (VBs) of both $Cs_3Cu_2I_5$ and ZIF-9-III are excited to their respective conduction bands (CBs), generating electron–hole pairs; after that, the higher CB energy of $Cs_3Cu_2I_5$ enables photoexcited electrons to transfer to the CB of ZIF-9-III where they drive the CO_2 reduction reaction and, simultaneously, holes from the VB of ZIF-9-III migrate to the VB of $Cs_3Cu_2I_5$, where they interact with water molecules, producing O_2 (Figure 14B). In this way, $Cs_3Cu_2I_5$@ZIF-1 exhibited a highly selective and efficient conversion of CO_2 into carbon monoxide (CO) with a production rate of 110 μmol g^{-1} h^{-1} and methane (CH_4), with a production rate of 5 μmol g^{-1} h^{-1}, suppressing hydrogen evolution. DFT calculations confirmed that the non-covalent interactions between $Cs_3Cu_2I_5$ and ZIF-9-III facilitated efficient charge transfer, effectively lowering the energy barrier for CO_2 reduction and enhancing CH_4 selectivity over competing H_2 evolution. This charge redistribution mechanism ensures a more efficient CO_2 conversion process, making the $Cs_3Cu_2I_5$@ZIF-9-III hybrid a promising photocatalyst for solar-driven carbon capture and utilization technologies.

Similarly, Zhao et al. demonstrated that the incorporation of organic guest molecules, such as 9,10-bis(4-pyridyl)anthracene (BPAN), into MOFs significantly improves charge carrier mobility and enhances photocatalytic performance, leading to CO_2 reduction rates exceeding those of conventional MOFs.[156] However, since the synthesis was carried out using a traditional solvothermal approach rather than a more sustainable mechanochemical method, this study will not be examined herein in detail.

3.2.7. Mechanochemically-Prepared Bioconjugates

Recent advances have demonstrated the potential of mechanochemistry for the preparation of bioconjugates, such

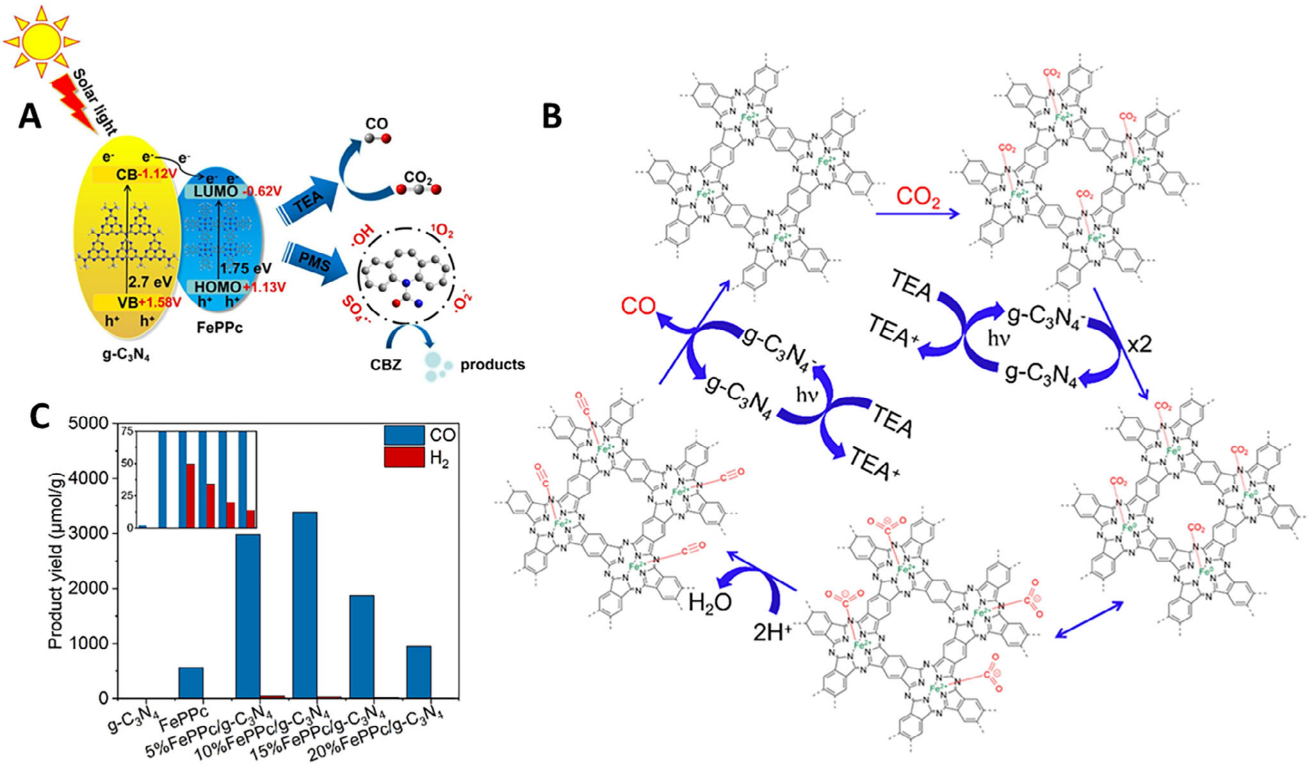

Figure 15. A) Schematic illustration of CO_2 photoreduction and carbamazepine photodegradation. B) Proposed mechanism of CO_2 photoreduction at FePPc/g-C_3N_4 interface. C) CO and H_2 yield after 12 h with different ratios of FePPc/g-C_3N_4; the inset shows a magnified image of the indistinct data in the graph. Reproduced with permission from ref. [165].

as hybrids based on g-C_3N_4 and biomolecules, designed as photocatalysts for CO_2 reduction, enabling the integration of light-harvesting inorganic components with biomolecules under mild, solvent-free conditions. g-C_3N_4 possesses a suitable band gap and a highly stable conjugated structure due to the strong covalent bonding between carbon and nitrogen atoms. These properties make it a promising candidate for photocatalytic applications, including hydrogen generation.[160] However, its limited visible-light absorption and high electron–hole recombination rate significantly restrict its photocatalytic efficiency.[161] To overcome these limitations, strategies such as sensitization with dyes have been explored to extend light absorption into the visible and near-infrared regions. Metal phthalocyanines (MPc) are particularly effective as sensitizers, as they not only enhance light absorption but also promote charge transfer through the formation of heterojunctions.[162,163] However, small-molecule MPc compounds tend to aggregate during catalysis, reducing their efficiency. To address this issue, polymerized metal phthalocyanines (MPPc) have been employed due to their extended π-conjugation, increased metal active sites, and improved catalytic stability. Combining the broad light-harvesting capability of g-C_3N_4 with the catalytic activity of MPPc presents a promising approach to developing high-performance composite photocatalysts.[164]

Chengyu Chu et al. proposed a mechanochemical approach to synthesize a composite photocatalyst based on polymerized iron phthalocyanine (FePPc) and g-C_3N_4, exhibiting outstanding performance in visible-light-driven oxidation of organic pollutants (e.g., carbamazepine) and CO_2 photoreduction to CO (**Figure** 15A).[165] The synthesis involved ball milling FePPc and g-C_3N_4 (both previously prepared via thermal methods)[166,167] at 400 rpm for 1 h, varying the FePPc content. Interestingly, during milling FePPc underwent mechanical exfoliation, leading to strong π–π stacking interactions with g-C_3N_4, ensuring uniform dispersion and improved interfacial contact. The integration of FePPc with g-C_3N_4 resulted in the formation of a well-matched heterojunction, facilitating efficient electron transfer upon light excitation. EIS confirmed this enhancement, revealing improved electronic conductivity. The interaction between FePPc and g-C_3N_4 introduced electronic transition states, allowing excited electrons from the conduction band (CB) of g-C_3N_4 to migrate to the CB of FePPc, thereby reducing charge recombination with holes in the valence band (VB) of g-C_3N_4 and enhancing charge separation (Figure 15B). This effect was further validated by PL spectroscopy, which showed a decrease in emission intensity at 380 nm in the composite relative to pure g-C_3N_4, indicating lower recombination rates. Moreover, the aromatic structure of FePPc played a key role in stabilizing charge carriers, promoting electron storage and improving reactivity for CO_2 reduction. Transient absorption spectroscopy (TAS) analysis demonstrated prolonged electron retention in FePPc, leading to a higher probability of electron participation in CO_2 reduction reactions. Additionally, FePPc broadened the visible light absorption range, extending it into the NIR region, further enhancing photocatalytic efficiency.

As a result, the FePPc/g-C_3N_4 composite with 10% FePPc loading achieved a maximum CO yield of 3388.98 µmol g^{-1} in 12 h under simulated solar irradiation (in water and acetonitrile as solvents and triethylamine as sacrificial agent), significantly outperforming pristine g-C_3N_4. (Figure 15C). In contrast, a similar composite synthesized using small-molecule FePc instead of FePPc exhibited a much lower CO yield of only 175.59 µmol g^{-1}, likely due to FePc's tendency to aggregate, which limited the number of exposed active sites and reduced photocatalytic efficiency. These findings highlight the importance of FePPc's polymeric structure, which ensures better dispersion, charge transfer, and active site availability, particularly when processed via mechanochemical ball milling.

The mechanochemical synthesis employed in this work offers a solvent-free, scalable alternative to conventional methods. However, further optimization of the FePPc synthesis process is necessary, as its preparation remains time-consuming (≈24 h) and requires multiple solvent-based steps. Additionally, exploring different ball milling parameters could provide valuable insights into how processing conditions influence the composite's structural properties and photocatalytic performance, potentially further enhancing its efficiency.

DFT studies have provided critical mechanistic insight into CO_2 photoreduction systems, particularly those involving SACs. DFT calculations revealed that isolated metal atoms such as Ni on g-C_3N_4 or Pd on TiO_2 significantly distort the CO_2 molecule upon adsorption, reducing the O—C—O bond angle and elongating the C—O bonds, thereby lowering the activation barrier for C═O bond cleavage.[124] This activation effect was much weaker on pristine substrates or nanoparticle-based systems. Reaction pathway analyses further demonstrated that SACs not only reduce Gibbs free energies along the reaction coordinate but also alter the rate-determining step and selectivity. For example, Pd_{SA}/TiO_2 showed a much lower energy barrier for ·CHOH reduction than pristine TiO_2, while Zn—CN favored selective CO production due to low CO desorption energy, in contrast to Cu—CN, which promoted CH_4 evolution.[114] DFT-based electronic structure analysis (e.g., PDOS) indicated that metal–nitrogen orbital hybridization enhances charge transfer and suppresses recombination.[131] Furthermore, calculations of work function alignment in van der Waals heterostructures (e.g., CPDs/KCNNS) confirmed the formation of interfacial electric fields that facilitate directional electron migration and efficient carrier separation.[136]

In the case of MOFs, DFT simulations have played a pivotal role in elucidating structure–activity relationships and electronic properties relevant to CO_2 photoreduction. Specifically, defect engineering in MOFs such as UiO-66-NH_2 was shown to lower activation barriers for CO_2 reduction pathways, enhancing photocatalytic efficiency.[152] DFT calculations also enabled predictions of band gap tunability across isoreticular MOFs and revealed that electronic conductivity is strongly influenced by metal-linker orbital coupling and charge carrier effective masses. In hybrid systems, such as halide perovskites interfaced with ZIF-9(III) nanosheets, DFT identified favorable non-covalent interactions and the formation of type-II heterojunctions, facilitating interfacial electron transfer and improving charge separation.[158] Simulations further mapped the reaction energy landscape for CO_2-to-CO and CH_4 conversion, confirming that intermediate species like COOH* preferentially adsorb on active metal sites (e.g., Co) and that guest molecule inclusion within MOF cavities (e.g., BPAN) can significantly reduce rate-limiting barriers.[156] Additionally, the formation of multilevel charge transport pathways, through-space and hopping mechanisms, was shown to extend carrier lifetimes and enhance overall photocatalytic performance.

For halide perovskite-based systems, DFT calculations have similarly deepened the understanding of charge dynamics and CO_2 activation mechanisms. In $Cs_2NaBiCl_6$, chlorine vacancies were found to play a critical role by suppressing charge recombination, enhancing CO_2 adsorption, and lowering the Gibbs free energy for key intermediates such as COOH*, thus significantly improving catalytic performance.[146] These defect states create localized energy levels within the bandgap, primarily due to hybridization between Bi 6*p* and Cl 3*p* orbitals, resulting in stronger light absorption and enhanced charge carrier generation. DFT simulations provided crucial insights into excited-state charge dynamics in donor–acceptor polymers. In HAT-N, excited electrons and holes were spatially overlapping, indicating inefficient charge separation. Conversely, HAT-S exhibited directional charge transfer from the thianthrene donor to the HAT acceptor, with well-separated electron–hole distributions. This behavior explains the superior CO_2 photoreduction efficiency of HAT-S, as confirmed by both theoretical and experimental results.[137]

The studies on CO_2 photoreduction described here are summarized in **Table 2**, highlighting the material type, mechanochemical processes involved, as well as the photocatalytic activity and selectivity.

3.3. Mechanochemistry-Driven Design of Visible-Light-Active Photocatalytic Materials with Potential in Fuel Generation

In addition to studies where materials have been specifically designed for fuel production or the generation of energy vectors such as hydrogen, the literature also reports novel materials synthesized via mechanochemistry that exhibit promising photocatalytic activity or possess optical and structural properties suitable for solar-driven reactions. Although these works are not directly focused on fuel generation, the features of the materials are well aligned with the demands of such processes. Accordingly, this section focuses on the properties of the mechanochemically prepared materials described in these studies and discusses their potential applicability in energy-related catalytic reactions.

Most relevant contributions report the development of systems based on oxides, or containing oxides as the main component, although materials based on graphitic carbon nitride and perovskites are also relevant in the number of publications. There are other complex structures synthesized by mechanochemical methods. Sun et al. developed $ZnIn_2S_4$/Zn-Al layered double hydroxide (LDH) and $CdIn_2S_4$/Zn-Al LDH composites with Z-scheme heterojunctions, demonstrating enhanced visible-light photocatalytic performance for sodium isopropyl xanthate degradation.[168] The composites described superior degradation rates compared to their individual components, with $^{\bullet}O^{2-}$ radicals playing a dominant role. Xiao et al. investigated ball-milled biochar for enrofloxacin degradation, finding that ball-milling promoted reactive oxygen species (ROS) generation and increased photocatalytic activity,[169] while Jiang et al. synthesized BiOBr ultrathin nanosheets using an ionic liquid-assisted

Table 2. Summary of mechanochemically prepared materials and their applications in CO_2 photoreduction.

Entry	Material	Milling condition (speed/time)	Apparent quantum efficiency [%]	Main Photoreduction products and yield [name, $\mu molg^{-1}h^{-1}$]	Refs.
1	Ni/CN-0.5	400 rpm/12 h	nr	CO, 19.9	[124]
2	Zn-CN-0.5; Cu-CN-0.5	400–500 rpm/10–12 h	nr	CO, 21.1; CO,15.2	[131]
3	CPDs/KCNNS	1200 rpm/0.5 h and 1200 rpm/2 h	0.86	CO, 78.9	[136]
4	$PdSA/TiO_2$	400 rpm/12 h	nr	CH_4, 271.6	[114]
5	α-Ga_2O_3/β-Ga_2O_3	400 rpm/up to 16 h	nr	CO, 0.6	[118]
6	HAT-S	30 Hz/2 h	1.11	CO, 306.1	[137]
7	3C-SiC nanoparticles	500 rpm/5 h	nr	CH_4, 4.9	[142]
8	NS-Cu-RGO	500 rpm/1–3 h	1.26	CH_4, 103.0	[143]
9	$Cs_2AgBiBr_6$-Cu-RGO	500 rpm/1 h	1.1	CH_4, 10.7	[145]
10	$Cs_2NaBiCl_6$-G	Manual/10 min	nr	CO, 30.2	[146]
11	DMA50	400 rpm/1 h	nr	CO, 23.8	[25]
12	$Cs_3Cu_2I_5$@ZIF-9-III	Manual/ 5 min	nr	CO, 110.0	[158]
13	FePPc/g-C_3N_4	400 rpm/1 h	nr	CO, 282.4	[165]

[a] nr: non-reported.

mechanochemical method, achieving superior visible-light-driven photocatalysis for bisphenol.[170]

Among the most notable examples of oxide-based systems are the studies that have demonstrated the synthesis of ultrafine PVP-BiO_2-x nanomaterials, TiO_2-based photocatalysts, and $CuBi_2O_4$/Zn-Al LDH p-n junction hybrids, all of which exhibit enhanced visible light absorption and photocatalytic performance.[57,171,172] Mechanochemical processes have also been used to create Z-scheme Bi_2MoO_6/Zn-Al LDH heterojunctions, reduce metal oxides like TiO_2 and Nb_2O_5 and prepare sulfur-doped nanosized TiO_2.[173–175] These methods have resulted in materials with enhanced visible light absorption, improved charge separation, and increased photocatalytic activity for degrading organic pollutants. Additionally, the effect of calcination temperature on Fe_2O_3-ZrO_2 nanocomposites has been investigated for photocatalytic applications.[176] These studies highlight the potential of mechanochemical approaches in developing efficient visible-light-driven photocatalysts. A solventless mechanochemical approach produced Pd/H_xMoO_3 nanoparticles with enhanced catalytic activity due to synergistic optical excitations.[177] In this contribution, the authors address the limitations of plasmonic photocatalysis, which has traditionally been constrained by the high cost and scalability issues of materials like Ag and Au. The effects of Pd interband transitions irradiated at 427 nm, and H_xMoO_3 localized surface plasmon resonance (LSPR) generated using a wavelength of 640 nm, were investigated. Both excitation wavelengths led to comparable photoenhancements, but a 110% increase in activity was achieved under dual excitation conditions (427 and 640 nm). **Figure** 16 schematically shows the synthesis procedure of the catalysts obtained by mechanochemistry. The proposed procedure was relatively simple, based on the chemical reduction of the noble metal precursor with $NaBH_4$. In this step, both the deposition of palladium nanoparticles and the exfoliation of the MoO_3 structure, advantageous in morphological and structural terms, were carried out. Additionally, according to the authors' description, some H intercalation is obtained. The plasmonic properties were achieved using an H_2 treatment that consisted of bubbling H_2 in a solution containing the solid obtained by mechanochemistry, forming the Pd/H_xMoO_3 structure. The intercalation of H_2 atoms increases the free charge carriers with high delocalization, generating localized surface plasmon resonance. Since H_xMoO_3 also has semiconductor properties, the authors propose a scheme where a synergistic effect occurs between photocatalytic excitations and plasmonic catalysis. The charge management mechanism in the structure is complex but can be schematically represented as shown in Figure 16B–E. Under irradiation conditions at 427 nm (Figure 16B), the system acted following a typical semiconductor scheme, leading to the formation of active charges. At the same time, band transitions in Pd (Figure 16C) also generate energetic electrons. These electrons from H_xMoO_3 and Pd can be transferred to Pd sites, which, according to the authors' description, enhance catalysis by activating adsorbed molecules (phenylacetylene or H species). When the material received radiation at a longer wavelength (640 nm), plasmonic excitation was activated (hot electrons). This is schematically represented in Figure 16D. Under these excitation conditions, these electrons were transferred to the noble metal particles, increasing catalytic activity. The combined effect at both wavelengths is described in Figure 16E. Under these conditions, both processes occur simultaneously, where efficient charge management produces an effect that significantly improves the results using only one type of radiation. The synergistic effect that can be generated by using this type of material opens up the possibility of harnessing solar radiation and multi-energy excitations.

Other notable examples include $WO_3 \bullet 2H_2O$ ultrathin nanosheets, synthesized via a one-step, solvent-free mechanochemical reaction, exhibiting excellent photocatalytic properties;[178] a Z-scheme $Bi_2WO_6/CuBi_2O_4$ heterojunction, prepared through mechanochemical synthesis, showing high

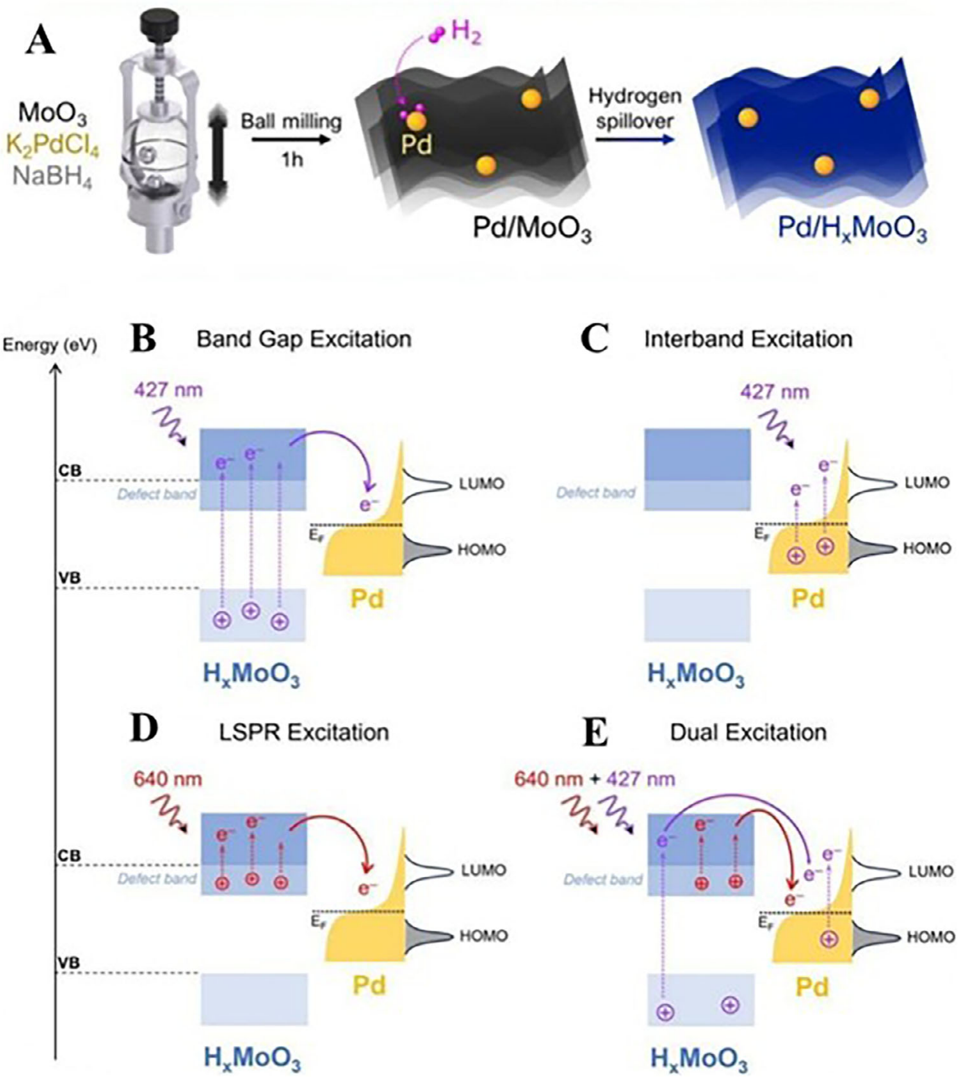

Figure 16. A) Schematic description of the mechanochemistry preparation of Pd/H_xMoO_3. A mechanism proposed using the Pd/H_xMoO_3 sample. B) H_xMoO_3, 427 nm; C) Pd interband transitions at 427 nm; D) H_xMoO_3 LSPR excitation at 640 nm, and E) scheme under dual illumination conditions. Modified with permission from ref. [177].

efficiency in ciprofloxacin degradation under visible light;[179] and Fe-doped ZnO nanoparticles, synthesized using high-energy ball milling, demonstrating enhanced photocatalytic-related performance for the degradation of malachite green and phenol under visible light and ultrasonic waves.[180] These synthesis strategies, which involve the development of oxide-based systems and, in some cases, the incorporation of co-catalysts (mainly noble metals), are transferable to energy-relevant reactions such as hydrogen production via reforming (e.g., of alcohols or methane) or CO_2 hydrogenation to methane or methanol.[181,182]

As previously discussed, and well-described in the literature, $g\text{-}C_3N_4$-based materials are highly promising candidates for the energy-related reactions addressed in this work.[183,184] Their exceptional synthetic simplicity, particularly well-suited to mechanochemical approaches, has further stimulated interest in their development and application. Deng et al. employed mechanical ball milling to fabricate amorphous $TiO_2/g\text{-}C_3N_4$ heterojunctions with improved interfacial bonding and charge carrier separation,[185] while Liu et al. developed a one-step mechanochemical treatment to produce anthraquinone-coupled few-layered $g\text{-}C_3N_4$ nanoplates, achieving 14 times better photocatalytic H_2O_2 production compared to bulk materials.[186] In another contribution, the authors used ball milling to increase single-atom cobalt-hydroxyl loading on polymeric carbon nitride, resulting in significantly enhanced oxygen evolution reaction rates.[187] The last-mentioned manuscript presents an advancement in photocatalytic water oxidation by synthesizing single-atom Co-OH modified polymeric carbon nitride (Co-PCN) with a 37-fold increase in single-atom content using ball milling.[187] This modification enhanced the photocatalytic oxygen evolution reaction (OER) activity under visible light irradiation compared to common PCN/CoO_x and control samples prepared without ball milling. The single-atom $Co\text{-}N_4OH$ structure in Co-PCN, confirmed both experimentally and theoretically, enhances optical

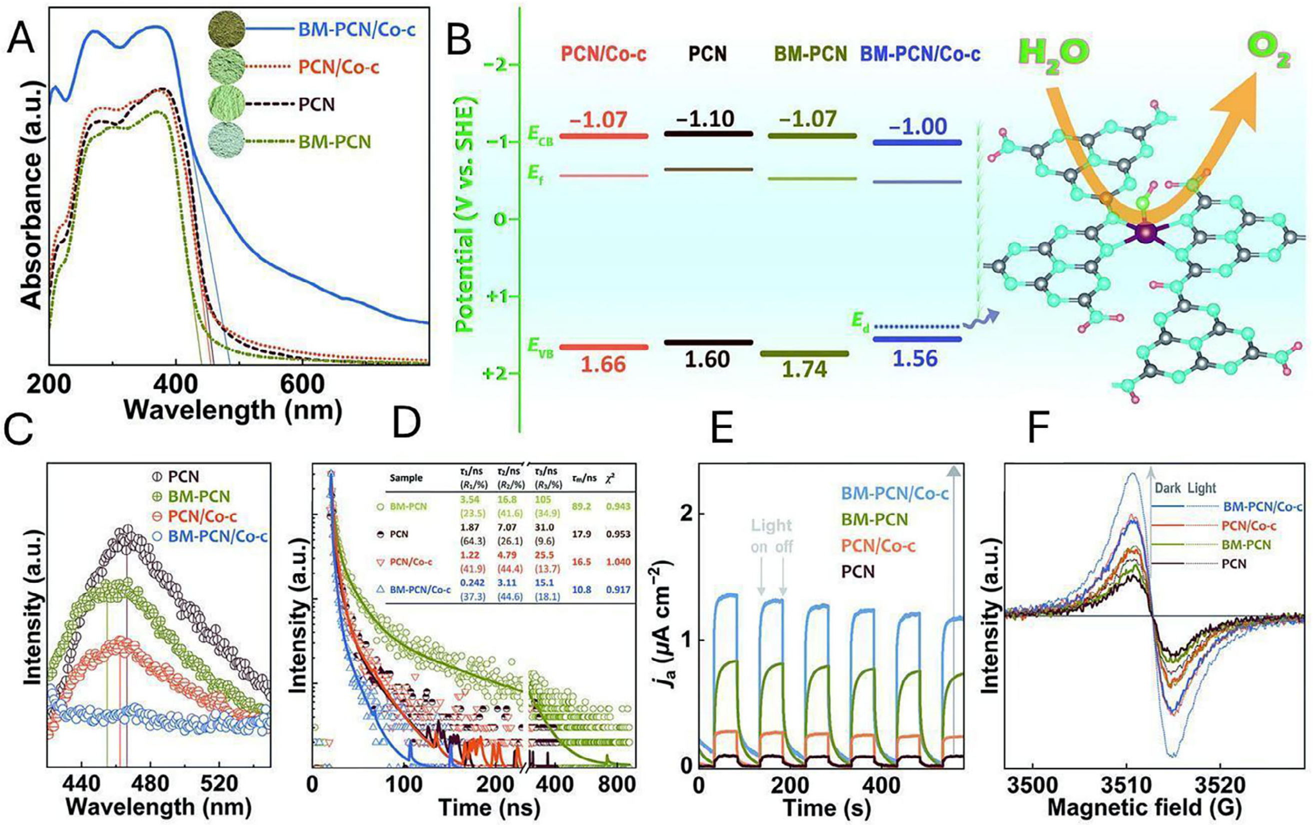

Figure 17. A) UV–vis data obtained for PCN, BM-PCN, BM-PCN/Co-c, and PCN/Co-c samples. B) Energy band levels of the samples and schematic description of the tested reaction. C) Photoluminescence data. D) Time-resolved fluorescence data. E) Anodic photocurrent response and F) EPR spectra. Reproduced with permission from ref. [187].

absorption, charge separation, and serves as the active site for OER. Co-PCN exhibited the highest OER rate of 37.3 μmol h^{-1} under visible light, which was 28 times higher than common PCN/CoO$_x$. The methodology involved ball milling PCN to obtain BM-PCN with reduced particle size and increased surface energy, adsorption of Co^{2+} ions onto BM-PCN, followed by calcination to form Co-PCN. A good summary of the characterization studies to evaluate relevant properties in terms of absorption and charge mobility is presented in **Figure** 17A–F. BM-PCN/Co-c showed significantly higher optical absorption compared to PCN, attributed to electron-rich Co and Co─OH doping (Figure 17A). Bandgaps were determined, revealing differences due to quantum size effects and doping. As described in Figure 17C–E, photoluminescence and photoelectrochemical tests indicated that BM-PCN/Co-c has the highest photogenerated charge separation efficiency, while Electron paramagnetic resonance spectroscopy demonstrated that Co doping increases delocalized electron density, enhancing charge transport and photocatalytic activity (Figure 17F). In particular, Time-resolved fluorescence spectra (Figure 17D) indicated that while ball-milled PCN (BM-PCN) showed significantly longer lifetimes (89.2 vs 17.9 ns for pristine PCN), suggesting faster charge transfer from the bulk to the surface and reduced recombination, the cobalt-modified samples (PCN/Co-c and especially BM-PCN/Co-c) exhibited much shorter lifetimes (16.5 and 10.8 ns, respectively). This shortening is attributed to the efficient capture of photogenerated holes by the Co-OH doping levels, leading to rapid non-radiative energy transformation, essentially consuming the charges for the reaction rather than wasteful recombination. Consistently, the photoluminescence (PL) intensity was lowest for BM-PCN/Co-c, indicating the highest charge separation efficiency (Figure 17C). Furthermore, the anodic photocurrent density followed the order PCN < PCN/Co-c < BM-PCN < BM-PCN/Co-c, directly confirming its superior charge separation and transfer performance of BM-PCN/Co-c, due to both ball milling and Co-OH modification.

Recent studies have explored solvent-free, mechanochemical extrusion methods for synthesizing graphitic carbon nitride photocatalysts decorated with carbon dots (CDs). This mechanochemical approach, in contrast to traditional high-temperature and high-pressure synthesis methods, has been shown to significantly influence the materials' optical properties by increasing defects, modifying the bandgap, and altering charge dynamics. These changes were found to enhance the photocatalytic performance of the composites, offering a more environmentally friendly and energetically favorable alternative for photocatalytic applications.[188]

Recent research has explored innovative approaches to synthesizing and applying covalent organic frameworks (COFs) and metal-organic frameworks (MOFs) for catalytic purposes. Lv et al. demonstrated a ball milling technique to produce COFs at room temperature, significantly reducing synthesis time and

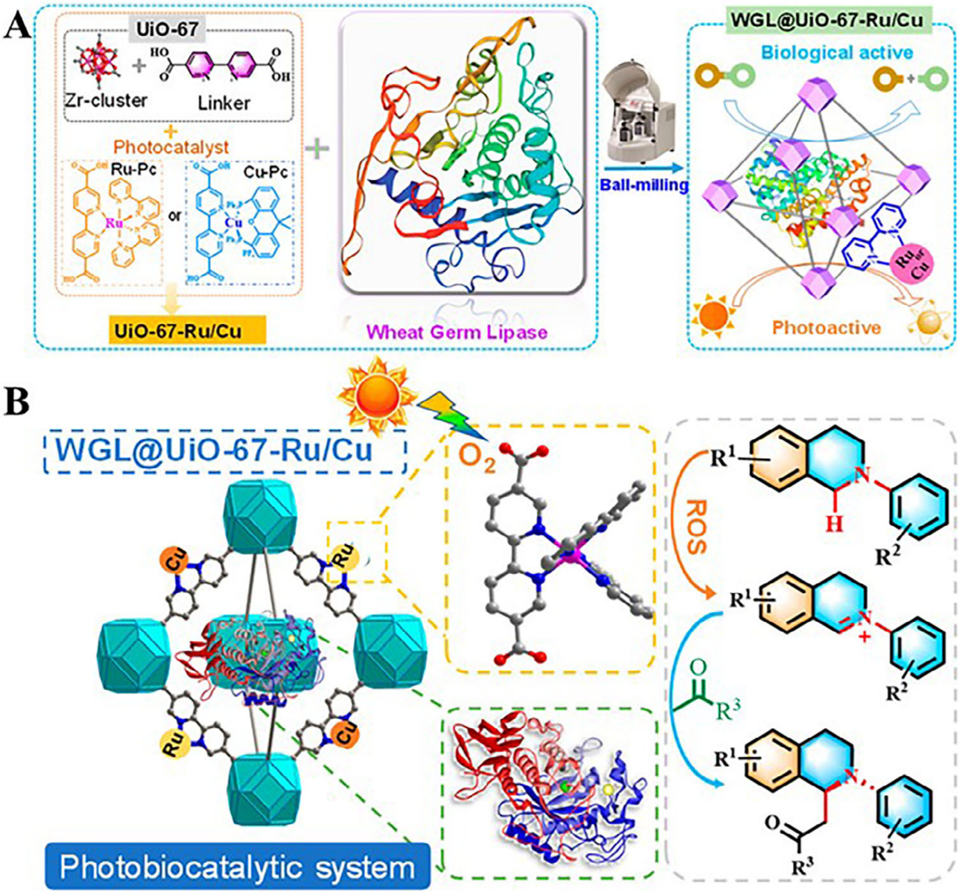

Figure 18. A) Schematic description of integrated photoenzyme System preparation. B) Diagram of N-aryl-substituted tetrahydroisoquinoline asymmetric catalysis. Modified with permission from ref. [190].

solvent use compared to traditional methods.[189] The resulting COFs showed promising photocatalytic activity for degrading organic pollutants. As described in **Figure** 18A, an effective mechanochemical method to encapsulate both photocatalysts and enzymes within Zr-based MOFs, creating heterogeneous photoenzymatic catalysts was employed. The catalytic system exhibited high activity and stability in asymmetric Mannich reactions, with a broad substrate scope. The integration of multiple catalytic components within functional immobilization systems, such as MOFs, emerged as a promising strategy for developing photo biocatalysts with enhanced performance and reusability.[190] This study represents a significant advancement in the integration of photocatalysis and biocatalysis within a heterogeneous system for enantioselective catalysis. The mechanochemical synthesis strategy employed to simultaneously encapsulate a photocatalyst and wheat germ lipase (WGL) into a Zr-based MOF proved to be highly effective. The resulting photo biocatalysts not only exhibit high catalytic activity and operational stability but also expand the substrate scope to include N-aryl-substituted tetrahydroisoquinolines, which had not been previously achieved through photocatalysis. The optimization of the photosensitizer loading ratios, specifically the 1/2 and 1/3 ratios of photosensitizers to 2,2′-Bipyridine-5,5′-dicarboxylic acid ligand, resulted in the best crystallinity and performance. Detailed characterization techniques, including transient photocurrent response curves and 3D view confocal laser scanning microscopy images, confirmed the successful incorporation of both the photocatalyst and enzyme. The study also revealed that the MOF shells effectively protect the encapsulated WGL from external disturbances such as organic solvents, hot water, and heat treatment, thereby enhancing the enzyme's stability and reusability. As described in Figure 18B, the catalytic mechanism was thoroughly investigated, with electron spin resonance (ESR) and reactive oxygen species probes identifying superoxide anions and singlet oxygen as the primary active species driving the asymmetric catalysis. This work not only provides a robust platform for enantioselective catalysis but also opens new possibilities for industrial applications, highlighting the synergy between chemistry and biosynthesis. The ability to achieve high enantioselectivity (er values up to 85:15) and maintain catalytic activity after multiple recycling (up to 88% after ten cycles) underscores the practical potential of these photocatalysts.

Perovskites are also noteworthy materials that have been employed in visible-light-driven photocatalytic reactions, yielding promising results, and have demonstrated performance worth considering in reaction schemes aimed at energy applications.[191,192] Although many studies only achieve an optical characterization of the materials, the simple tuning of

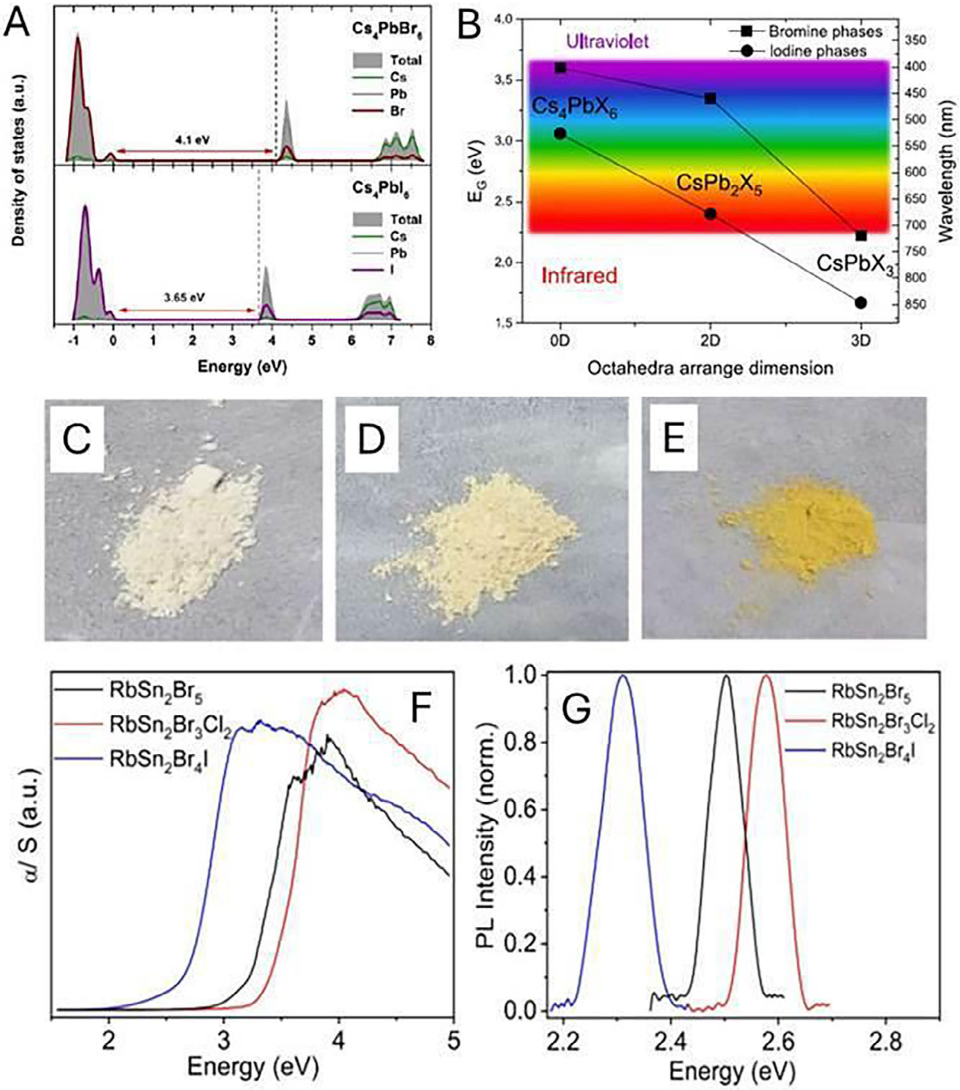

Figure 19. A) Partial density of states for Cs_4PbX_6 (X = Br, I) halides. B) Comparison of the band gap energy values for the Cs–Pb–X (X = Br, I) phases with different octahedral arrangement dimensions. Reproduced with permission from ref. [193]. Prepared samples C) $RbSn_2Br_3Cl_2$, D) $RbSn_2Br_5$, and E) $RbSn_2Br_4I$, F) UV–Vis and G) PL spectra for $RbSn_2Br_3Cl_2$, $RbSn_2Br_5$, and $RbSn_2Br_4I$ samples. Modified with permission from ref. [197].

their optical and electronic properties, which define their photocatalytic activity, makes them strong candidates for potential use in fuel production under solar radiation. Studies related to the preparation of $Cs_4PbBr_{6-x}I_x$, $CsSn_2Br_5$, $Cs_2AgBiBr_6$, $Cs_3Bi_2Br_9$, $Cs_2AgSbCl_6$, and $RbSn_2Br_5$ can be mentioned.[193–197] These types of samples exhibited tunable optical properties, with band gaps ranging from 2.12 to 3.6 eV, and have demonstrated potential for applications in photovoltaics, optoelectronics, and photocatalysis. In **Figure** 19A,B, optical data of well-crystallized Cs_4PbX_6 (X = Br, I), obtained via mechanochemical methods, is presented, after a proper DFT simulation. The research highlights the superior stability of all-inorganic perovskites compared to their hybrid counterparts, particularly in terms of moisture resistance.[193] The study also uncovers the potential for ionic mobility within the crystal lattice, which could be advantageous for enhancing the material's performance in solar applications (i.e., solar cell or photocatalysis). The findings underscore the importance of considering both the halide composition and the dimensionality of the perovskite structure to achieve improved optical device performance. Additionally, the optical band gap (2.68–3.36 eV) and PL emission (2.31–2.58 eV) were tunable by synthesizing mixed halide compounds $RbSn_2Br_3Cl_2$ and $RbSn_2Br_4I$ (Figure 19F,G). The dielectric properties exhibited strong frequency dependence, with the primary contribution to impedance arising from the grain. This work highlights the potential of Sn(II)-based metal halides as environmentally friendly alternatives to lead-based materials, with promising applications in optoelectronics and photocatalytic schemes.[197]

In situ analysis during sample preparation by mechanochemistry is another line that should provide fine optimization of beneficial properties for photocatalytic applications. In addition to common monitoring based on techniques that provide structural information such as Raman, XRD, FTIR, etc., the evaluation of properties in optical terms is of special interest. In this

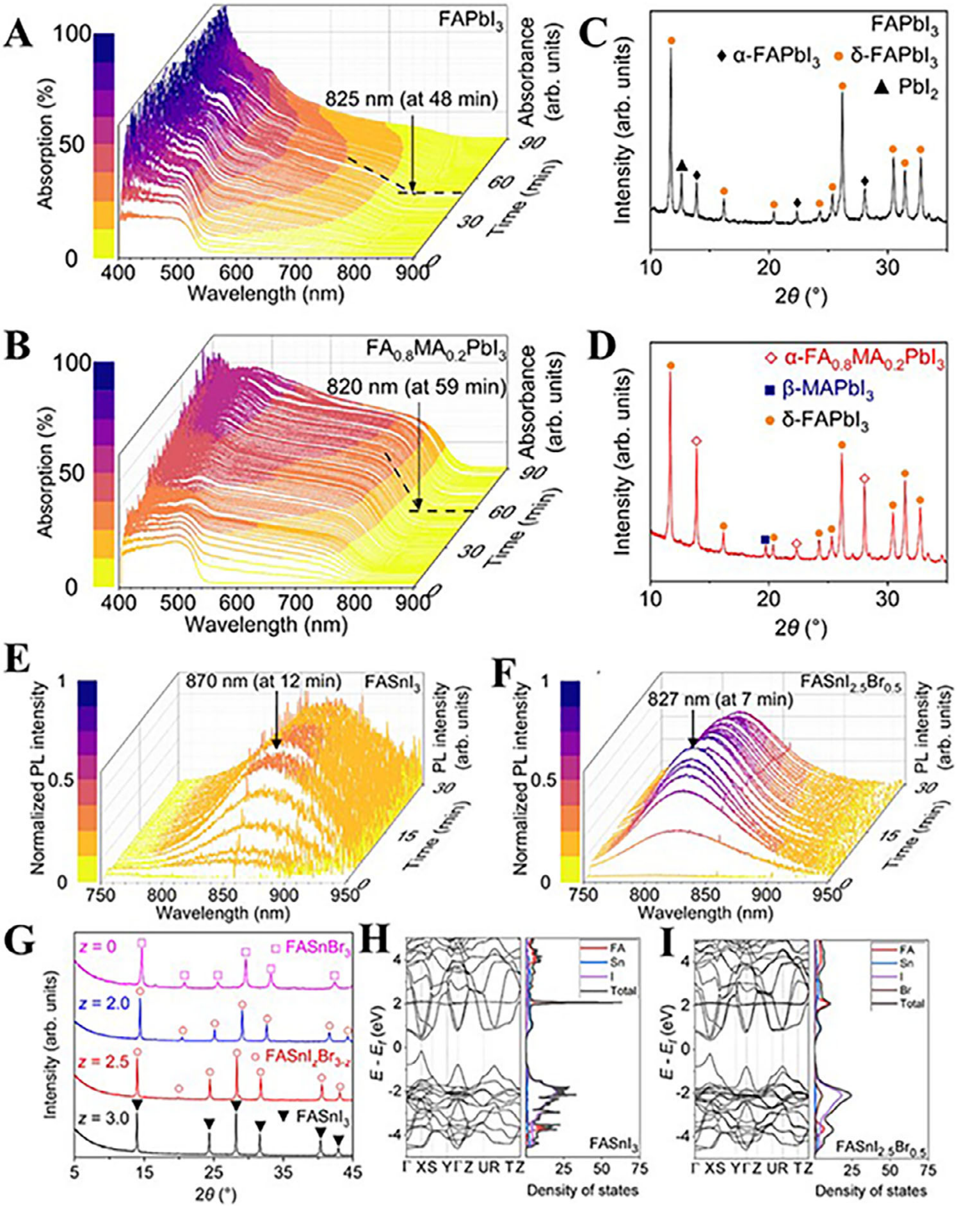

Figure 20. Time-lapsed in situ UV–visible absorption spectra under a N_2 atmosphere and the corresponding XRD data of $FA_xMA_{1-x}PbI_3$ and $FAPbI_3$ samples. A) $x = 1$, B) $x = 0.8$, and XRD results for D) $x = 1$, E) $x = 0.8$. Time-lapsed in situ PL, XRD, and DFT calculation data of the $FASnI_zBr_{3-z}$ samples (where z = 3.0, 2.5, 2.0, 0). TLIS PL spectra of $FASnI_zBr_{3-z}$ for E: z = 3 and F) z = 2. G) XRD patterns of $FASnI_zBr_{3-z}$ (where z = 3.0, 2.5, 2.0, 0). Electronic band structure and partial density of states of $FASnI_zBr_{3-z}$ for H) z = 3.0 and (I) z = 2.5. Modified with permission from ref. [198].

sense, UV–VIS measurements to identify absorption shoulders and therefore band gap values, as well as PL measurements that can be correlated with charge recombination, are especially relevant. In this line, the study by Yonghao Xiao et. al. introduces a novel time-lapsed in situ (TLIS) optical spectrometer designed to monitor the mechanochemical synthesis of metal halide perovskites in real-time.[198] By employing the TLIS spectrometer, the researchers were able to observe the optical properties and structural dynamics of $FA_xMA_{1-x}PbI_3$ perovskites during synthesis, optimizing the synthesis duration and enhancing light-harvesting properties (**Figure** 20A,B). The approach developed in terms of PL can be observed in Figure 20E,F. The authors describe the analysis of the PL intensity of various compositions of $FASnI_zBr_{3-z}$. It was observed that the PL signal of $FASnI_3$ reached its maximum after 12 min but gradually decayed over time. With increasing Br content, the PL peak position shifted toward the blue. The highest PL intensity was observed for $FASnI_{2.5}Br_{0.5}$, which was five times higher than that of $FASnI_3$, reaching its peak after 7 min of milling. However, $FASnI_{2.5}Br_{0.5}$ also exhibited instability, leading to a decay in the PL signal. The XRD data indicated that the cubic Pm3m phase was retained across the entire compositional range, with a shift to higher angles from z = 3.0 to 0, consistent with the decrease in lattice spacings due to the smaller ionic radius of Br compared to I. DFT calculations were employed to investigate the enhanced PL intensity of $FASnI_{2.5}Br_{0.5}$ compared to $FASnI_3$. The DFT-computed band structure and partial densities of states suggested that additional electronic states near the valence band edge increased the transition probability from the valence band maximum to the conduction band minimum, thereby enhancing the PL intensity, which could account for the observed enhancement in $FASnI_{2.5}Br_{0.5}$ compared to $FASnI_3$ (Figure 20H,I).

While halide perovskites have demonstrated remarkable photocatalytic performance under visible light, their long-term stability and potential toxicity issues prompt the exploration of alternative materials. In this context, MXenes, a class of 2D transition metal carbides, nitrides, and carbonitrides, have garnered increasing attention as promising photocatalytic materials due to their intrinsic layered structure, high electrical conductivity, and favorable band edge positions.[199,200] Their multi-layered configuration can facilitate effective charge transport and suppress electron–hole recombination, which is critical for enhancing photocatalytic efficiency.[201] Despite these advantages, current applications of MXenes synthesized via mechanochemical methods remain confined to fields such as electrocatalysis, lithium/sodium-ion battery electrodes, and pollutant degradation.[202–209]

To date, reports involving MXenes for photocatalytic CO_2 reduction or H_2 production have predominantly employed conventional synthesis routes, such as solution-phase exfoliation, acid etching, or hydrothermal treatments.[199,210,211] These studies have demonstrated the potential of MXenes in light-driven processes, yet none have investigated their use when prepared via mechanochemical strategies.[199,201,212,213] Nevertheless, recent works have successfully developed mechanochemical protocols for MXene synthesis, indicating their synthetic feasibility without the use of hazardous etchants or energy-intensive procedures.[202]

Given these considerations, the integration of mechanochemical synthesis into MXene-based photocatalyst development represents an appealing future direction. Mechanochemically derived MXenes could offer a more sustainable and scalable pathway to access highly active and structurally robust catalysts for visible-light-driven CO_2 reduction and hydrogen evolution. The combination of green synthesis with the promising photocatalytic properties of MXenes makes them attractive candidates for inclusion in next-generation solar fuel systems.

Although these examples have not been directly evaluated by the authors in reactions aimed at fuel production or the generation of alternative energy carriers such as hydrogen, the electronic and optical properties described in the selected works demonstrate significant potential for such applications. These features position the materials as promising candidates for further investigation in the field of energy conversion and utilization. In particular, their compatibility with mechanochemical synthesis strategies reinforces their appeal, offering a versatile platform for the development of efficient and scalable materials.

4. Mechanochemistry: A Sustainable Path to Fuel Production

While this review primarily focuses on the role of mechanochemistry in the development of advanced materials, it is also important to highlight the potential applications of this methodology for direct fuel production. This section explores how mechanochemistry can be applied directly to the production of fuels, such as hydrogen and methane, through solid/gas reactions. It also addresses the challenges of performing mechanochemical reactions involving gases, including the control of reaction conditions, gas–solid interactions, and the scalability of such processes. By examining these aspects, we aim to provide a broader understanding of the versatility and challenges of mechanochemical techniques in the context of energy production.

In the context of direct fuel production, mechanochemical force acts as more than a tool for material synthesis; it can actively drive chemical transformations by supplying the activation energy required to initiate solid–gas reactions under mild conditions. Mechanical impact, friction, and shear forces can promote bond cleavage and electron transfer processes without the need for high external temperatures or solvents. In solid/gas systems for hydrogen or methane production, mechanochemical activation can enhance gas–solid contact, facilitate reactant diffusion, and even transiently generate localized high-pressure/high-temperature zones at the point of impact, which are critical for overcoming kinetic barriers. These conditions can trigger redox reactions, promote defect formation, and activate inert substrates, making mechanochemistry a compelling route for sustainable fuel generation.

In this regard, one notable example is the wet mechanochemical processing of olivine under a CO_2 atmosphere. Olivine is an orthosilicate mineral with the general chemical formula $(Fe_xMg_{1-x})_2SiO_4$, comprising a solid mixture between forsterite (Mg_2SiO_4) and fayalite (Fe_2SiO_4), with the magnesium component typically being the most abundant (≈92%). Under mechanochemical conditions, this mineral not only sequesters CO_2 as $MgCO_3$ but also reduces CO_2 to methane at room temperature. The milling chamber was equipped with a valve for CO_2 loading and was linked to a dedicated gas line. To ensure the reaction gas's purity, sequential vacuum and CO_2 charging steps were carried out. Following each milling process, gas samples were extracted from the chamber and analyzed using gas-phase FTIR and GC-FID techniques. The yield of CO_2 sequestration and CH_4 production varies depending on milling duration and CO_2 pressure.[214]

A further development in mechanochemical CO_2 utilization involves the mechanochemical solid/gas reaction of light metal hydrides (LiH, NaH, MgH_2, and CaH_2) with CO_2 to generate methane and hydrogen fuel mixtures at room temperature. Ball milling was conducted at speeds ranging from 350 to 550 rpm for durations between 1 and 48 h using a planetary mill. To limit temperature variations, milling was intermittently paused for 30 min after every hour of operation. While the authors stated that the process occurred at room temperature, it is important to note that one of the common challenges in ball milling is the difficulty of maintaining precise temperature control throughout the process. This one-pot mechanochemical reaction was highly selective, with methane being the sole hydrocarbon product, and its yield depending on the species of metal hydride, milling duration, and CO_2 pressure.[21]

Another noteworthy breakthrough is the mechanocatalytic water-splitting reaction, which was serendipitously discovered

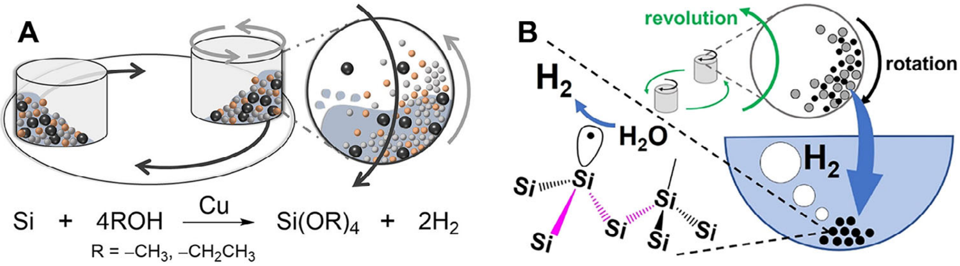

Figure 21. A) Schematic illustration of the Si–alcohol mechanochemical reaction using a planetary ball mill. Reproduced with permission from ref. [215]. B) Mechanochemically tailored silicon particles for efficient H_2 production. Reproduced with permission from ref. [216].

and subsequently refined by Saitow and colleagues. In more detail, six different metals and their corresponding oxides were chosen for this study, including Al, Zn, Fe, and Mn—commonly used in conventional metal–steam reactions—along with Ti and Sn. These metals underwent mechanochemical treatment in distilled water, while real-time monitoring tracked temperature and pressure changes inside the milling chamber. The recorded temperature remained within 30–38 °C, while pressure varied between 2 and 8 bar. The highest pressure, reaching 8 bar, was observed exclusively for the reaction involving Ti, attributed to the significant hydrogen generation. Analysis of the resulting gas mixture indicated it contained ≈87% H_2, 12% Ar, and less than 0.9% water vapor. The process occurs under supercritical water conditions at impact sites between the milling balls, where local temperature and pressure are significantly elevated.[16]

Mechanochemical reactions are also being applied in the synthesis of alkoxysilanes, important precursors for silicone materials. In this sense, it was found that milling a mixture of Si, Cu, and ethanol results in the efficient production of tetraethoxysilane (TEOS) at room temperature, with the additional generation of hydrogen as a byproduct (**Figure** 21A). The use of stainless-steel milling media as a mechanocatalyst in this process suggests that mechanochemistry could enable green, low-temperature, one-pot synthesis methods for high-purity chemicals and fuels.[215]

In addition, mechanochemical reactions between silicon and water offer a promising route for hydrogen production, particularly by repurposing discarded solar cells as a silicon source. For instance, in the work by Tomoya Mizutani et al, milling silicon particles with water at low temperatures (30–70 °C) enables hydrogen generation, with efficiency dependent on precise control over particle properties and milling conditions (Figure 21B). Interestingly, two common assumptions: that higher mechanical energy always improves the reaction and that larger surface areas enhance efficiency, were disproven. The most effective hydrogen production was achieved with silicon particles milled for just 3 min, without any chemical additives. Key factors such as enthalpy, entropy, mechanical energy input, and structural characteristics of the milled particles were analyzed to define the Gibbs free energy and activation barrier of the reaction, shedding light on the underlying mechanism. Additionally, scaling up the process improved its energy efficiency to levels comparable to electrolysis, suggesting that mechanochemical hydrogen production could be a viable and sustainable alternative for the future.[216]

Pushing the mechanochemical-water-splitting concept forward, the exploration of piezoelectric nanostructures further extends the scope of mechanochemistry in fuel production. By converting mechanical energy into electrical charges, piezoelectric materials, such as ZnO and $BaTiO_3$, can drive water splitting reactions when subjected to vibrations, stirring, or ultrasonication. This ability to directly convert mechanical energy into chemical fuel generation offers an alternative to traditional electrolysis, contributing to the growing interest in sustainable energy technologies.[217]

Despite the promising potential of mechanochemistry for direct fuel production, the scalability of these processes remains a major unresolved challenge. A key limitation lies in the inherently low throughput of conventional ball milling, which typically operates in batch mode. While extrusion offers a more promising platform for scale-up due to its continuous nature and higher material throughput, its application to gas-solid reactions is still largely unexplored. Critical bottlenecks include inefficient gas dosing, non-uniform gas–solid contact along the extruder, and safety risks associated with operating under pressurized or reactive gas environments. Moreover, most current setups are designed for solid–solid or solid-liquid (LAG) processes and are not equipped for precise control or real-time monitoring of gas-phase reactions. These technical limitations severely constrain the transferability of lab-scale findings to industrial contexts. Thus, while the field holds long-term promise, the development of robust, scalable reactors and new engineering strategies is essential before mechanochemical fuel production can become a practical alternative to established technologies.

5. Conclusions and Future Perspectives

Mechanochemistry has emerged as a powerful strategy for designing and tuning photocatalysts, offering solvent-free and energy-efficient pathways for material synthesis. Its ability to control structural and electronic properties at the nanoscale has led to advances in photocatalysis, particularly in hydrogen production and CO_2 photoreduction. However, despite its potential, significant challenges remain before mechanochemical methods can be fully established as a mainstream approach in solar fuel production.

One of the primary limitations is that most reported studies still employ hybrid synthesis approaches, where mechanochemistry is used for one step while conventional solution-based methods are necessary for others. While completely eliminating solution-based protocols is not always feasible, particularly for surface modifications, templating, or post-synthetic treatments, it is crucial to prioritize mechanochemical routes whenever possible to maximize sustainability benefits. Future research should focus on minimizing the reliance on solvents and optimizing solid-state reaction conditions to achieve fully mechanochemical workflows without compromising material quality.

A particularly promising yet underdeveloped area is the use of extrusion as a scalable mechanochemical technique. While ball milling has become a standard tool for synthesizing photocatalysts in the lab, its batch nature makes it difficult to translate directly to industrial processes. Extrusion, on the other hand, offers a continuous approach that allows for better control over temperature, shear forces, and reaction time, all of which can play a key role in tuning the properties of the final material. This technique has the potential to generate photocatalysts with precisely engineered morphology, crystallinity, and defect structures, opening new possibilities for large-scale applications. Given its energy efficiency, green chemistry credentials, and scalability, extrusion deserves much more attention in future research as a platform for producing advanced photocatalysts with industrial relevance.

Beyond synthesis techniques, the sustainability of mechanochemically produced photocatalysts also depends on the choice of precursors. A transition toward renewable feedstocks, such as biomass-derived sources, could significantly reduce the environmental impact of material production. The development of methodologies that integrate bio-based precursors without compromising photocatalytic performance will be a crucial step toward more sustainable solar fuel technologies.

Moreover, the effectiveness of photocatalysts is ultimately dictated by their optical properties and ability to efficiently utilize solar energy. Mechanochemistry has been instrumental in tuning band structures, defect densities, and surface states, yet many synthesized materials still exhibit limited visible-light absorption. More efforts are still required to integrate mechanochemistry with complementary strategies, such as co-catalyst deposition, heterojunction formation, and plasmonic enhancement, to optimize light harvesting and charge separation. Additionally, the determination of the local superficial/volumetric rate of photon absorption profiles must be accomplished.[218] The determination of this observable, which is defined as Einstein $m^{-2}s^{-1}$ (in catalytic films) or Einstein $cm^{-3}s^{-1}$, would allow the precise quantification of activity in terms of quantum efficiency, which is relevant for comparison with materials obtained by traditional methods and the subsequent scaling of reaction systems.[219,220]

An emerging frontier in this field is photomechanochemistry, where light and mechanical energy act synergistically to drive chemical transformations.[221–223] While still in its infancy, this approach holds significant potential for fuel production by enabling light-assisted mechanochemical activation of reactants, potentially lowering activation barriers and improving reaction selectivity. The development of photocatalysts that can efficiently couple mechanical and photonic energy inputs could lead to novel reaction pathways for solar fuel generation, making photomechanochemistry a promising direction for future research.[224]

Looking ahead, another exciting direction involves the integration of mechanochemistry with digital and analytical tools. For example, using machine learning to guide the optimization of parameters, such as milling speed, extrusion temperature, or material ratios, could significantly accelerate the discovery of new photocatalysts. At the same time, coupling these processes with in situ characterization techniques, like synchrotron-based X-ray diffraction or real-time Raman spectroscopy, could provide valuable insights into how materials evolve during synthesis. Together, these innovations could make mechanochemistry not just more efficient and scalable, but also more predictable, reproducible, and fundamentally understood, key steps toward bridging the gap between lab research and real-world applications.

Ultimately, the widespread adoption of mechanochemistry in photocatalyst synthesis will depend on overcoming both scientific and practical challenges. While its advantages in terms of sustainability and energy efficiency are clear, its successful integration into real-world applications will require advancements in material properties control and scalability. By addressing these challenges, mechanochemistry could play a transformative role in next-generation solar fuel production, contributing to a cleaner and more sustainable energy future.

Acknowledgements

D.R.-P. received funding from the European Union's Horizon2020 Research and Innovation Programme under the Marie Sklodowska-Curie Cofund Grant Agreement No. 945361. M.J.M-B acknowledges funding from the project PID2022-139014OB-I00/SRA (State Research Agency)/10.13039/501100011033.

Conflict of Interest

The authors declare no conflict of interest.

Keywords

carbon dioxide photoreduction, hydrogen photoproduction, mechanochemistry, visible-light photocatalytic materials

Received: March 17, 2025
Revised: July 9, 2025
Published online: July 23, 2025

---

[1] P. Preuster, A. Alekseev, P. Wasserscheid, *Annu. Rev. Chem. Biomol. Eng.* **2017**, *8*, 445.
[2] S. Griffiths, *Energy Strategy Rev.* **2019**, *26*, 100386.
[3] P. P. Edwards, V. L. Kuznetsov, W. I. F. David, *Philos. Trans. R. Soc., A* **2007**, *365*, 1043.
[4] K. Oshiro, S. Fujimori, *Appl. Energy* **2022**, *313*, 118803.
[5] A. Awad, T. Veziroglu, *Int. J. Hydrogen Energy* **1984**, *9*, 355.
[6] P. Nikolaidis, A. Poullikkas, *Renew. Sustain. Energy Rev.* **2017**, *67*, 597.
[7] I. Dincer, *Int. J. Energy Res.* **2007**, *31*, 29.
[8] I. Dincer, *Int. J. Hydrogen Energy* **2002**, *27*, 265.
[9] A. Bhisikar, M. N. Singh, N. Khantwal, A. K. Sinha, *Mater. Today Commun.* **2022**, *33*, 104138.
[10] M. R. Usman, *Renew. Sustain. Energy Rev.* **2022**, *167*, 112743.
[11] M. Younas, S. Shafique, A. Hafeez, F. Javed, F. Rehman, *Fuel* **2022**, *316*, 123317.
[12] J. A. Turner, *Science 1979* **2004**, *305*, 972.
[13] I. Staffell, D. Scamman, A. Velazquez Abad, P. Balcombe, P. E. Dodds, P. Ekins, N. Shah, K. R. Ward, *Energy Environ. Sci.* **2019**, *12*, 463.

[14] R. Bhandari, C. A. Trudewind, P. Zapp, *J. Clean. Prod.* **2014**, *85*, 151.
[15] A. L. Dicks, *J. Power Sources* **1996**, *61*, 113.
[16] T. Yamamoto, S. Ashida, N. Inubuse, S. Shimizu, Y. Miura, T. Mizutani, K. Saitow, *J. Mater. Chem. A Mater.* **2024**, *12*, 30906.
[17] B. Li, Y. Duan, D. Luebke, B. Morreale, *Appl. Energy* **2013**, *102*, 1439.
[18] E. V. Kondratenko, G. Mul, J. Baltrusaitis, G. O. Larrazábal, J. Pérez-Ramírez, *Energy Environ. Sci.* **2013**, *6*, 3112.
[19] Y. Fu, Y. Li, X. Zhang, Y. Liu, J. Qiao, J. Zhang, D. P. Wilkinson, *Appl. Energy* **2016**, *175*, 536.
[20] D. P. Hanak, E. J. Anthony, V. Manovic, *Energy Environ. Sci.* **2015**, *8*, 2199.
[21] B.-X. Dong, J. Zhao, L.-Z. Wang, Y.-L. Teng, W.-L. Liu, L. Wang, *Appl. Energy* **2017**, *204*, 741.
[22] S. Ahmed, M. Irshad, W. Yoon, N. Karanwal, J. R. Sugiarto, M. K. Khan, S. K. Kim, J. Kim, *Appl. Catal. B* **2023**, *338*, 123052.
[23] X. Duan, J. Xu, Z. Wei, J. Ma, S. Guo, S. Wang, H. Liu, S. Dou, *Adv. Mater.* **2017**, *29*, 1701784.
[24] C. D. Windle, R. N. Perutz, *Coord. Chem. Rev.* **2012**, *256*, 2562.
[25] I.-H. Tsai, C.-W. Huang, C.-F. Chang, E. Wei-Guang Diau, I. Tsai, C. Huang, C. Chang, E. W.-G. Diau, *Small* **2025**, *21*, 2409023.
[26] A. I. Martín-Perales, A. M. Balu, I. Malpartida, R. Luque, *Curr. Opin. Green Sustain. Chem.* **2022**, *38*, 100714.
[27] O. Trentin, D. Ballesteros-Plata, E. Rodríguez-Castellón, L. Puppulin, M. Selva, A. Perosa, D. Rodríguez-Padrón, *ChemSusChem* **2024**, *18*, 202401255.
[28] F. Zorzetto, D. Ballesteros-Plata, A. Perosa, E. Rodríguez-Castellón, M. Selva, D. Rodríguez-Padrón, *Green Chem.* **2024**, *26*, 5221.
[29] O. Trentin, D. Polidoro, A. Perosa, E. Rodríguez-Castellon, D. Rodríguez-Padrón, M. Selva, *Chemistry* **2023**, *5*, 1760.
[30] N. Fantozzi, J. N. Volle, A. Porcheddu, D. Virieux, F. García, E. Colacino, *Chem. Soc. Rev.* **2023**, *52*, 6680.
[31] D. Hasa, W. Jones, *Adv. Drug Deliv. Rev.* **2017**, *117*, 147.
[32] K. Wang, F. Zhang, N. Cao, Y. Bao, M. Yan, K. Yan, P. Xie, *Sci China Chem* **2024**, *67*, 4125.
[33] F. Zhou, B. Zhang, H. Wang, D. Wang, X. Qu, S. Wang, M. Tang, L. Peng, X. Chen, D. Wang, L. Y. S. Lee, H. Yin, *Green Chem.* **2025**, *27*, 7918.
[34] H. Ghayour, M. Abdellahi, M. Bahmanpour, *Powder Technol.* **2016**, *291*, 7.
[35] M. Abdellahi, M. Bahmanpour, *Ceram. Int.* **2015**, *41*, 1631.
[36] P. P. Chattopadhyay, I. Manna, S. Talapatra, S. K. Pabi, *Mater. Chem. Phys.* **2001**, *68*, 85.
[37] A. E. Mariño-Gámez, G. E. Acosta-González, M. I. Pech-Canul, M. B. Hernández, S. García-Villarreal, P. Zambrano-Robledo, B. S. Vera Barrios, J. A. Aguilar-Martínez, *Ceram. Int.* **2022**, *48*, 3362.
[38] J. Alkebro, S. Bégin-Colin, A. Mocellin, R. Warren, *J. Solid State Chem.* **2002**, *164*, 88.
[39] C. Marchal, A. Piquet, M. Behr, T. Cottineau, V. Papaefthimiou, V. Keller, V. Caps, *J. Catal.* **2017**, *352*, 22.
[40] C. Marchal, M. Behr, F. Vigneron, V. Caps, V. Keller, *New J. Chem.* **2016**, *40*, 4428.
[41] L. Martínez, M. Benito, I. Mata, L. Soler, E. Molins, J. Llorca, *Sustain. Energy Fuels* **2018**, *2*, 2284.
[42] Y. Chen, L. Soler, C. Xie, X. Vendrell, J. Serafin, D. Crespo, J. Llorca, *Appl. Mater. Today* **2020**, *21*, 100873.
[43] Y. Chen, L. Soler, M. Armengol-Profitós, C. Xie, D. Crespo, J. Llorca, *Appl. Catal. B* **2022**, *309*, 121275.
[44] Y. Chen, L. Soler, C. Cazorla, J. Oliveras, N. G. Bastús, V. F. Puntes, J. Llorca, *Nat. Commun.* **2023**, *4*, 6165.
[45] Y. Kageshima, S. Kato, S. Shiga, F. Takagi, H. Minamisawa, M. Horita, T. Yamakami, K. Teshima, K. Domen, H. Nishikiori, *ACS Appl. Mater. Interfaces* **2023**, *15*, 13108.
[46] B. G. Fiss, N. N. Vu, G. Douglas, T. O. Do, T. Friščić, A. Moores, *ACS Sustain. Chem. Eng.* **2020**, *8*, 12014.
[47] G. Chen, D. Li, F. Li, Y. Fan, H. Zhao, Y. Luo, R. Yu, Q. Meng, *Appl Catal A Gen* **2012**, *443–444*, 138.
[48] S. Paul, S. K. Pradhan, *Phys. B Condens. Matter* **2024**, *687*, 416086.
[49] R. Rameshbabu, P. Ravi, G. Pecchi, E. J. Delgado, R. V. Mangalaraja, M. Sathish, *J. Colloid Interface Sci.* **2021**, *590*, 82.
[50] Z. Shalabayev, M. Baláž, N. Khan, Y. Nurlan, A. Augustyniak, N. Daneu, B. Tatykayev, E. Dutková, G. Burashev, M. Casas-Luna, R. Džunda, R. Bureš, L. Čelko, A. Ilin, M. Burkitbayev, *Nanomaterials* **2022**, *12*, 1250.
[51] Z. Shalabayev, A. Abilkhan, N. Khan, S. Tugelbay, A. Seisembekova, B. Tatykayev, M. Balaz, *Nanomaterials* **2024**, *14*, 1785.
[52] P. Gomathisankar, K. Hachisuka, H. Katsumata, T. Suzuki, K. Funasaka, S. Kaneco, *RSC Adv.* **2013**, *3*, 20429.
[53] A. Pollap, J. Serafin, I. Serrano, J. Srenscek-Nazzal, J. Llorca, *J. Environ. Chem. Eng.* **2022**, *10*, 108877.
[54] D. Ni, H. Shen, H. Li, Y. Ma, T. Zhai, *Appl. Surf. Sci.* **2017**, *409*, 241.
[55] M. Muscetta, S. Al Jitan, G. Palmisano, R. Andreozzi, R. Marotta, S. Cimino, I. Di Somma, *J. Environ. Chem. Eng.* **2022**, *10*, 107735.
[56] M. Umair, A. Ruiz-Aguirre, I. Berruti, S. M. Rodríguez, L. Palmisano, V. Loddo, M. Bellardita, *Chem. Eng. J.* **2025**, *504*, 158585.
[57] Y. Wang, K. I. Saitow, *Chem. Mater.* **2020**, *32*, 9190.
[58] E. do Couto-Pessanha, V. M. Paiva, T. J. A. Mori, L. Soler, B. Canabarro, P. Jardim, E. D'Elia, J. Llorca, B. A. Marinkovic, *Int. J. Hydrogen Energy* **2024**, *80*, 528.
[59] Y. Zhu, Q. Ling, Y. Liu, H. Wang, Y. Zhu, *Phys. Chem. Chem. Phys.* **2014**, *17*, 933.
[60] X. Gao, B. Niu, Z. Xu, *ACS Sustain. Chem. Eng.* **2024**, *12*, 17272.
[61] D. M. Cañas-Martínez, S. Cipagauta-Díaz, M. Manrique, R. Gómez, J. A. Pedraza-Avella, *Top. Catal.* **2021**, *64*, 2.
[62] Z. Jin, M. Yang, Z. Fan, Y. Li, *Sustain. Energy Fuels* **2022**, *6*, 4506.
[63] X. Li, M. Lei, Z. Jin, *J. Catal.* **2023**, *428*, 115131.
[64] Z. Zhou, J. Wang, M. Reheimujiang, Z. Jin, *J. Mater. Sci. Technol.* **2025**, *213*, 241.
[65] Y. Xiao, Z. Wang, L. Li, Q. Gu, M. Xu, L. Zhu, X. Fu, *Int. J. Hydrogen Energy* **2023**, *48*, 15460.
[66] X. Wang, X. Wang, W. Tian, A. Meng, Z. Li, S. Li, L. Wang, G. Li, *Appl. Catal. B* **2022**, *303*, 120933.
[67] A. Meng, W. Tian, H. Yang, X. Wang, X. Wang, Z. Li, *J. Hazard. Mater.* **2021**, *413*, 125400.
[68] M. Wen, N. Yang, J. Wang, D. Liu, W. Zhang, S. Bian, H. Huang, X. He, X. Wang, S. Ramakrishna, P. K. Chu, S. Yang, X. F. Yu, *ACS Appl. Mater. Interfaces* **2021**, *13*, 50988.
[69] M. Hu, J. Zhu, W. Guo, Q. Xu, Y. Min, J. Fan, *ACS Sustain. Chem. Eng.* **2022**, *10*, 1008.
[70] S. H. Bu, W. Cho, C. Lee, G. Ham, B. Yang, J. Jung, H. Cha, C. Park, *Chem. Eng. J.* **2024**, *502*, 157688.
[71] M. Guo, M. Chen, J. Xu, C. Wang, L. Wang, *Chem. Eng. J.* **2023**, *461*, 142046.
[72] G. Ba, T. Huo, Q. Deng, H. Li, W. Hou, *ACS Sustain. Chem. Eng.* **2020**, *8*, 18606.
[73] X. Chen, H. Chen, J. Guan, J. Zhen, Z. Sun, P. Du, Y. Lu, S. Yang, *Nanoscale* **2017**, *9*, 5615.
[74] W. Liu, T. Yanase, N. Iwasa, H. Koizumi, S. Mukai, S. Iwamura, T. Nagahama, T. Shimada, *Int. J. Hydrogen Energy* **2020**, *45*, 8444.
[75] O. Y. Posudievsky, A. S. Kondratyuk, O. A. Kozarenko, V. V. Cherepanov, V. G. Koshechko, V. D. Pokhodenko, *Int. J. Hydrogen Energy* **2019**, *44*, 17922.
[76] T. Mi, F. Zhao, Y. Y. Dong, J. Zhao, J. Zhao, X. Zhong, N. Zhang, P. Tsiakaras, *J. Colloid Interface Sci.* **2023**, *636*, 230.
[77] X. Zhu, T. Zhang, Z. Sun, H. Chen, J. Guan, X. Chen, H. Ji, P. Du, S. Yang, *Adv. Mater.* **2017**, *29*, 1605776.
[78] S. D. Stranks, H. J. Snaith, *Nat. Nanotechnol.* **2015**, *10*, 391.
[79] A. D. Jodlowski, D. Rodríguez-Padrón, R. Luque, G. de Miguel, *Adv. Energy Mater.* **2018**, *8*, 1703120.

[80] H. Huang, B. Pradhan, J. Hofkens, M. B. J. Roeffaers, J. A. Steele, *ACS Energy Lett.* **2020**, *5*, 1107.
[81] C. Zheng, O. Rubel, *J. Phys. Chem. C* **2019**, *123*, 19385.
[82] J. A. Christians, P. A. Miranda Herrera, P. V. Kamat, *J. Am. Chem. Soc.* **2015**, *137*, 1530.
[83] X. Zhu, Y. Lin, J. San Martin, Y. Sun, D. Zhu, Y. Yan, *Nat. Commun.* **2019**, *10*, 2843.
[84] Z. Zhao, J. Wu, Y. Z. Zheng, N. Li, X. Li, X. Tao, *ACS Catal.* **2019**, *9*, 8144.
[85] S. Park, W. J. Chang, C. W. Lee, S. Park, H. Y. Ahn, K. T. Nam, *Nat. Energy* **2016**, *2*, 16185.
[86] M. Wang, Y. Zuo, J. Wang, Y. Wang, X. Shen, B. Qiu, L. Cai, F. Zhou, S. P. Lau, Y. Chai, *Adv. Energy Mater.* **2019**, *9*, 1901801.
[87] Z. Zhao, J. Wu, Y. Z. Zheng, N. Li, X. Li, Z. Ye, S. Lu, X. Tao, C. Chen, *Appl. Catal. B* **2019**, *253*, 41.
[88] A. Pisanu, A. Speltini, P. Quadrelli, G. Drera, L. Sangaletti, L. Malavasi, *J. Mater. Chem. C Mater.* **2019**, *7*, 7020.
[89] D. Ju, X. Zheng, J. Liu, Y. Chen, J. Zhang, B. Cao, H. Xiao, O. F. Mohammed, O. M. Bakr, X. Tao, *Angew. Chem., Int. Ed.* **2018**, *57*, 14868.
[90] A. D. Jodlowski, A. Yépez, R. Luque, L. Camacho, G. de Miguel, *Angew. Chem., Int. Ed.* **2016**, *55*, 14972.
[91] L. Romani, A. Speltini, F. Ambrosio, E. Mosconi, A. Profumo, M. Marelli, S. Margadonna, A. Milella, F. Fracassi, A. Listorti, F. De Angelis, L. Malavasi, *Angew. Chem.* **2021**, *133*, 3655.
[92] Z. Durmus, A. W. Maijenburg, *Int. J. Hydrogen Energy* **2022**, *47*, 36784.
[93] B. Zhu, R. Zou, Q. Xu, B. Zhu, R. Zou, Q. Xu, *Adv. Energy Mater.* **2018**, *8*, 1801193.
[94] S. Dai, E. Montero-Lanzuela, A. Tissot, H. G. Baldoví, H. García, S. Navalón, C. Serre, *Chem. Sci.* **2023**, *14*, 3451.
[95] H. Yang, J. Wang, J. Ma, H. Yang, J. Zhang, K. Lv, L. Wen, T. Peng, *J Mater Chem A Mater* **2019**, *7*, 10439.
[96] T. Liao, L. Kou, A. Du, Y. Gu, Z. Sun, *J. Am. Chem. Soc.* **2018**, *140*, 9159.
[97] M. El Ouardi, A. El aouni, H. Ait Ahsaine, M. Zbair, A. BaQais, M. Saadi, *Chemosphere* **2022**, *308*, 136483.
[98] R. Nivetha, P. Kollu, K. Chandar, S. Pitchaimuthu, S. K. Jeong, A. N. Grace, *RSC Adv.* **2019**, *9*, 3215.
[99] F. Jin, B. Yang, X. Wang, T. Li, N. Tsubaki, Z. Jin, *Chin. J. Struct. Chem.* **2023**, *42*, 100198.
[100] K. Wang, X. Kong, H. Xie, S. Li, M. Wang, Z. Jin, *Dalton Trans.* **2023**, *52*, 8716.
[101] S. Feng, S. Ning, L. Wang, J. Zhao, J. Ou, Z. Wu, S. Luo, Z. Lin, K. Yan, C. Wu, Y. Xu, *ACS Appl. Energy Mater.* **2022**, *5*, 6248.
[102] Y. Wu, Y. Qu, C. Su, X. Yang, Y. Yang, Y. Zhang, W. Huang, *Inorg. Chem.* **2023**, *62*, 21290.
[103] B. Karadeniz, A. J. Howarth, T. Stolar, T. Islamoglu, I. Dejanović, M. Tireli, M. C. Wasson, S. Y. Moon, O. K. Farha, T. Friščić, K. Užarević, *ACS Sustain Chem Eng* **2018**, *6*, 15841.
[104] G. Ayoub, B. Karadeniz, A. J. Howarth, O. K. Farha, I. Lilović, L. S. Germann, R. E. Dinnebier, K. Užarević, T. Friščić, *Chem. Mater.* **2019**, *31*, 5494.
[105] T. ming Su, Z. zeng Qin, H. bing Ji, Y. xiu Jiang, G. Huang, *Environ. Chem. Lett.* **2015**, *14*, 99.
[106] B. Kumar, M. Llorente, J. Froehlich, T. Dang, A. Sathrum, C. P. Kubiak, *Annu. Rev. Phys. Chem.* **2012**, *63*, 541.
[107] M. S. Fan, A. Z. Abdullah, S. Bhatia, *ChemCatChem* **2009**, *1*, 192.
[108] Q. Guo, C. Zhou, Z. Ma, X. Yang, *Adv. Mater.* **2019**, *31*, 1901997.
[109] J. Lee, S. P. Chai, L. L. Tan, *ACS Energy Lett.* **2024**, *9*, 1932.
[110] K. Teramura, T. Tanaka, H. Ishikawa, Y. Kohno, T. Funabiki, *J. Phys. Chem. B* **2003**, *108*, 346.
[111] Y. Kohno, H. Ishikawa, T. Tanaka, T. Funabiki, S. Yoshida, *Phys. Chem. Chem. Phys.* **2001**, *3*, 1108.
[112] S. Xie, Y. Wang, Q. Zhang, W. Deng, Y. Wang, *ACS Catal.* **2014**, *4*, 3644.
[113] A. Ziarati, A. Badiei, R. Luque, M. Dadras, T. Burgi, *ACS Sustain Chem Eng* **2020**, *8*, 3689.
[114] R. Tang, X. Dong, J. Sheng, S. Xi, L. Zhang, F. Dong, *Appl. Catal. B* **2022**, *316*, 121661.
[115] H. Huang, D. Y. C. Leung, *ACS Catal.* **2011**, *1*, 348.
[116] L. Q. Zhou, C. Ling, H. Zhou, X. Wang, J. Liao, G. K. Reddy, L. Deng, T. C. Peck, R. Zhang, M. S. Whittingham, C. Wang, C. W. Chu, Y. Yao, H. Jia, *Nat. Commun.* **2019**, *10*, 4081.
[117] D. Qian, Y. Hinuma, H. Chen, L. S. Du, K. J. Carroll, G. Ceder, C. P. Grey, Y. S. Meng, *J. Am. Chem. Soc.* **2012**, *134*, 6096.
[118] T. Aoki, M. Yamamoto, T. Tanabe, T. Yoshida, *New J. Chem.* **2022**, *46*, 3207.
[119] R. Ito, M. Akatsuka, A. Ozawa, M. Yamamoto, T. Tanabe, T. Yoshida, *Bull. Chem. Soc. Jpn.* **2020**, *93*, 694.
[120] Q. Li, Y. Zhang, L. Zhang, J. Xia, X. Liu, L. Hu, F. Wang, X. Chu, P. Zhao, J. Yin, D. Yang, *Catal. Commun.* **2019**, *120*, 23.
[121] T. Tong, B. Zhu, C. Jiang, B. Cheng, J. Yu, *Appl. Surf. Sci.* **2018**, *433*, 1175.
[122] C. Zhang, D. Qin, Y. Zhou, F. Qin, H. Wang, W. Wang, Y. Yang, G. Zeng, *Appl. Catal. B* **2022**, *303*, 120904.
[123] Z. Chen, J. Zhao, C. R. Cabrera, Z. Chen, *Small Methods* **2019**, *3*, 1800368.
[124] R. Tang, H. Wang, X. Dong, S. Zhang, L. Zhang, F. Dong, *J. Colloid Interface Sci.* **2023**, *630*, 290.
[125] Y. Xiong, W. Sun, Y. Han, P. Xin, X. Zheng, W. Yan, J. Dong, J. Zhang, D. Wang, Y. Li, *Nano Res.* **2021**, *14*, 2418.
[126] B. Peng, H. Liu, Z. Liu, X. Duan, Y. Huang, *J. Phys. Chem. Lett.* **2021**, *12*, 2837.
[127] J. Montgomery, *Angew. Chem., Int. Ed.* **2004**, *43*, 3890.
[128] G. Wilke, *Angew. Chem. Int. Ed. Engl.* **1988**, *27*, 185.
[129] Y. Wang, Y. Qu, B. Qu, L. Bai, Y. Liu, Z.-D. Yang, W. Zhang, L. Jing, H. Fu, Y. Wang, Y. Qu, B. Qu, L. Bai, Y. Liu, L. Jing, H. Fu, Z.-D. Yang, W. Zhang, *Adv. Mater.* **2021**, *33*, 2105482.
[130] C. Chen, T. Wang, K. Yan, S. Liu, Y. Zhao, B. Li, *Inorg. Chem. Front.* **2022**, *9*, 4753.
[131] R. Tang, H. Wang, X. Dong, L. Zhang, Y. Sun, F. Dong, *J. Colloid Interface Sci.* **2024**, *655*, 243.
[132] T. Liu, T. Xu, T. Li, Y. Jing, *J. Am. Chem. Soc.* **2024**, *146*, 24133.
[133] J. Zhang, J. Fu, K. Dai, *J. Mater. Sci. Technol.* **2022**, *116*, 192.
[134] H. Liu, S. Cao, L. Chen, K. Zhao, C. Wang, M. Li, S. Shen, W. Wang, L. Ge, *Chem. Eng. J.* **2022**, *433*, 133594.
[135] J. Jiang, D. Duan, J. Ma, Y. Jiang, R. Long, C. Gao, Y. Xiong, *Appl. Catal. B* **2021**, *295*, 120261.
[136] J. Dong, J. Zhao, X. Yan, L. Li, G. Liu, M. Ji, B. Wang, Y. She, H. Li, J. Xia, *Appl. Catal. B Environ. Energy* **2024**, *351*, 123993.
[137] N. Yang, Z. J. Zhou, X. Zhu, J. Wu, Y. Zhang, T. Wang, X. P. Wu, C. Tian, X. Jiang, S. Dai, *Angew. Chem., Int. Ed.* **2025**, *64*, 202419108.
[138] H. Li, H. Shang, Y. Shi, R. Yakimova, M. Syväjärvi, L. Zhang, J. Sun, *J Mater Chem A Mater* **2018**, *6*, 24358.
[139] H. Li, Y. Shi, H. Shang, W. Wang, J. Lu, A. A. Zakharov, L. Hultman, R. I. G. Uhrberg, M. Syväjärvi, R. Yakimova, L. Zhang, J. Sun, *ACS Nano* **2020**, *14*, 4905.
[140] J. Jian, Y. Shi, S. Ekeroth, J. Keraudy, M. Syväjärvi, R. Yakimova, U. Helmersson, J. Sun, *J Mater Chem A Mater* **2019**, *7*, 4721.
[141] Y. Wang, L. Zhang, X. Zhang, Z. Zhang, Y. Tong, F. Li, J. C. S. Wu, X. Wang, *Appl. Catal. B* **2017**, *206*, 158.
[142] H. Li, J. Sun, *ACS Appl. Mater. Interfaces* **2021**, *13*, 5073.
[143] S. Kumar, M. Regue, M. A. Isaacs, E. Freeman, S. Eslava, *ACS Appl. Energy Mater.* **2020**, *3*, 4509.
[144] J. Rath, S. Sukanya, S. Biswas, N. Mishra, *Cryst. Growth Des.* **2024**, *24*, 6549.

[145] S. Kumar, I. Hassan, M. Regue, S. Gonzalez-Carrero, E. Rattner, M. A. Isaacs, S. Eslava, *J. Mater. Chem. A Mater.* **2021**, *9*, 12179.
[146] J. Pi, X. Jia, Z. Long, S. Yang, H. Wu, D. Zhou, Q. Wang, H. Zheng, Y. Yang, J. Zhang, J. Qiu, *Adv. Energy Mater.* **2022**, *12*, 2202074.
[147] N. Leupold, K. Schötz, S. Cacovich, I. Bauer, M. Schultz, M. Daubinger, L. Kaiser, A. Rebai, J. Rousset, A. Köhler, P. Schulz, R. Moos, F. Panzer, *ACS Appl. Mater. Interfaces* **2019**, *11*, 30259.
[148] Z. Hong, D. Tan, R. A. John, Y. K. E. Tay, Y. K. T. Ho, X. Zhao, T. C. Sum, N. Mathews, F. García, H. S. Soo, *iScience* **2019**, *16*, 312.
[149] R. Freund, O. Zaremba, G. Arnauts, R. Ameloot, G. Skorupskii, M. Dincă, A. Bavykina, J. Gascon, A. Ejsmont, J. Goscianska, M. Kalmutzki, U. Lächelt, E. Ploetz, C. S. Diercks, S. Wuttke, *Angew. Chem., Int. Ed.* **2021**, *60*, 23975.
[150] M. Ko, L. Mendecki, K. A. Mirica, *Chem. Commun.* **2018**, *54*, 7873.
[151] J. Cao, Z. Yang, W. Xiong, Y. Zhou, Y. Wu, M. Jia, C. Zhou, Z. Xu, *Coord. Chem. Rev.* **2021**, *439*, 213924.
[152] S. Subbareddy, S. Arehalli Shivamurthy, S. Basavapura Ravikumar, H. Mylnahalli Krishnegowda, S. Shadakshari, M. Selvaraj, S. Basumatary, *Mater Today Chem* **2024**, *40*, 102197.
[153] B. Thijs, J. Rongé, J. A. Martens, *Green Chem.* **2022**, *24*, 2287.
[154] D. Li, M. Kassymova, X. Cai, S. Q. Zang, H. L. Jiang, *Coord. Chem. Rev.* **2020**, *412*, 213262.
[155] T. Stolar, A. Prašnikar, V. Martinez, B. Karadeniz, A. Bjelić, G. Mali, T. Friščić, B. Likozar, K. Užarević, *ACS Appl. Mater. Interfaces* **2021**, *13*, 3070.
[156] Y. Zhao, Z. Shao, Y. Cui, K. Geng, X. Meng, J. Wu, H. Hou, Y. Zhao, Y. Cui, K. Geng, X. Meng, J. Wu, H. Hou, Z. Shao, *Small* **2023**, *19*, 2300398.
[157] S. A. Younis, E. E. Kwon, M. Qasim, K. H. Kim, T. Kim, D. Kukkar, X. Dou, I. Ali, *Prog. Energy Combust. Sci.* **2020**, *81*, 100870.
[158] S. Sharma, N. Jacob, G. K. Grandhi, M. B. Choudhary, S. Ippili, V. R. Hathwar, P. Vivo, R. Lo, M. Motapothula, K. Jayaramulu, *iScience* **2024**, *27*, 110924.
[159] K. Jayaramulu, J. Masa, D. M. Morales, O. Tomanec, V. Ranc, M. Petr, P. Wilde, Y.-T. Chen, R. Zboril, W. Schuhmann, R. A. Fischer, J. Masa, D. M. Morales, P. Wilde, W. Schuhmann, Y. Chen, K. Jayaramulu, R. A. Fischer, O. Tomanec, V. Ranc, M. Petr, R. Zboril, *Adv. Sci.* **2018**, *5*, 1801029.
[160] K. Kočí, H. D. Van, M. Edelmannová, M. Reli, J. C. S. Wu, *Appl. Surf. Sci.* **2020**, *503*, 144426.
[161] H. Li, J. Liu, W. Hou, N. Du, R. Zhang, X. Tao, *Appl. Catal. B* **2014**, *160–161*, 89.
[162] Z. Zhu, W. Lu, N. Li, T. Xu, W. Chen, *Chem. Eng. J.* **2017**, *321*, 58.
[163] Y. Mo, C. Wang, L. Xiao, W. Chen, W. Lu, *Catal. Sci. Technol.* **2021**, *11*, 5952.
[164] G. Anandhababu, S. C. Abbas, J. Lv, K. Ding, Q. Liu, D. D. Babu, Y. Huang, J. Xie, M. Wu, Y. Wang, *Dalton Trans.* **2017**, *46*, 1803.
[165] C. Chu, N. Li, T. Xu, F. Gao, C. Qi, W. Lu, W. Chen, *Appl. Surf. Sci.* **2022**, *592*, 153308.
[166] V. Hasija, P. Raizada, A. Sudhaik, K. Sharma, A. Kumar, P. Singh, S. B. Jonnalagadda, V. K. Thakur, *Appl. Mater. Today* **2019**, *15*, 494.
[167] S. Yang, Y. Yu, M. Dou, Z. Zhang, F. Wang, *J. Am. Chem. Soc.* **2020**, *142*, 17524.
[168] M. Sun, Y. Mao, Y. Na, Y. Liu, Z. Li, M. Chen, P. Li, S. Dai, T. Zhao, *Mater. Sci. Semicond. Process.* **2024**, *177*, 108406.
[169] Y. Xiao, H. Lyu, J. Tang, K. Wang, H. Sun, *Chem. Eng. J.* **2020**, *384*, 123311.
[170] Q. Jiang, M. Ji, R. Chen, Y. Zhang, K. Li, C. Meng, Z. Chen, H. Li, J. Xia, *J. Colloid Interface Sci.* **2020**, *574*, 131.
[171] Z. Zhang, W. Zhang, T. Wang, C. Su, X. Dong, *Surf. Interfaces* **2024**, *44*, 103812.
[172] T. Ma, Y. Mao, C. Liu, M. Sun, Z. Li, M. Chen, R. Zheng, S. Dai, X. Guo, T. Zhao, *J. Alloys Compd.* **2023**, *941*, 169032.
[173] X. Li, T. Ma, L. Dong, Y. Na, Y. Liu, Z. Li, R. Zheng, S. Dai, T. Zhao, *Adv. Powder Technol.* **2022**, *33*, 103468.
[174] A. Michaely, O. Janka, E. C. J. Gießelmann, R. Haberkorn, H. T. A. Wiedemann, C. W. M. Kay, G. Kickelbick, *Chem. Eur. J.* **2023**, *29*, 202300223.
[175] Z. Zhiqiang, Z. Xianyou, W. Ze, D. Limin, *Chin. Sci. Bull.* **2005**, *50*, 2691.
[176] M. Zain, K. A. Yasin, S. Haq, W. Rehman, S. U. Din, S. Shujaat, A. Syed, M. K. Hossain, B. A. Paray, J. Razzokov, A. Samad, *RSC Adv.* **2024**, *14*, 15085.
[177] L. S. Bezerra, S. A. Belhout, S. Wang, J. Quiroz, P. F. M. de Oliveira, S. Shetty, G. Rocha, H. L. S. Santos, S. Frindy, F. E. Oropeza, V. A. de la Peña O'Shea, A. J. Kallio, S. Huotari, W. Huo, P. H. C. Camargo, *ACS Appl. Mater. Interfaces* **2024**, *16*, 11467.
[178] X. Fang, M. Yao, L. Guo, Y. Xu, W. Zhou, M. Zhuo, C. Shi, L. Liu, L. Wang, X. Li, W. Chen, *ACS Sustain. Chem. Eng.* **2017**, *5*, 10735.
[179] Z. Li, M. Chen, Q. Zhang, D. Tao, *J. Alloys Compd.* **2020**, *845*, 156291.
[180] M. Zarei, N. Jesarati, E. Narimani, M. Darbandi, R. Torkamani, B. Aslibeiki, *Adv. Powder Technol.* **2024**, *35*, 104550.
[181] E. Gong, S. Ali, C. B. Hiragond, H. S. Kim, N. S. Powar, D. Kim, H. Kim, S. Il In, *Energy Environ. Sci.* **2022**, *15*, 880.
[182] S. S. Mani, S. Rajendran, T. Mathew, C. S. Gopinath, *Energy Adv.* **2024**, *3*, 1472.
[183] A. Naseri, M. Samadi, A. Pourjavadi, A. Z. Moshfegh, S. Ramakrishna, *J. Mater. Chem. A Mater.* **2017**, *5*, 23406.
[184] Q. Xu, Z. Xia, J. Zhang, Z. Wei, Q. Guo, H. Jin, H. Tang, S. Li, X. Pan, Z. Su, S. Wang, *Carbon Energy* **2023**, *5*, 205.
[185] H. Deng, X. jin Ma, H. Yang, J. Yin, Y. Liu, L. Wu, S. ying Shi, H. qiang Liu, X. Ma, Y. xiang Li, Y. Xiong, *J. Photochem. Photobiol. A Chem.* **2024**, *454*, 115716.
[186] W. Liu, R. Xu, Y. Wang, N. Huang, T. Shimada, L. Ye, *Int. J. Hydrogen Energy* **2022**, *47*, 16005.
[187] F. Yu, T. Huo, Q. Deng, G. Wang, Y. Xia, H. Li, W. Hou, *Chem. Sci.* **2022**, *13*, 754.
[188] I. Bertuol, L. Jiménez-Rodríguez, R. R. Solís, P. Canton, M. Selva, M. Calero, A. Perosa, D. Rodríguez-Padrón, M. J. Muñoz-Batista, *Sustain. Energy Fuels* **2025**, *9*, 2031.
[189] H. Lv, X. Zhao, H. Niu, S. He, Z. Tang, F. Wu, J. P. Giesy, *J. Hazard. Mater.* **2019**, *369*, 494.
[190] S. Wang, W. Liu, J. Wang, J. Yu, F. Wang, C. Jin, K. Wang, P. Cheng, Z. Zhang, Y. Chen, *ACS Mater. Lett.* **2024**, *6*, 2609.
[191] V. H. Nguyen, H. H. Do, T. Van Nguyen, P. Singh, P. Raizada, A. Sharma, S. S. Sana, A. N. Grace, M. Shokouhimehr, S. H. Ahn, C. Xia, S. Y. Kim, Q. Van Le, *Sol. Energy* **2020**, *211*, 584.
[192] X. Wang, Y. Peng, S. Yang, H. G. Yang, Y. Hou, *Mater. Chem. Front.* **2023**, *7*, 4635.
[193] C. Abia, C. A. López, J. Gainza, J. E. F. S. Rodrigues, B. Fragoso, M. M. Ferrer, M. T. Fernández-Díaz, F. Fauth, J. L. Martínez, J. A. Alonso, *ACS Appl. Mater. Interfaces* **2023**, *15*, 40762.
[194] C. A. López, C. Abia, J. Gainza, J. E. Rodrigues, B. Martinelli, F. Serrano-Sánchez, R. S. Silva, M. M. Ferrer, O. J. Dura, J. L. Martínez, M. T. Fernández-Díaz, J. A. Alonso, *Inorg. Chem.* **2024**, *63*, 12641.
[195] J. Estrada-Pomares, S. Ramos-Terrón, G. Lasarte-Aragonés, R. Lucena, S. Cárdenas, D. Rodríguez-Padrón, R. Luque, G. de Miguel, *J Mater Chem A Mater* **2022**, *10*, 11298.
[196] K. K. F. Barbosa, D. Aristizábal-Giraldo, J. M. Osorio-Guilí, J. J. J. S. Acuña, F. F. Ferreira, *RSC Mechanochem.* **2024**, *1*, 69.
[197] K. Kundu, P. Dutta, P. Acharyya, K. Biswas, *Mater. Res. Bull.* **2021**, *140*, 111339.
[198] Y. Xiao, D. G. Bradley, W. X. Chan, X. Hu, L. Xiao, Z. Liu, Z. Y. Tan, X. Zhao, C. Li, M. Sadek, V. K. Ravi, Y. H. Tam, X. Wang, F. García, H. Sun, S. C. Low, P. B. Phua, T. C. Sum, X. Zhou, Y. F. Lim, J. V. Hanna, H. S. Soo, *Nat. Commun.* **2025**, *16*, 1362.

[199] H.-E. Nemamcha, N.-N. Vu, D. S. Tran, C. Boisvert, D. D. Nguyen, P. Nguyen-Tri, *Sci. Total Environ.* **2024**, *931*, 172816.
[200] M. Naguib, O. Mashtalir, J. Carle, V. Presser, J. Lu, L. Hultman, Y. Gogotsi, M. W. Barsoum, *ACS Nano* **2012**, *6*, 1322.
[201] T. Amrillah, A. R. Supandi, V. Puspasari, A. Hermawan, Z. W. Seh, *Trans. Tianjin Univ.* **2022**, *28*, 307.
[202] S. Iravani, A. Zarepour, E. Nazarzadeh Zare, P. Makvandi, A. Khosravi, R. S. Varma, A. Zarrabi, *Mater. Adv.* **2024**, *5*, 8404.
[203] X. Shi, W. Liang, G. Liu, B. Chen, L. Shao, Y. Wu, Z. Sun, F. García, *Chem. Eng. J.* **2023**, *462*, 142271.
[204] X. Wang, J. Chen, D. Wang, Z. Mao, *ACS Appl. Energy Mater.* **2021**, *4*, 10280.
[205] H. Liu, J. Zhou, B. Li, Z. Liu, L. Zhou, T. Wang, *Chem. Eng. J.* **2024**, *490*, 151807.
[206] L. Biswal, R. Mohanty, S. Nayak, K. Parida, *J. Environ. Chem. Eng.* **2022**, *10*, 107211.
[207] X. Fan, P. Du, X. Ma, R. Wang, J. Ma, Y. Wang, D. Fan, Y. Long, B. Deng, K. Huang, H. Wu, *Materials* **2021**, *14*, 2426.
[208] T. Zhang, X. Jiang, G. Li, Q. Yao, J. Y. Lee, *ChemNanoMat* **2018**, *4*, 56.
[209] C. C. Leong, Y. Qu, Y. Kawazoe, S. K. Ho, H. Pan, *Catal. Today* **2021**, *370*, 2.
[210] Y. Sun, X. Meng, Y. Dall'Agnese, C. Dall'Agnese, S. Duan, Y. Gao, G. Chen, X.-F. Wang, *Nanomicro Lett* **2019**, *11*, 79.
[211] K. Li, S. Zhang, Y. Li, J. Fan, K. Lv, *Chin. J. Catal.* **2021**, *42*, 3.
[212] M. M. Nair, A. C. Iacoban, F. Neaţu, M. Florea, Ş. Neaţu, *J. Mater. Chem. A Mater.* **2023**, *11*, 12559.
[213] J. K. Im, E. J. Sohn, S. Kim, M. Jang, A. Son, K. D. Zoh, Y. Yoon, *Chemosphere* **2021**, *270*, 129478.
[214] N. Gamba, V. Farina, S. Garroni, G. Mulas, F. Gennari, *Powder Technol.* **2021**, *377*, 857.
[215] Y. Miura, T. Kashiwagi, T. Fukuda, A. Shichiri, T. Shiobara, K. I. Saitow, *ACS Sustain. Chem. Eng.* **2022**, *10*, 16159.
[216] T. Mizutani, H. Ohta, T. Ueda, T. Kashiwagi, T. Fukuda, T. Shiobara, K. I. Saitow, *ACS Sustain. Chem. Eng.* **2023**, *11*, 11769.
[217] S. Li, X. Zhang, F. Yang, J. Zhang, W. Shi, F. Rosei, *Chem Catalysis* **2024**, *4*, 100901.
[218] M. J. Muñoz-Batista, M. M. Ballari, A. Kubacka, O. M. Alfano, M. Fernández-García, *Chem. Soc. Rev.* **2019**, *48*, 637.
[219] M. J. Muñoz-Batista, *Catalysts* **2024**, *15*, 7.
[220] R. R. Solís, M. A. Quintana, G. Blázquez, M. Calero, M. J. Muñoz-Batista, *Catal. Today* **2023**, *423*, 114266.
[221] V. Martinez, T. Stolar, B. Karadeniz, I. Brekalo, K. Užarević, *Nat. Rev. Chem.* **2022**, *7*, 51.
[222] X. Xin, J. Geng, D. Zhang, H. T. Ang, H. Wang, Y. Cheng, Y. Liu, R. W. Toh, J. Wu, H. Wang, *Nat. Synth.* **2024**, *4*, 177.
[223] I. Cvrtila, V. Štrukil, M. Alešković, I. Kulcsár, T. Mrla, E. Colacino, I. Halasz, *Chemistry – Methods* **2025**, 202400089.
[224] F. Millward, E. Zysman-Colman, *Angew. Chem., Int. Ed.* **2024**, *63*, 202316169.

Oscar Trentin obtained his Master's degree in Sustainable Chemistry and Technologies from Ca' Foscari University of Venice with a thesis in mechanochemistry. In December 2023, he undertook the Research Doctorate of National Interest in Design for Made in Italy: Identity, Innovation, and Sustainability. He is currently a PhD student in the Green Organic Synthesis Team at Ca' Foscari, supervised by Professor Alvise Perosa, focusing on green mechanochemical synthesis of heterogeneous catalysts for cross-coupling reactions via reactive extrusion. He has published three articles green chemistry field and won a poster prize at the 9th EuChemS Chemistry Congress in Dublin.

Mario J. Muñoz-Batista is a professor at the Department of Chemical Engineering of the University of Granada. He has extensive experience in developing new methods for material preparation, optimization, and mathematical modelling of energy-efficient and environmentally friendly chemical processes. His research encompasses applications from decontamination and effluent treatment processes to new routes for obtaining chemicals, fuel production, and new energy vectors, including catalytic processes and waste valorization. The quality of his scientific contributions is reflected in the publication of over 100 scientific articles, the editing of several books and chapters, and participation in the major scientific dissemination events in his field.

Alvise Perosa earned his Ph.D. in Chemistry from Case Western Reserve University in 1996 and is currently an associate professor of Organic Chemistry at Ca' Foscari University, Venice. He was a Fulbright Fellow at Case Western Reserve University, an Endeavour Research Fellow at the University of Sydney, and is currently a Fellow of the Royal Society of Chemistry. Alvise sits on the Editorial Advisory Boards of Green Chemistry (RSC) and ACS Sustainable Chemistry and Engineering (ACS). Alvise's interests include research, teaching, and outreach in green chemistry with a focus on chemicals from renewables, like carbon dioxide, ionic liquids, catalysis, supercritical fluids, and multiphase systems.

Maurizio Selva is a full professor of Organic Chemistry at the Department of Molecular Sciences and Nanosystems, University Ca' Foscari Venezia (Italy). Since the beginning of his academic career in the early 90s, his main research interests have focused on the implementation of eco-friendly organic syntheses based on clean reagents, catalysts, and solvents. More specifically, the development of green catalytic techniques for the upgrading of bio-based platform chemicals using dense CO_2 and dialkyl carbonates and multiphase systems assisted by ionic liquids is among the current topics of research of Prof. Selva.

Daily Rodríguez-Padrón is a Marie-Curie Post-Doc researcher at the University Ca' Foscari Venezia, Italy. Her research has been focused on mechanochemistry and biomass valorization, with 88 articles and 2 patents. She serves on the Early Career Advisory Board of ChemCatChem. Her achievements include the Dan David Prize 2019 from Tel Aviv University, Israel, and the Green Talent Award 2020 from the German Federal Ministry of Education and Research. She was recognized as part of the Green Chemistry Emerging Investigators Series 2024 in Green Chemistry, the Sustainability Talents Special Collection 2024 in ChemSusChem, and the Catalysis Talents Class of 2023 in ChemCatChem.